

The design of an innovative hydrogen-oxygen power system based upon a solid oxide fuel cell and an advanced thermodynamic cycle

by

T.J. Evertse

To obtain the degree of Master of Science in Mechanical Engineering
at the Delft University of Technology,
to be defended on 01-07-2021.

Student number: 4623940
Project duration: February, 2020 – July, 2021
Thesis committee: Prof. Dr. Ir. S. Klein TU Delft, supervisor
Prof. Dr. Ir. B.J. Boersma TU Delft
Dr. Ir. L. van Biert TU Delft

An electronic version of this thesis is available at <http://repository.tudelft.nl/>.

Abstract

In the battle against climate change, humankind needs to develop alternative energy systems if it wants to survive on this planet. Fossil fuels, polluting the air with CO_2 , must make way for renewable sources so that climate change is put to a stop. Several new energy initiatives based on renewable sources are deployed worldwide, these however are mostly for electricity generation. There are relatively few zero-emission alternatives developed for the energy demand from the transport sector, therefore, new small scale energy systems need to be developed in order to achieve the goals stated in the Paris agreement. The "Hydrogen Roadmap" is a vital part of the European Union in achieving the Paris climate agreement, which uses hydrogen for future energy generation. Gas turbines, steam turbines and fuel cell applications are investigated thoroughly for small scale energy systems throughout the years. Fewer research is conducted about the integration of these three energy technologies and specially sparse research has been conducted in the area of pure hydrogen-oxygen combustion for these energy systems, resulting in opportunities for development. This report introduces an alternative small scale power system suited for the newest inland shipping vessels. It proposes a basic design for a 3 MW SOFC integrated hydrogen-oxygen fired combined power cycle, feasible within 10-20 years of research and development.

First, the theoretical background for the research is elaborated covering the thermodynamics of traditional power cycles, exergy analysis theory and zero-emission cycles such as hydrogen-oxygen fuelled power cycles. The electrochemical research containing the fuel cell operating specifics and the advantages of integrating fuel cell stacks in power cycles is introduced next. The theoretical background ends with an elaboration on the preliminary design steps for power cycle components regarding turbomachinery and heat exchange equipment.

After the relevant subjects regarding power cycles and fuel cells are elaborated, a basic cycle was designed. From literature, several starting points such as the maximum turbine inlet temperature and inlet temperatures of the SOFC were defined. With a few determining thermodynamic states known on beforehand, a pressure and temperature analysis was carried out to determine the limiting operating conditions and the remaining thermodynamic states in the cycle. The cycle was eventually designed as a SOFC integrated Brayton-Rankine cycle coupled via a single pressure heat recovery steam generator, where the SOFC is situated upstream of the combustor in the Brayton part of the cycle. All components in the cycle are evaluated using an exergy analysis, from which the final exergetic efficiency was determined as 73.09%.

From the exergy analysis of the proposed basic cycle became clear that there was potential for improvement regarding the HRSG design. The improved cycle is therefore designed with a dual pressure HRSG, while the rest of the combined cycle remains equal compared to the basic cycle. With the extra high pressure regime, a high pressure turbine is added, thus creating an extra point in the system from which useful power is extracted from the medium. The exergetic efficiency increase of the HRSG alone amounts to 0.74%, but due to extra compressor and pump work and losses, the improved cycle results in a total efficiency of 73.47%, implying an increase of 0.38% compared to the basic cycle.

To give a first practical indication about the size and specifics of the proposed cycles, a preliminary design of the components is made. The turbomachinery is sized according to the appropriate non-dimensional numbers, the specific speed and diameter. An indication about the SOFC stack size and its operating specifics are given, together with the preliminary designs of the sensible and latent heat exchangers. A total preliminary size estimation of the cycle predicted a system with the size of approximately 4.5 shipping containers.

Preface

Before you lies the master thesis "The design of an innovative hydrogen-oxygen power system based upon a solid oxide fuel cell and an advanced thermodynamic cycle". It has been written to fulfil the graduation requirements for the master Mechanical Engineering, specialised in Energy and Process Technology at the Delft University of Technology.

First of all, I would like to express my gratitude to Prof. Dr. Ir. Sikke Klein for letting me work on this project and his supervision this last year. His guidance during this period in not only the obvious technical part of the project, but also in the unforeseen challenges related to the COVID 19 pandemic is something I am grateful for. Furthermore, I would like to thank Dr. Ir. Lindert van Biert for helping me with the fuel cell related questions.

Additionally, I would like to thank my parents for providing me a workplace when the university closed down due to the pandemic and working from home did not went well for me. The same goes for my buddy Guido who opened up his home for me in the final weeks of the graduation project so I could work undisturbed.

Finally, I would like to thank the rest of my family, friends and girlfriend for their support. Even when I was having challenging moods, you kept supporting me which gave me the endurance to finish my work.

Tom Evertse
Rotterdam, June 2021

Contents

Abstract	iii
List of Figures	ix
List of Tables	xi
Nomenclature	xiii
1 Introduction	1
2 Thermodynamic power cycle analysis	5
2.1 Power cycle thermodynamics	5
2.2 Exergy analysis theory	6
2.2.1 The closed system entropy balance	6
2.2.2 Exergy analysis of a system	7
2.3 Classic thermodynamic cycles	9
2.3.1 Joule-Brayton cycle	9
2.3.2 Rankine cycle	10
2.3.3 Governing power cycle equations	11
2.4 Combined cycle power plants	12
2.5 Zero emission power cycles	13
2.5.1 The Graz cycle	13
2.5.2 Allam cycle	14
2.5.3 Hydrogen-oxygen cycles	14
3 The Solid Oxide Fuel Cell	17
3.1 Fuel cell principles	17
3.2 SOFC Components	19
3.3 SOFC performance & characteristics	21
3.4 Advantages of integrating a SOFC into a power cycle	24
4 Power cycle equipment	27
4.1 Compressor & turbine selection	27
4.2 Preliminary turbomachinery design steps	29
4.3 Heat Recovery Steam Generator	30
4.3.1 Single pressure HRSG	30
4.3.2 Multiple pressure HRSG	31
4.4 Heat exchange equipment	32
4.4.1 Preliminary design steps	33
5 Thermodynamic design of the basic power cycle	35
5.1 Starting points	35
5.1.1 Pressure analysis	36
5.1.2 Starting points of the cycle	38
5.2 Basic power cycle thermodynamics	39
5.2.1 SOFC integrated Brayton cycle	39
5.2.2 Single pressure heat recovery steam generator	41
5.2.3 Rankine cycle	44
5.3 Basic cycle exergy analysis	48
6 Thermodynamic design of the improved power cycle	49
6.1 HRSG-Steam Turbine	50
6.2 Dual pressure HRSG design	51
6.3 Improved cycle exergy analysis	54

7	Preliminary equipment design	55
7.1	Turbomachinery design	55
7.2	Solid Oxide Fuel Cell design	60
7.3	First steps of the heat exchanger design procedure	63
7.3.1	Shell & tube versus welded plate heat exchangers	65
7.3.2	Sensible heat exchanger design results.	66
7.4	Latent heat exchanger design	67
7.4.1	Condenser design	67
7.4.2	Evaporator design	68
7.5	Comparison with commercial equipment	70
7.5.1	Inland shipping application.	71
7.5.2	Preliminary size estimation of the basic cycle.	72
8	Conclusion & recommendations	73
8.1	Conclusion	73
8.2	Recommendations for future research	74
	Bibliography	75
A	Mathematical derivations	81
A.1	Enthalpy & entropy change of the reaction	81
A.2	Ideal gas use verification.	82
A.3	Shell & Tube heat exchanger design steps continued	83
A.4	Plate heat exchanger design steps continued	86
B	Thermoflex simulation models	89
B.1	Basic cycle Thermoflex model	90
B.2	Improved cycle Thermoflex model.	91

List of Figures

1.1	Global surface temperature relative to 1951-1980 average temperatures	1
1.2	Atmospheric CO_2 levels in ppm since 2005 measured at Mauna Loa Observatory, Hawaii	1
1.3	CO_2 levels during the last three glacial cycles, as reconstructed from ice cores by NOAA, the National Oceanic and Atmospheric Administration within the U.S. Department of Commerce [1]	2
1.4	Global electricity and total energy sources in 2019, Data based on BP Statistical Review of World Energy	2
1.5	Schematic flow scheme of a CCGT plant for electricity production [22]	3
2.1	Schematic diagram of a power cycle [55]	5
2.2	Energy flow diagram, system diagram & exergy flow diagram of a hot water boiler [95] .	8
2.3	Diagram of the basic open or closed Joule-Brayton cycle [55]	9
2.4	Schematic T-s diagram of the basic Joule-Brayton cycle [55]	9
2.5	The basic Rankine cycle with its four principle components [55]	10
2.6	Schematic temperature-entropy diagram of the basic Rankine cycle [55]	10
2.7	Schematic diagram of a combined gas turbine-vapour power plant [55]	12
2.8	Principle flow scheme of the adapted Graz cycle, suitable for hydrogen/oxygen combustion [71]	13
2.9	Schematic flow scheme of the oxy-fired gas variant Allam cycle [5]	14
2.10	Electric efficiency as a function of the rated load for a fuel cell power plant compared with thermal power plants [56]	15
3.1	Schematic of the basic working principle of a SOFC fuelled by H_2 and O_2 [48]	17
3.2	Schematic of the basic working principle of a SPFC/PEMFC [48]	17
3.3	Efficiency limit comparison of a Carnot process, a fuel cell and a FC integrated CCGT cycle [43]	19
3.4	Theoretical Temperature-Voltage curve of a single cell [11]	19
3.5	Flat plate fuel cell stack with parallel flow [11]	19
3.6	Tubular fuel cell design from Siemens-Westinghouse [11] [33]	19
3.7	Schematic electric circuit of a fuel cell / load system	22
3.8	Schematic relation between the current density versus cell voltage of a standard SOFC with the specific loss regions [11]	24
3.9	Schematic current density versus cell voltage together with the optimum power of the FC [11]	24
3.10	Schematic example of a hybrid SOFC-GT configuration [84]	25
4.1	The Baljé diagram for single stage compressors [69][79]	28
4.2	The Baljé diagram for single stage expanders [46][79]	28
4.3	General axial and radial compressor operating characteristics	29
4.4	General axial and radial turbine operating characteristics	29
4.5	Schematic diagram of a single pressure HRSG [57]	30
4.6	Schematic TQ-diagram of a single pressure HRSG with its approach and pinch points [4] .	30
4.7	Schematic diagram of a dual pressure HRSG [7]	31
4.8	Temperature-Enthalpy diagram of a dual pressure HRSG [7]	31
4.9	Schematic shell & tube heat exchanger diagram	32
4.10	Schematic exploded view of a plate & frame heat exchanger	32
4.11	Schematic plate & shell heat exchanger	32
4.12	Exploded view of a fully welded plate heat exchanger [42]	33

5.1	Principle flow scheme of the preliminary SOFC integrated combined cycle	35
5.2	HTT-PR vs SOFC cooling steam inlet temperature for each ΔT_{min}	36
5.3	HTT-PR vs SOFC cooling steam inlet temperature cutoff for max PR for each ΔT_{min}	36
5.4	Heat exchangers ΔT_{min} vs HTT power output	37
5.5	Heat exchangers ΔT_{min} vs LPT power output	37
5.6	HTT-PR vs Gross power output of the combined cycle (excl. SOFC power)	37
5.7	HTT-PR vs Thermal efficiency of the combined cycle (incl. SOFC power)	37
5.8	Schematic overview of the designed SOFC-Brayton part of the integrated SOFC combined cycle	41
5.9	Schematic overview of the basic, single pressure heat recovery steam generator and compressor	41
5.10	Temperature-Heat transfer diagram of the basic, single pressure heat recovery steam generator	42
5.11	Schematic overview of the designed Rankine part of the integrated SOFC combined cycle	44
5.12	Mollier diagram with the LPT expansion path, the corresponding isobars and lines of constant vapour quality	45
5.13	Schematic overview of the designed integrated SOFC combined power cycle	46
5.14	Exergy flow diagram of the basic cycle	48
6.1	Principle flow scheme of the preliminary dual pressure HRSG, HPT and compressor	49
6.2	HPT inlet pressure variation versus the power cycle output, SOFC power excluded	50
6.3	Mollier diagram with the expansion path of both steam turbines in the improved cycle	51
6.4	Schematic overview of the improved cycle, dual pressure HRSG, HPT and compressor	51
6.5	Temperature-Heat transfer diagram of the dual pressure HRSG	53
6.6	Exergy flow diagram of the improved cycle	54
7.1	The Baljé N_s - D_s diagram for single stage compressors [69]	56
7.2	The Baljé N_s - D_s diagram for single stage expanders [46]	56
7.3	Unshrouded compressor impeller (front left) vs shrouded compressor impeller (right) [78]	57
7.4	Radial turbomachinery N_s versus shaft speed N per stage	57
7.5	Axial LPT N_s versus shaft speed N per stage	57
7.6	Radial turbomachinery N_s versus impeller tip diameter d_t per stage	59
7.7	Axial LPT N_s versus impeller tip diameter d_t per stage	59
7.8	Schematic overview of a Ceres Power metal supported cell structure [45]	60
7.9	Cell voltage vs efficiency vs power density of the M-SOFC	62
7.10	Current density vs cell voltage vs power density curves of the M-SOFC	62
7.11	Schematic side view of a part of the planar SOFC stack showing the unit cell [45]	62
7.12	Schematic top view of a 9-cell bipolar plate [45]	62
7.13	Standard heat exchanger temperature diagram	64
7.14	A size comparison between a Shell & tube design vs a plate heat exchanger design for equal heat transfer duty [36]	65
7.15	The C600S Power Package developed by Capstone [21]	70
7.16	MDT-300 developed by Turbonik as suggested LPT [86]	70
7.17	Lay-out of the DEMCOPEM 2 MWe PEM fuel cell system with human for scale [82]	71
7.18	The inland shipping vessel "Antonie", currently developed to be powered by a 100% hydrogen fuelled PEM fuel cell [66]	71
A.1	The graphical relation between Z^0 , P_r and T_r [75]	82

List of Tables

2.1	Standard chemical exergy and molecular mass of hydrogen, oxygen and water [6]	7
2.2	Main performance parameters of the discussed carbon free cycles in nominal conditions	15
3.1	A comparison of fuel cell technologies [9][27][43][45]	18
3.2	SOFC-combined cycle studies conducted in the past years in chronological order [90] .	25
4.1	Overview of the operating parameters of the four discussed heat exchanger designs . .	33
5.1	Thermodynamic input data from literature	36
5.2	Component efficiencies and key parameters of the proposed cycle thermodynamic simulation	38
5.3	Solid oxide fuel cell thermodynamic operating specifics	39
5.4	Gas Turbine thermodynamic operating specifics	40
5.5	Reactant hydrogen & oxygen heat exchanger thermodynamic operating specifics	40
5.6	Combustion chamber operating specifics	41
5.7	Basic HRSG thermodynamic operating specifics	42
5.8	Compressor thermodynamic operating specifics	43
5.9	Low Pressure Turbine thermodynamic operating specifics	44
5.10	Condenser operating specifics	45
5.11	Pump operating specifics	46
5.12	Basic cycle power distribution overview	47
5.13	Exergy analysis results of the basic power cycle	48
6.1	High Pressure Turbine operating specifics	50
6.2	Improved HRSG LP regime thermodynamic operating specifics	52
6.3	Improved HRSG HP regime thermodynamic operating specifics	52
6.4	Improved cycle power distribution overview	53
6.5	Exergy analysis results of the improved power cycle	54
7.1	Analysed N_s - D_s coordinates in the Baljé diagram for a radial compressor stage	58
7.2	Optimal N_s - D_s coordinates in the Baljé diagram for 90% efficiency radial turbines	58
7.3	Analysed N_s - D_s coordinates in the Baljé diagram for an axial turbine stage	58
7.4	Preliminary turbomachinery design specifics	59
7.5	Parameters used in the electrochemical model for the metal-supported cell [3][45]	60
7.6	Electrochemical results of the M-SOFC	61
7.7	Geometrical and total power result of the designed M-SOFC stack	63
7.8	Shell & tube vs welded plate heat exchanger comparison	65
7.9	Welded plate exchanger design specifications for the basic cycle	66
7.10	Heat exchanger design specifications for the improved cycle	66
7.11	Welded plate condenser design specifications for both cycles	67
7.12	Evaporator design specifications for both cycles	69
7.13	Provisional size estimation of the components and cycle	72
A.1	Heat capacity constants, standard enthalpies & Gibbs energies of formation of the gasses in the ideal-gas state	82

Nomenclature

Variables and physical constants

α	Heat transfer coefficient	$\frac{W}{m^2 \cdot ^\circ C}$
β	Surface area density	$\frac{m^2}{m^3}$
\dot{m}	Mass flow	$\frac{kg}{s}$
η	Efficiency	–
λ	Thermal conductivity	$\frac{W}{mK}$
Ω	Shaft speed	$\frac{rad}{s}$
ϕ	Flow coefficient	–
Ψ	Load coefficient	–
ρ	Density	$\frac{kg}{m^3}$
σ	Entropy production	$\frac{J}{K}$
A	Area	m^2
B_d	Bond number	–
Bo_{eq}	Equivalent boiling number	–
C_p	Heat capacity at constant pressure	$\frac{J}{K}$
C_p^{ig}	Ideal gas heat capacity at constant pressure	$\frac{J}{K}$
D_s	Specific diameter	–
d_t	Impeller tip diameter	m
E	Voltage	V
E_0	Maximum voltage	V
E_d	Exergy destruction	J
E_x	Exergy	J/s
e_x^{ch}	Chemical exergy	$\frac{J}{kg}$
e_x^{tm}	Thermomechanical exergy	$\frac{J}{kg}$
E_{cell}	Cell voltage	V
E_{load}	Load voltage	V
E_{loss}	Voltage loss	V
E_{Nernst}	Nernst voltage	V

e_{xf}	Specific exergy of a flow		$\frac{J}{kg}$
F	Faraday constant	96485.33	$\frac{A \cdot s}{mol}$
$f_{ex,F}$	Fuel exergy factor		—
G	Mass flux		$\frac{kg}{m^2 \cdot s}$
g	Gravitational acceleration	9.81	$\frac{m}{s^2}$
G_{eq}	Equivalent mass flux		$\frac{kg}{m^2 \cdot s}$
H	Enthalpy		J
h	Specific enthalpy		$\frac{J}{kg}$
H^o	Standard enthalpy		J
H_f^o	Standard enthalpy of formation		J
I	Current		A
i	Current density		$\frac{A}{m^2}$
I_{cell}	Cell current		A
I_{load}	Load current		A
k	Heat capacity ratio		$\frac{c_p}{c_v}$
N	Shaft speed		RPM
N_s	Specific speed		—
P	Power		W
p	Pressure		Pa
Q	Heat		J
R	Universal Gas constant	8.31	$\frac{J}{mol \cdot K}$
R_i	Rate of species		$\frac{mol}{s}$
Re_{eq}	Equivalent Reynolds		—
Res	Resistance		Ω
S	Entropy		$\frac{J}{K}$
s	Specific entropy		$\frac{J}{kg \cdot K}$
S^o	Standard Entropy		$\frac{J}{K}$
S_f^o	Standard entropy of formation		$\frac{J}{K}$
T	Temperature		K
T_{ap}	Approach point temperature		K
T_{pp}	Pinch point temperature		K

u	Specific internal energy	$\frac{J}{kg}$
U_0	Overall heat transfer coefficient	$\frac{J}{m^2 \cdot s \cdot K}$
v	Specific volume	$\frac{m^3}{kg}$
W	Work	J
z	Height	m
Z^0	compressibility factor	—

Subscripts

b	Evaluated at system boundary
c	Compressor
d	Destruction
F	Fuel
f	Flow
G	Gas
L	Liquid
p	Pump
r	Chemical reaction
s	Steam
t	Turbine
$,s$	Isentropic process
act	Activation losses
ass	Assumed
ch	Chemical
cv	Control volume
eq	Equivalent
fc	Forced convective
fg	Flue gas
lm	Logarithmic mean
m	Mean
nb	Nucleate boiling
ohm	Ohmic losses
red	Reduced
sat	Saturated
th	Thermal
$trans$	Transport losses

Acronyms & Abbreviations

ASR	Area Specific Resistance
ASU	Air Separation Unit
BFP	Boiler Feedwater Pump
CCGT	Combined Cycle Gas Turbine
COND	Condenser
DE	Dearator
DOF	Degree Of Freedom
DOP	Drum Operating Pressure
GISS	Goddard Institute for Space Studies
GPHE	Gasket Plate Heat Exchanger
GT	Gas Turbine
HEX	Heat Exchanger
HFCTC	Hydrogen Fuelled Combustion Turbine Cycle
HHV	Higher Heating Value
HPT	High Pressure Turbine
HRSG	Heat Recovery Steam Generator
HTT	High Temperature Turbine
LHV	Lower Heating Value
LPT	Low Pressure Turbine
NASA	National Aeronautics and Space Administration
NOAA	National Oceanic and Atmospheric Administration
OEM	Original Equipment Manufacturer
PEMFC	Proton Exchange Membrane Fuel Cell
PSHE	Plate & Shell Heat Exchanger
RPM	Revolutions Per Minute
S&T	Shell and Tube
SOFC	Solid Oxide Fuel Cell
SPFC	Solid Polymer Fuel Cell
WE-NET	World Energy Network
WPHE	Welded Plate Heat Exchanger
YSZ	Yttria-Stabilised Zirconia

Introduction

Climate change is one of the most important challenges the human race is facing at the moment. The increasing concentration of greenhouse gasses that trap the heat of the sun are extremely worrying and directly related to the existence of human life on this planet. In 2019, a group of international scientists officially declared that the human influence in climate change could no longer be ignored or denied. Multiple researches have proved that the chance that human interaction has had no effect on the development of the overall surface temperatures on the planet is one in 3.5 million [70]. Figure 1.1 shows the change in global surface temperature relative to 1951-1980 average temperatures to give an idea about the deviation nowadays. Institutions such as NASA/GISS state that nineteen of the twentieth warmest years ever recorded all happened since the year 2001, with the year 2020 breaking all temperature records. The year 2020 was the warmest year since the beginning of the weather measurements by Copernicus, the earth observatory program from the European Union. The year was on average 0.4 degrees Celsius warmer compared to 2019, Europe was 1.6 degrees warmer compared to the long period average of the period from 1981-2020. Last year was the sixth year in a row measuring exceptionally warm yearly averages since 2015, contributing to the hottest decade ever recorded 2011-2020 [25]. The rapid increase in global surface temperature is due to heat-trapping (greenhouse) gasses in the atmosphere. These gasses are released in human related processes such as the burning of fossil fuel and deforestation and natural processes such as volcanic eruptions and respiration. The graph depicted in figure 1.2 shows the increase of carbon dioxide concentration in the atmosphere in parts per million (ppm) since 2005.

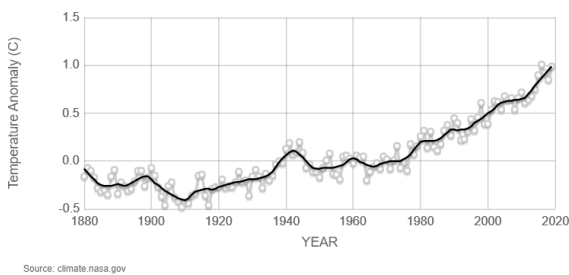


Figure 1.1: Global surface temperature relative to 1951-1980 average temperatures

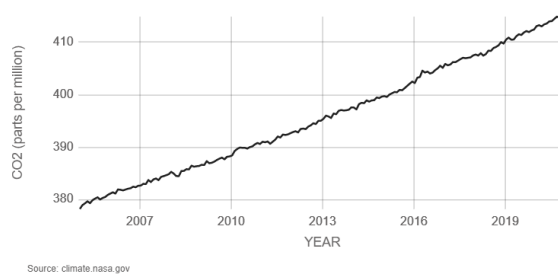


Figure 1.2: Atmospheric CO₂ levels in ppm since 2005 measured at Mauna Loa Observatory, Hawaii

To fully comprehend these levels of carbon dioxide (CO₂) in the atmosphere, some perspective is required. Figure 1.3 depicts the atmospheric CO₂ levels since the last three glacial cycles reconstructed from ice core samples made by NOAA (National Oceanic and Atmospheric Administration) [1]. In the last 170 years, human related processes have raised the atmospheric CO₂ concentrations by 47% above pre-industrial levels found in 1850. To put this in perspective, the last glacial period raised the CO₂ concentration by natural processes from 185 ppm to 280 ppm but required approximately 20,000 years to reach this level.

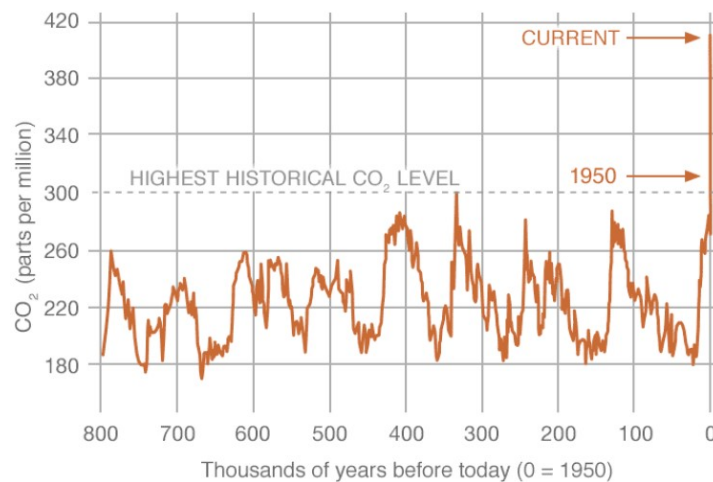


Figure 1.3: CO_2 levels during the last three glacial cycles, as reconstructed from ice cores by NOAA, the National Oceanic and Atmospheric Administration within the U.S. Department of Commerce [1]

As previously mentioned, the high concentrations of CO_2 in the atmosphere are directly related to the burning of fossil fuels. The energy sector contributes much to these carbon emissions since the production methods highly rely on the burning of fossil fuels. It is therefore of the utmost importance to develop new energy systems capable to deliver the energy demand of the total energy demand. New energy technologies regarding solar and wind energy are developed and continuously improved. Worldwide solar and wind parks are installed to generate sustainable energy on an increasing scale. The unfortunate reality is that this is almost exclusively for the production of electricity.

The energy sector can be divided in three parts, electricity, transport and heating. Decarbonising electricity production is an important step in the process of creating a global CO_2 free energy system, but it is only a part of the solution. The fact that the energy demand for heating is approximately five times higher than the energy demand for electricity explains the differences in figure 1.4. The figure depicts the global electricity and total energy sources in the year 2019.

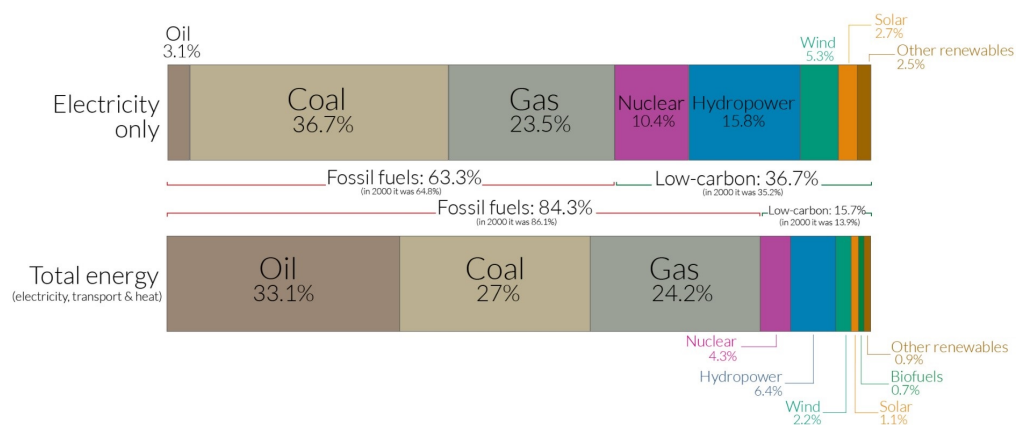


Figure 1.4: Global electricity and total energy sources in 2019, Data based on BP Statistical Review of World Energy

The transport and heating demand is more challenging to decarbonise. New, high efficiency and clean energy systems need to be developed that are able to take care of the total energy demand of the future. One of the most interesting and promising new clean energy technology of the recent years is the hydrogen technology, which is considered a limitless source of clean energy. The European Union focuses on hydrogen as future energy source since it has the potential to take care of all three energy demands [28].

Today's state-of-the-art power plants are Combined Cycle Gas Turbine (CCGT) plants that operate at extremely high temperatures and pressures to achieve high efficiencies. Where open gas turbine cycles reject the flue gasses after the expansion stage, the combined cycle partially recovers the thermal energy from the flue gasses in a heat recovery steam generator (HRSG) before being sent to the stack. The HRSG transfers the waste heat from the gas turbine flue gasses to a closed steam cycle from which more energy is extracted via a low pressure steam turbine. This cascading of energy through multiple pressure regimes makes the combined cycle the most efficient "traditional" power cycle today. With this design, efficiencies up to 62% LHV are achieved, a schematic flow scheme of a CCGT plant is depicted in figure 1.5 [32]. The major losses of such a power cycle are related to the heat addition to the cycle and thus occur in the combustion chamber.

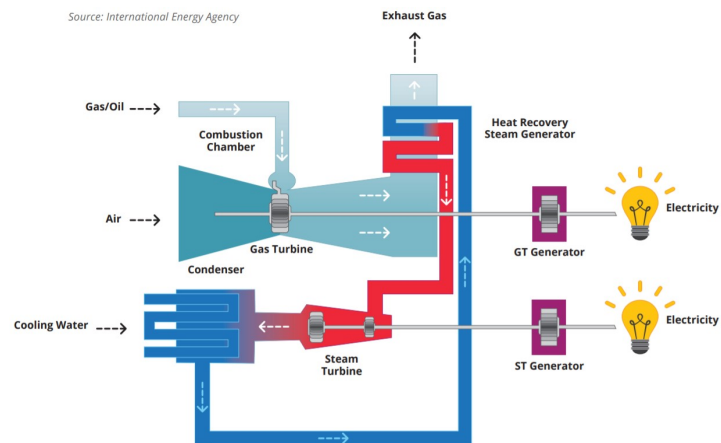


Figure 1.5: Schematic flow scheme of a CCGT plant for electricity production [22]

Previous research conducted by Schouten [73] at the TU Delft showed several improvements for combined cycle power cycles, one of which was the integration of a high temperature fuel cell stack upstream of the combustion chamber. This arrangement resulted in a large efficiency improvements due to significant loss reduction in the combustion chamber. This design was promising in many ways but the operating conditions are not conceivable within the near future, more research is required for more basic alternative systems, feasible in the near future.

The principle via which a fuel cell generates electricity is similar as for batteries, the large advantage a fuel cell has over batteries is that it provides electricity as long as fuel and oxidiser are provided. It converts the chemical energy of a fuel directly into electricity and heat. The energy stored is thus chemical in the form of a fuel, and not electrical as for a battery pack, making the energy storage significantly more dense. The fuel variety on which a fuel cell is able to operate is diverse, one of the most promising fuel options is considered hydrogen [28]. Fuel cells are considered to be the preferred decarbonisation option in the transport sector, especially regarding ships and trains due to the size, scalability and proportionate power ranges [28].

The principle via which a fuel cell generates electricity is similar as for batteries, the large advantage a fuel cell has over batteries is that it provides electricity as long as fuel and oxidiser are provided. It converts the chemical energy of a fuel directly into electricity and heat. The energy stored is thus chemical in the form of a fuel, and not electrical as for a battery pack, making the energy storage significantly more dense. The fuel variety on which a fuel cell is able to operate is diverse, one of the most promising fuel options is considered hydrogen [28]. Fuel cells are considered to be the preferred decarbonisation option in the transport sector, especially regarding ships and trains due to the size, scalability and proportionate power ranges [28].

The Hydrogen Roadmap Europe [28] is a plan that will radically transform how the EU generates, distributes, stores and consumes energy. Without it, the EU will fail its decarbonisation goals and promises made in the Paris agreement [28][88]. Green hydrogen, also commonly referred to as renewable hydrogen is produced with renewable energy sources. The most used and best known method today is water (H_2O) electrolysis using electricity generated by renewable sources to split the hydrogen (H_2) and oxygen (O_2).

A fuel cell integrated combined cycle power system fuelled with pure hydrogen and using pure oxygen as oxidiser would yield several advantages. First of all, pure hydrogen is a carbon free fuel, resulting in no CO_2 emissions. Secondly, the by-product from the electrolysis, oxygen, is used effectively when used as oxidiser. Third, burning pure hydrogen with oxygen results in no air related greenhouse gasses such as nitrogen oxide since the reaction product is pure steam (H_2O). And last, with the flue gasses being pure steam implies that there is more variety in the integration of combined power cycles, a closed cycle is feasible and there is no need for a stack.

Gas turbine cycles, steam turbine cycles and fuel cells have been investigated greatly throughout the years. Fewer research is conducted on the integration of the three components and especially rare is the research on fuel cell integrated combined cycles fuelled with pure hydrogen and oxygen.

This thesis focuses on the design of a basic and realistic high efficiency power system that generates electricity without harmful emissions which could be realised within an estimated 10 to 20 years of research and development. The proposed power system uses hydrogen and oxygen as fuel and oxidiser to generate electricity, the hydrogen used is assumed to be green. The research question can be formulated as follows:

What is the optimal design for a 3 MWe SOFC integrated hydrogen-oxygen fuelled combined power cycle regarding efficiency and simplicity, feasible within 10-20 years of research and development?

Report outline

Chapter 2 presents the theoretical background required for the design and evaluation of the thermodynamic cycle. First, thermodynamic- and power cycles are introduced as a basis to start upon. Next, the exergy analysis is discussed, this is the method from which the efficiencies are going to be determined and gives a clear image where the losses in the power cycle occur. Thereafter, traditional and combined cycle gas turbine systems are introduced followed by several carbon free power cycles.

Chapter 3 introduces a crucial electrochemical component of the proposed power cycle, the fuel cell. Its working principles, components and performance characteristics are discussed and elaborated. The following part covers the advantages of introducing a solid oxide fuel cell into a power cycle and thus tying the classical thermodynamic and electrochemical components together.

Chapter 4 presents the literature required for a preliminary design of the equipment of the proposed power cycle. The first design steps of the turbomachinery, heat recovery steam generator and heat exchangers are elaborated so that at the end of this report, a basic but complete design of the total power cycle can be presented.

Chapter 5 presents the thermodynamic design of the proposed SOFC integrated combined power cycle. The chapter starts with the design starting points and the selection of operating conditions regarding pressure and temperature. It discusses the relevant topics per subsystem in the cycle and explains the decisions made per component regarding settings or operating parameters. In the end, an exergetic efficiency of the cycle is presented, from which becomes clear where the largest losses in the cycle occur.

Chapter 6 follows up on the results of the exergetic efficiency from chapter five. This chapter proposes an improvement of the basic power cycle focusing on the heat recovery steam generator. The chapter ends with a new exergetic efficiency analysis to reveal the effect of the implemented improvements.

Chapter 7 presents the preliminary equipment design of the turbomachinery, solid oxide fuel cell and both sensible and latent heat exchangers. The chapter provides a practical insight about the size of the proposed cycles and basic design considerations ending with a short comparison with commercial available equipment.

Chapter 8 contains the conclusions of the report together with the recommendations for future research.

2

Thermodynamic power cycle analysis

This chapter contains the literature regarding thermodynamic cycles on which the research is based upon. Subjects such as basic power cycle thermodynamics, exergy, combined cycle gas turbine cycles and zero emission power cycles are discussed and elaborated in the upcoming pages.

2.1. Power cycle thermodynamics

A thermodynamic cycle is a sequence of processes that begins and ends at the same state [55]. The first law of thermodynamics is the conservation of energy principle and is described as the following word statement. "The change in the amount of energy contained within a system during some time interval is equal to the net amount of energy transferred in across the system boundary by heat transfer during the time interval, minus the net amount of energy transferred out across the system boundary by work during the time interval" [55]. Applying this word statement of the first law onto a thermodynamic cycle results in a more delicate and clear formulation depicted in equation 2.1, where Q_{cycle} and W_{cycle} represent the net amounts of energy transfer by heat and work in kW respectively. Equation 2.1 must be satisfied for every thermodynamic cycle, regardless of the process or sequence of processes that make up the system. Figure 2.1 schematically depicts the thermodynamics of a power cycle, the system communicates thermally with a hot and a cold body that are located in the surroundings of the system. During operation, there is an energy transfer between the system and the surroundings by work. The direction of the arrow in figure 2.1 illustrates that the work is done by the system and delivered to the surroundings [55].

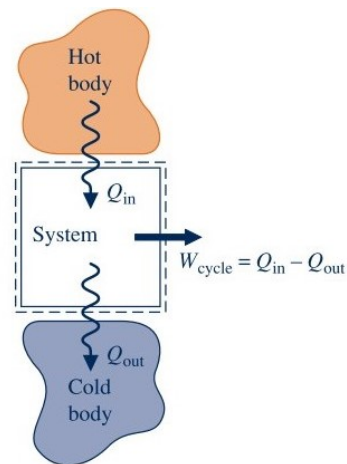


Figure 2.1: Schematic diagram of a power cycle [55]

$$\Delta E_{cycle} = E_{out} - E_{in} = Q_{cycle} - W_{cycle} \quad (2.1)$$

Since the cycle begins and ends in the same state, there is no net change in its energy ($\Delta E_{cycle} = 0$), which reduces the first law to equation 2.2.

$$W_{cycle} = Q_{cycle} = Q_{in} - Q_{out} \quad (2.2)$$

Where Q_{in} represents the heat transfer from the hot body into the system and Q_{out} represents the heat transfer out of the system to the cold body. Thermodynamic cycles that are designed to deliver a net work transfer to their surroundings are called power cycles, it is therefore that the discussed cycles in this research are frequently referred to as power cycles instead of thermodynamic cycles. The thermal performance of a power cycle is determined by the amount of heat converted to a net work output. This theoretical thermal efficiency expresses the extent of the energy conversion from heat

to work by equation 2.3 [55]. Only when power cycles are reversible (*rev*), the ratio of heat transfers Q_{out}/Q_{in} depends solely on the temperatures of the bodies on the Kelvin scale, which is stated in the last step of Eq. 2.3.

$$\eta_{max} = \frac{W_{cycle}}{Q_{in}} = \frac{Q_{in} - Q_{out}}{Q_{in}} = 1 - \frac{Q_{out}}{Q_{in}} \xrightarrow{rev} \eta_{max} = 1 - \frac{T_C}{T_H} \quad (2.3)$$

From this statement can be deduced that when Q_{out} equals zero, the thermal efficiency would be unity (100%). This however, is never the case since only a portion of the heat Q_{in} can be converted into work and the rest must be discharged by heat transfer Q_{out} according to the Kelvin-Planck statement [55].

2.2. Exergy analysis theory

Exergy is the maximum amount of theoretical work obtainable from a system while it comes into equilibrium with its surroundings and reaches the dead state. An exergy analysis is a tool to evaluate thermodynamic processes and their efficiencies. Energy and exergy are two fundamentally different concepts, even though exergy transfer accompanies energy transfer and the two quantities have the same units.

2.2.1. The closed system entropy balance

Where energy is related to the first law of thermodynamics, exergy is related to the second law, and as the first law is described with an energy balance, the entropy balance is regarded as a statement of the second law of thermodynamics. Moran & Shapiro state the entropy balance of the second law as equation 2.4 [55].

$$\left[\begin{array}{l} \text{The change in the} \\ \text{amount of entropy} \\ \text{contained within the} \\ \text{system during some} \\ \text{time interval} \end{array} \right] = \left[\begin{array}{l} \text{The net amount of} \\ \text{entropy transferred in} \\ \text{across the system} \\ \text{boundary during the} \\ \text{time interval} \end{array} \right] + \left[\begin{array}{l} \text{The amount of entropy} \\ \text{produced within the} \\ \text{system during the time} \\ \text{interval} \end{array} \right] \quad (2.4)$$

Expressed in a mathematical statement, the closed system entropy balance is stated by equation 2.5, where subscript b indicates that the integral is taken at the boundary of the system.

$$\Delta S = \int_1^2 \left(\frac{\delta Q}{T} \right)_b + \sigma \quad (2.5)$$

The energy transfer term on the right side of the equation is solely dependent on the heat transfer to or from the system, the term is defined as the "entropy transfer accompanying heat transfer". The same sign convention holds as for energy transfers, a positive value indicates an entropy transfer into the system, a negative value implies a transfer of entropy out of the system. The second term on the right side of Eq. 2.5, defined as the entropy production σ , is either positive or zero but never negative (Eq. 2.6).

$$\sigma : \begin{cases} > 0 & \text{irreversibilities in the system} \\ = 0 & \text{no irreversibilities in the system} \end{cases} \quad (2.6)$$

A positive entropy production indicates that internal irreversibilities are present within the system, which is frequently referred to as entropy generation. The entropy production σ depends on the nature of the process and measures the effect of irreversibilities in the system during a process. The change in entropy ΔS , contrary to the entropy production, can either be positive, zero or negative (Eq. 2.7).

$$\Delta S : \begin{cases} > 0 \\ = 0 \\ < 0 \end{cases} \quad (2.7)$$

Only when the entropy transfer accompanying heat transfer equals zero, the change in entropy is never negative. Holyst & Poniewierski state this second law version more compact as equation 2.8.

The extensive state function entropy, S , whose change in an adiabatic process satisfies the inequality in Eq. 2.8, where the change in entropy is only zero in the case of a reversible process [34].

$$\Delta S \geq 0 \quad (2.8)$$

The second law of thermodynamics describes if a process is reversible or irreversible. In the case of $\Delta S = 0$, the system changes from one state to another through a sequence of equilibrium states, this process is reversible. In the case of $\Delta S > 0$, irreversible changes have occurred in the system or in the surroundings of the system [34]. This means that the system cannot return to its initial state without the addition of energy to the system and implies that the process is irreversible. All natural processes are considered irreversible due to the fact that some "transformation energy" is lost. During the transfer from one state to another, energy will be dissipated due to intermolecular collisions and friction, this energy is impossible to recover and is thus lost. It is therefore that a second law analysis, or exergy analysis gives a better insight in the specific losses such as heat and pressure losses.

2.2.2. Exergy analysis of a system

Energy can be divided into two parts, a part from which useful work can be generated and a part from which this is not possible. The first is the exergy part, the second is frequently referred to as anergy. As previously stated, the exergy of a system is the maximum useful work possible in a process that brings the system into thermal equilibrium with its surroundings [14]. Exergy gives thus a sharper picture of performance compared to energy because exergy expresses all energy transfers on a common basis and accounts explicitly for the effect of irreversibilities through the exergy destruction concept [55]. Exergy analysis in general, will provide more specific knowledge about the losses per component within the system and gives thus an important insight where the most potential for improvement is, it is therefore frequently used for thermodynamic evaluation of power plants. The significance of the analysis however depends strongly on the gained insight in the origin of losses within the system, and thus the options for loss reductions [96]. According to Moran & Shapiro the total exergy of a flow in a system on a unit mass basis is defined by equation 2.9, also referred to as total flow exergy [55].

$$e_{xf} = \underline{(u - u_0) + p_0(v - v_0) - T_0(s - s_0) + \frac{V^2}{2} + gz + e_{xf}^{ch}} \quad (2.9)$$

Where u , v , s , $V^2/2$ and gz are the specific internal energy, volume, entropy, kinetic energy and potential energy at the state of interest respectively. The specific properties at the reference environment are presented by u_0 , v_0 at s_0 at T_0 and p_0 . With the most important term being the enthalpy difference between the system and dead state conditions ($s - s_0$). Exergy, just as energy, is also divided into two parts, the first part of a flow of exergy comes from the chemical exergy e_{xf}^{ch} , as stated at the end of equation 2.9. The standard chemical exergy ($e_x^{o, ch}$) is based on a reference environment with standard pressures (p_0) and temperatures (T_0) of 1 atm and 298.15 K and differs for each element or substance. This research uses the values shown in table 2.1 from the model developed by Szargut, Morris & Steward [95] [55] [6].

Table 2.1: Standard chemical exergy and molecular mass of hydrogen, oxygen and water [6]

Substance	State	Molecular mass M, g/mol	Standard chemical exergy $e_x^{o, ch}$, kJ/mol
H_2	g	2.02	236.09
O_2	g	32.00	3.97
H_2O	g	18.02	9.50
H_2O	l	18.02	0.90

The second part of specific exergy corresponds to the thermomechanical exergy of a flow (e_{xf}^{tm}), this is represented by the underlined terms in equation 2.9. A reformulation of these terms, introducing enthalpy and neglecting the kinetic and potential parts of the equation gives a more elegant formulation of the thermomechanical exergy in equation 2.10.

$$e_{xf}^{tm} = \underline{(h - h_0) - T_0(s - s_0)} \quad (2.10)$$

Now that both exergy terms are defined, the total exergy of a flow can be stated in a clear and simple formulation where e_{xf} represents the maximum amount of work that can be extracted from the flow until the system is at T_0 and p_0 and at rest relative to the environment. This state is referred to as "the dead state", there can be no interactions between system and environment in this state and there is thus no potential for the extraction of useful work. Taking the mass flow into account results in the exergy statement presented in Eq. 2.12.

$$e_{xf} = e_{xf}^{tm} + e_{xf}^{ch} \quad (2.11)$$

$$E_x = \dot{m}e_{xf} \quad (2.12)$$

For every component in a power cycle, an exergy balance can be made to determine how much of the exergy supplied to the component is passed along to the next component and how much is lost. The lost exergy is referred to as exergy destruction and is used as a qualitative evaluation of the component. The rate of exergy destruction (E_d) equals the incoming exergy minus the leaving exergy minus the generated work done or used by the specific component (Eq 2.13).

$$E_d = \sum_{in} E_{in} - \sum_{out} E_{out} - W \quad (2.13)$$

Where the rate of work (W) is positive if it is generated by the component, for example a turbine and negative if work has to be provided to the component for example a compressor or pump. The largest exergy destruction rates in a power cycle occur in the heat addition part of the cycle, most commonly, the combustion chamber. Significant irreversibilities are associated with the chemical combustion reaction and heat transfer across large temperature differences between the combustion gasses and working fluid [24]. After the exergy balances of the individual components in the cycle are determined, a graphical representation of the losses can be made in the form of an exergy value diagram, which give a clear and visual in depth insight about the exergy losses within a system. The exergy flow diagram presents absolute or relative flows and losses in a system without process property relations. An exergy flow diagram is more comprehensive compared to an energy flow diagram, as can be seen in this hot water boiler example provided by Woudstra [95].

A hot water boiler is assumed to consist of a combustion chamber and a heat exchanger, as shown in the diagram in the middle of figure 2.2. The energy flow diagram can be seen on the left side of the figure, where the exergy flow diagram is depicted on the right side of the figure. The two fundamental processes within the boiler are the assumed adiabatic combustion and heat transfer from hot flue gasses to the water. The overall thermal efficiency is stated as 93%, this is stated by the energy flow diagram on the left. But after taking into account the exergy losses in combustion and heat transfer, the overall exergy efficiency results in only 14.5%. The comparison between the energy and exergy flow diagrams of the same hot water boiler show that the evaluation of energy conversion system based only on thermal or other single types of energy values can be extremely misleading [95].

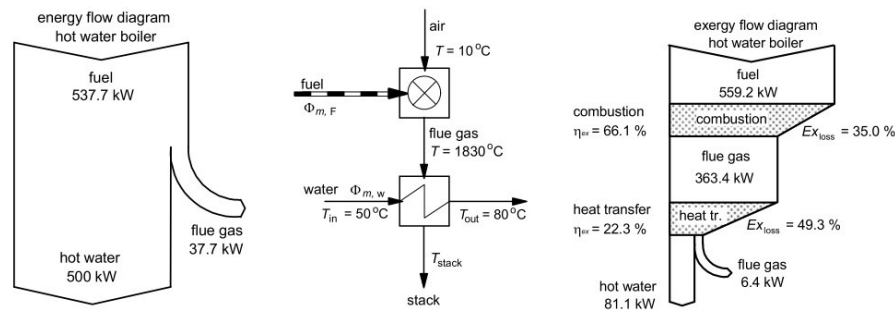


Figure 2.2: Energy flow diagram, system diagram & exergy flow diagram of a hot water boiler [95]

2.3. Classic thermodynamic cycles

Introducing two basic thermodynamic cycles which are considered building blocks for air and steam power cycles, after the introduction of the cycles their corresponding governing equations are discussed.

2.3.1. Joule-Brayton cycle

The Joule-Brayton cycle, also referred to as "Brayton cycle" describes the continuous process of a constant-pressure heat engine. In the old days, the cycle used piston compressors and piston expanders, nowadays modern gas turbines and jet engines follow the same cycle principles. A gas turbine is a continuous combustion engine in which an energy conversion takes place to convert the chemical energy from the fuel into work. The open Brayton cycle consists of three components: a compressor, a combustion chamber and an expander. The closed cycle consists of an additional heat exchanger, both the open and closed cycle are depicted in figure 2.3.

The working principle of the cycle is as follows: air is continuously drawn into the compressor where it is compressed to the desired pressure. The compressed air then enters the combustion chamber where fuel is added, the pressurised air and fuel ignite and create hot flue gasses. The flue gasses then go through the expansion stage in a turbine, where work is extracted. A part of the extracted work is used to drive the compressor since both components are connected to the same shaft. After the turbine stage, the flue gasses can be released into the atmosphere, having an open cycle, or send through a heat exchanger where the heat of the medium is rejected before entering the compressor again, creating a closed cycle. Some of the assumptions the ideal cycle makes are the use of ideal gasses as working medium, resulting in constant C_p and C_v values, negligible kinetic and potential energy losses between the in- and outlet of the components and isentropic compression and expansion stages. The ideal cycle can be summarised in the following four parts, the referred processes are depicted in the temperature-entropy diagram of the medium in figure 2.4. Figure 2.4 schematically displays the temperature and entropy changes of the medium for both the ideal and the real process.

1. Isentropic compression, process 1-2s.
2. Isobaric heat addition, process 2s-3.
3. Isentropic expansion, process 3-4s.
4. Isobaric heat rejection, process 4s-1.

The real Brayton cycle does not include isentropic processes, implying that the compression and expansion stages (1 & 3) are never without an entropy increase. The compressor and turbine operate adiabatic instead of isentropic, meaning that there is no heat loss to the surroundings and that the real closed cycle is presented by the curves connecting point 1-2-3-4-1 in figure 2.4 [55] [91]. The maximum temperature occurs after the combustion process and is limited by the maximum temperature of the turbine blades. This also limits the pressure ratio and the maximum efficiency of the cycle [91].

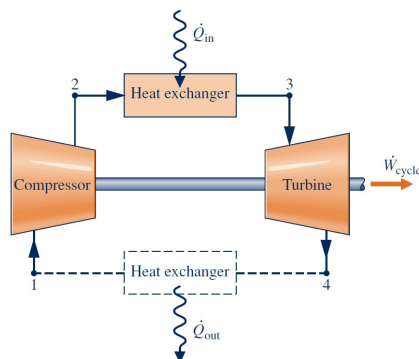


Figure 2.3: Diagram of the basic open or closed Joule-Brayton cycle [55]

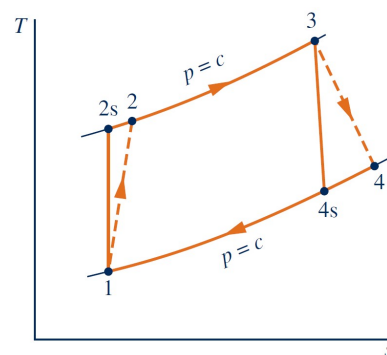


Figure 2.4: Schematic T-s diagram of the basic Joule-Brayton cycle [55]

2.3.2. Rankine cycle

Where the Brayton cycle is the typical air power cycle, the Rankine cycle is a standard vapour/steam power cycle and the basic building block of vapour power plants [55]. It is a closed thermodynamic cycle that converts heat into work while the working medium undergoes a phase change. The common cycle consists of the four principle components depicted in figure 2.5, the turbine, condenser, pump and boiler.

The working principle of the cycle is as follows: starting at low pressure and low temperature working medium conditions (point 3 in figures 2.5 and 2.6), the water is pumped from low to high pressure. After the pump, the high pressure liquid enters the boiler where heat is added to the working medium under constant pressure. Once it leaves the boiler, the medium is now a high temperature high pressure dry saturated vapour. The vapour then expands through a steam turbine, where work is extracted. In this process, the medium decreases in temperature and pressure, resulting in a medium change from dry to wet vapour. After the expansion process in the turbine, the wet vapour is condensed in a condenser making it a saturated liquid again and completing the closed cycle [55]. The ideal cycle considers friction losses negligible and heat transfers to the surroundings as nonexistent. The cycle can be summarised in the following four parts in the same order as just stated. The referred processes are depicted in the temperature-entropy diagram of the medium in figure 2.6. The diagram schematically displays the temperature and entropy changes of the medium for both the ideal and the real process.

1. Isentropic compression, process 3-4s.
2. Isobaric heat addition, process 4s-1.
3. Isentropic expansion, process 1-2s.
4. Isobaric heat rejection, process 2s-3.

As discussed in the Joule-Brayton cycle, processes are never ideal and thus, losses are inevitable. Loss contributions in the real cycle are caused by fluid friction in the components and heat losses to the surroundings. Friction losses in the turbomachinery are considered primary since these have the most severe effect on the efficiency decrease, these losses are depicted by the dotted lines in figure 2.6. Heat losses to the environment are considered secondary and not presented in the schematic T-s diagram.

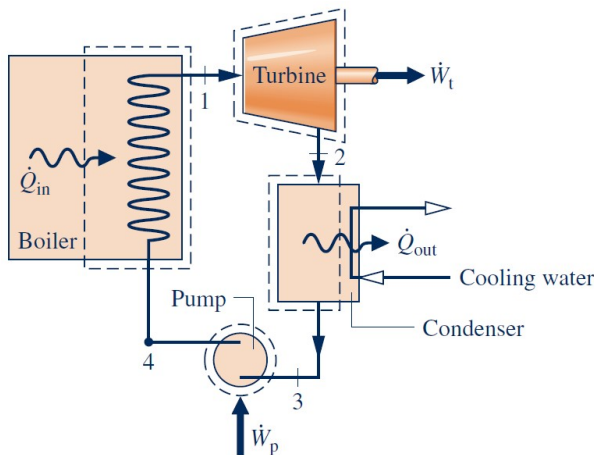


Figure 2.5: The basic Rankine cycle with its four principle components [55]

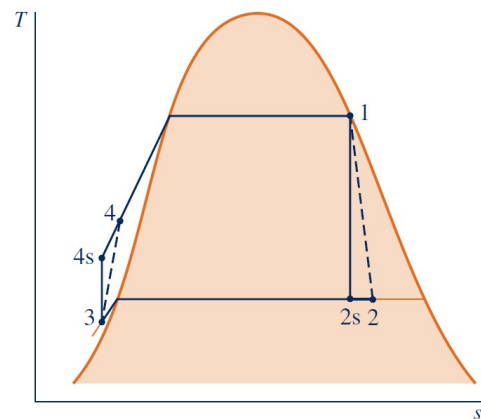


Figure 2.6: Schematic temperature-entropy diagram of the basic Rankine cycle [55]

2.3.3. Governing power cycle equations

The irreversibilities and losses in the cycles are associated with the principal four components, where the one has a much larger effect on the power cycle performance than the other. Although the Brayton and Rankine cycle have a lot of differences, they do share fundamental, basic governing thermodynamic principles. These equations, stated by Moran & Shapiro, are now presented per cycle component [55]. The mass and energy rate balance is specified for a control volume around the turbine. The mass and energy rate balance denoted in Eq. 2.14 neglects the effects of heat loss to the surroundings, together with kinetic and potential effects.

$$0 = \dot{Q}_{cv} - \dot{W}_t + \dot{m} \left[h_{in} - h_{out} + \frac{V_{in}^2 - V_{out}^2}{2} + g(z_{in} - z_{out}) \right] \quad (2.14)$$

Resulting in equation 2.15 where the work is defined per unit of mass of the working fluid.

$$\frac{\dot{W}_t}{\dot{m}} = h_{in} - h_{out} \quad (2.15)$$

With h_{in} as the enthalpy entering the turbine and h_{out} as the outlet enthalpy in kJ/kgK . All four principle components of the cycle are calculated with mass and energy rate balances, assuming adiabatic operation and neglecting kinetic and potential energy effects. Stating the crossed out terms of the mass and energy rate balances for each component was considered redundant due to the similarity of the balances, only the results per component are therefore shown. The isentropic efficiency of the turbine shown in equation 2.16 and is defined as the ratio of actual work developed by the turbine over the theoretical work possible developed during isentropic expansion.

$$\eta_t = \frac{\left(\frac{\dot{W}_t}{\dot{m}}\right)}{\left(\frac{\dot{W}_t}{\dot{m}}\right)_s} = \frac{h_{in} - h_{out}}{h_{in} - h_{out,s}} \quad (2.16)$$

The method for determining the work required for the compressor or pump is similar as equation 2.15, the difference is that the work per unit mass is now considered as input instead of output, this is stated in equation 2.17.

$$\frac{\dot{W}_{c,p}}{\dot{m}} = h_{out} - h_{in} \quad (2.17)$$

The isentropic compressor or pump efficiency is defined as the work needed for the isentropic process divided by the actual work done by the compressor or pump resulting in equation 2.18.

$$\eta_{c,p} = \frac{\left(\frac{\dot{W}_{c,p}}{\dot{m}}\right)_s}{\left(\frac{\dot{W}_{c,p}}{\dot{m}}\right)} = \frac{h_{out,s} - h_{in}}{h_{out} - h_{in}} \quad (2.18)$$

The heat added in the combustor is given per unit of mass by equation 2.19.

$$\frac{\dot{Q}_{in}}{\dot{m}} = h_{out} - h_{in} \quad (2.19)$$

The rejected heat per unit of mass is given by equation 2.20, this corresponds to the cooling of the air in the heat exchanger of the closed Brayton cycle (process 4-1 fig 2.4) and the heat discharged in the condenser in the Rankine cycle (process 2-3 fig 2.6).

$$\frac{\dot{Q}_{out}}{\dot{m}} = h_{out} - h_{in} \quad (2.20)$$

The thermal efficiency is defined as the work generated by the cycle, minus the work put into the cycle divided by the heat provided to the cycle, stated in Eq. 2.21.

$$\eta_{th} = \frac{\sum \frac{\dot{W}_t}{\dot{m}} - \sum \frac{\dot{W}_{c,p}}{\dot{m}}}{\sum \frac{\dot{Q}_{in}}{\dot{m}}} \quad (2.21)$$

2.4. Combined cycle power plants

A combined cycle power plant is a combination of heat engines using the same heat source that convert the supplied heat into power. The most commonly used combined cycle for electricity production is referred to as the combined cycle gas turbine, where the discharged heat from the gas turbine is used partly or wholly as heat input for the bottoming cycle. This principle is schematically displayed in figure 2.7 where the waste heat of the top cycle is transferred to the bottom cycle in a heat recovery steam generator HRSG. The combined gas turbine-vapour power cycle combines the high temperature heat supply from the Brayton cycle with the low temperature heat rejection from the Rankine cycle, resulting in a greater efficiency either one could have individually [55]. The thermal efficiency of the overall cycle is calculated as the summation of the extracted net work from both gas and vapour cycles over the total heat addition to the combined cycle, stated in Eq. 2.22.

$$\eta_{th} = \frac{\dot{W}_{gas} + \dot{W}_{vap}}{\dot{Q}_{in}} \quad (2.22)$$

Where \dot{W}_{gas} is defined as the net power developed by the air cycle ($\dot{W}_{gt} - \dot{W}_c$) and \dot{W}_{vap} is defined as the net power developed by the vapour cycle ($\dot{W}_{st} - \dot{W}_p$). An important parameter of this tandem cycle configuration is the heat recovery steam generator since this device transfers the energy from the gas cycle to the steam cycle. A first insight in the energy transfer is determined by the means of a mass and energy balance for a control volume enclosing the HRSG. Such a balance is stated in equation 2.23 where steady state operating conditions, non existing heat transfer to the surroundings and no changes in kinetic and potential energies are assumed [55].

$$\dot{m}_v(h_{out} - h_{in}) = \dot{m}_g(h_{in} - h_{out}) \quad (2.23)$$

Where \dot{m}_v and \dot{m}_g account for the mass flow rates of the vapour and gas streams respectively. A more in-depth insight in the HRSG and its operating characteristics is given chapter 4.3.

When comparing individual cycle efficiencies to their combined alternative explains why combined cycles are so widely used for electricity production. A basic gas turbine cycle achieves energy conversion efficiencies of approximately 20% to 35% [56]. The typical steam power plant efficiency is somewhat higher and ranges between 35% and 50% [55]. State-of-the-art combined gas and vapour cycles nowadays reach thermal efficiencies of 62% and slightly above [32][56]. Important parameters for the combined cycle efficiency are the gas turbine inlet temperature and the pressure ratios in the compressor and gas turbine. A higher turbine inlet temperature (TIT) results in a higher turbine outlet temperature and thus, more heat can be transferred to the bottoming cycle. This cascade of heat results in optimal use of the exergy in the medium and results in more work extracted from the medium. The top and bottom cycle work output thus increases with increasing gas turbine inlet temperature, as a result the combined cycle work output increases [65]. A higher pressure ratio results in more work extracted in the top cycle but comes with larger exergy destruction rates for the components. A higher PR results in more entropy generation related irreversibilities for both the compressor and turbine [65].

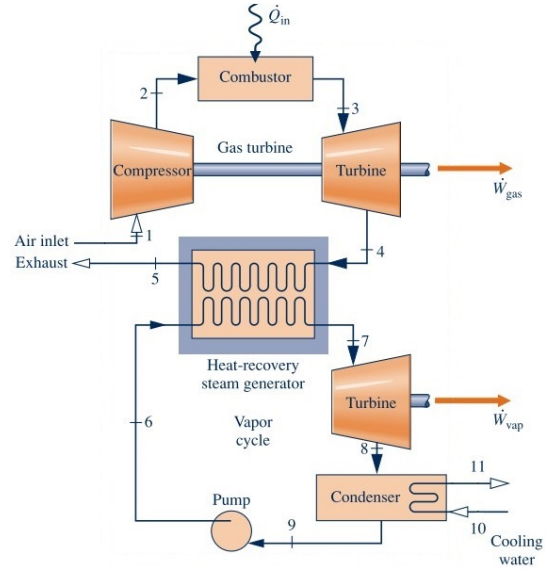


Figure 2.7: Schematic diagram of a combined gas turbine-vapour power plant [55]

2.5. Zero emission power cycles

Classical thermodynamic cycles such as the Joule-Brayton and the Rankine cycle are traditionally fuelled with fossil fuels, whereas for future power generation, zero emission methods are required to stop climate change. This subchapter presents different cycles and their methods for carbon free power production such as oxy-fired gas turbines and H_2 - O_2 fuelled cycles.

2.5.1. The Graz cycle

The Graz power cycle arose when the international treaty of the 1992 United Nations Framework Convention on Climate Change (UNFCCC) was extended in 1997 and was hereafter referred to as the Kyoto Protocol [87]. It set its targets to power future energy with sustainable sources to reduce greenhouse gas emissions. The Graz cycle originally burned fossil fuels with pure oxygen which enabled cost-effective separation of the combustion CO_2 by condensation [39]. Years later, the cycle was adapted for the burning of hydrogen, reaching efficiencies up to 70% and higher [40][71]. The cycle is a combination of a high temperature Joule-Brayton cycle and a low temperature Rankine cycle, where the Rankine cycle serves as a heat sink for the Brayton cycle. It is thus a variant of a standard combined cycle where hydrogen is used as fuel and pure oxygen is used as oxidiser, creating pure steam as combustion product and working fluid in the cycle. High temperature steam is formed in the combustor, which is then expanded in a high temperature turbine (HTT) where the waste heat after expanding is transferred to the bottoming Rankine cycle via a Heat Recovery Steam Generator (HRSG). The steam coming from the stack of the HRSG is now either send to a low pressure turbine (LPT) or to the compressor after which the pressurised steam acts as a cooling medium for the combustor. The compressor ensures an extra degree of freedom (DOF) in the cycle, this extra DOF enables a better energy balance over the HRSG and thereby a lower temperature difference in the heat transfer in the HRSG resulting in lower exergy losses [73]. Figure 2.8 shows the principle flow scheme of the cycle where the Brayton part consists of the combustor, HTT and the compressors (C1 & C2) and the Rankine steam loop consists of the HRSG, HPT, LPT, condenser, condensate pump, deaerator and the HRSG feed pump. The cycle arrangement offers several advantages over conventional power cycle arrangements. High thermal efficiencies can be achieved due to the allowed high temperature heat input combined with expansion processes approaching vacuum conditions, which results in high thermal efficiencies. Another big advantage versus more conventional combined power cycles is that a large amount of steam is send back to the compressor before condensing, meaning not releasing its heat of vaporization and taking this high heat content back into the combustion chamber, resulting in a significant efficiency increase. The integration of the Brayton and Rankine cycle however make it more complex to operate, especially considering part load conditions [71].

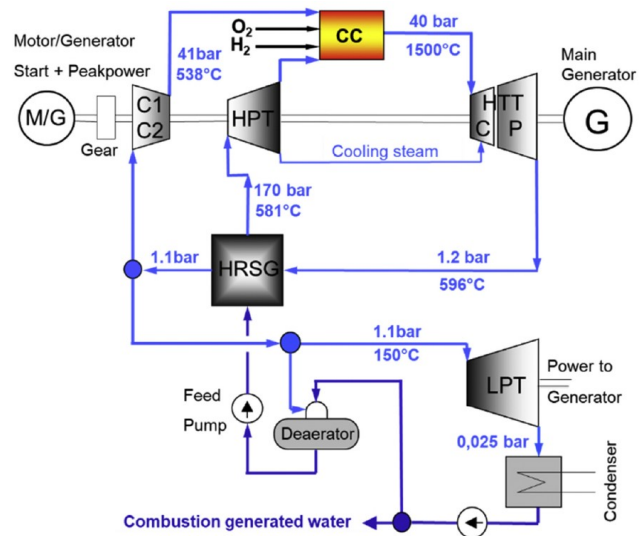


Figure 2.8: Principle flow scheme of the adapted Graz cycle, suitable for hydrogen/oxygen combustion [71]

2.5.2. Allam cycle

Another example of a carbon free cycle is the Allam cycle, also referred to as the NET cycle. The Allam cycle is an oxy-fuel cycle which uses CO_2 at supercritical conditions without the use of a bottoming cycle, relatively recent proposed by Allam et al. in 2010 [5]. The carbon dioxide is compressed in a multi stage intercooled compression system reaching pressures of 200-400 bar. It is then heated via a recuperator before entering the combustion chamber so it has an approximate combustor inlet temperature of 700 to 750°C. The heat transferred in the recuperator comes from the high pressure CO_2 turbine outlet in the cycle. The combustor uses natural gas as fuel and pure oxygen as oxidiser, delivered by an Air Separation Unit (ASU), thus operating under oxy-firing conditions and leading to combustor outlet temperatures of 1100 to 1200 °C. This high pressure high temperature medium is expanded in the turbine beyond the critical point of the CO_2 after which a part of the heat content is transferred to the cold CO_2 stream in the recuperator. After the water is separated from the stream, the carbon dioxide is again compressed after which a mass fraction is sent back in the system and the remaining part is used for storage and/or other uses such as for instance EOR (Enhanced Oil Recovery) [5].

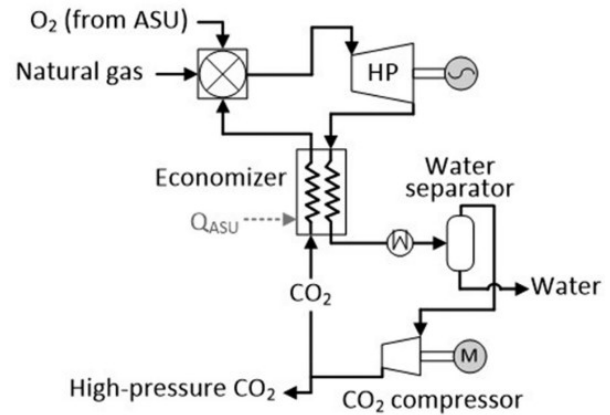


Figure 2.9: Schematic flow scheme of the oxy-fired gas variant Allam cycle [5]

2.5.3. Hydrogen-oxygen cycles

The traditional power cycles previously discussed, the Joule-Brayton cycle and the Rankine cycle have different working media. The Joule-Brayton cycle is the typical gas turbine cycle where fuel such as natural gas or kerosene is burned with compressed air resulting in a gaseous working medium. The Rankine cycle is different since it uses a closed system of water/steam as a working medium to convert heat into work. The heat applied to the cycles is most commonly generated by the combustion of fossil fuels. The chemical reaction that takes place when burning fossil fuels with air leads to unwanted and unavoidable fuel related emissions such as CO_2 and air related emissions such as NO_x at high temperatures. NO_x and CO_2 formation are significant problems in a world wide battle against climate change and air pollution. The ideal complete fossil fuel combustion reaction with stoichiometric air-to-fuel ratio will always have carbon dioxide as a reaction product and burning hydrocarbons will therefore never be the solution for greenhouse gas reduction. Hydrogen-oxygen cycles use pure hydrogen as fuel and pure oxygen as oxidant. Focusing on the stoichiometric combustion of H_2 and O_2 in a Brayton cycle results in only water/steam (H_2O) as a product which is the working fluid of the Rankine cycle. The combustion reaction of hydrogen-oxygen cycles stated in Eq. 2.24 show no undesired greenhouse gasses and other undesired emissions compared to hydrocarbon combustion.



Hydrogen-oxygen cycles are relatively young compared to conventional power cycles and are only studied since the late twentieth century [73]. One of the most important international projects for hydrogen utilization was "The International Clean Energy Network Using Hydrogen Conversion", also called the "WE-Net" program (World Energy Network) constructed in 1993. The goal of WE-NET was to construct a renewable energy network using hydrogen for effective supply, transportation and utilisation on a worldwide scale [54]. This program predicted the implementation of the Hydrogen-Fuelled Combustion Turbine Cycle (HFCTC) as an opportunity for new power production methods. The most important proposed HFCTC concepts are stated below with their corresponding main performance parameters stated in table 2.2, one of which being the Graz cycle previously discussed [51] [50].

1. Combined Steam Cycle with Steam Recirculation initially proposed by prof. H. Jericha (Technical University of Graz) and further developed by Sanz et al. by convention called **the Graz cycle**.
2. Direct-Fired Rankine Steam Cycle (New Rankine Cycle), which was studied in the following variants.

- (a) Proposed by Toshiba Co., by convention called **the Toshiba cycle**.
- (b) Proposed by Westinghouse Electric Co., by convention called **the Westinghouse cycle**.

Table 2.2: Main performance parameters of the discussed carbon free cycles in nominal conditions

Cycle	p_{max} bar	T_{max} °C	η_{LHV} %	$\eta_{e,LHV}$ %
Allam [5]	400	1200	58.8	57.3
Graz [71][73]	350	1700	70.8	69.0
Toshiba [73]	380	1700	71.2	69.4
Westinghouse [51][50]	250	1700	70.9	69.1

Where each of the H_2 - O_2 concepts reaches LHV efficiencies η_{LHV} of 70% LHV and over [73]. The concept most favoured by the WE-NET Program turned out to be the Graz cycle due to multiple advantages over the other concepts. One of which being the relatively low pressure regime in the high temperature areas. The cycle does however have several disadvantages such as the complicated heat exchanger network and steam compressor [51].

Toshiba & Graz cycle improvements

Previous research conducted at the TU Delft by Schouten [72][73] showed that there are still improvements that can be implemented in the Toshiba and Graz cycles resulting in higher LHV efficiencies. The focus of this research was to develop improvements to the existing Toshiba and Graz cycle with the additional application of solid oxide fuel cells by the means of an exergy analysis. Several improvements are suggested such as an increase in turbine inlet temperature, the use of a reheat combustor, condensate preheating and a hybrid cooling system for turbine blades to cope with the elevated temperature. With these improvements, the maximum efficiency of the improved Graz and Toshiba cycles reach 75% LHV.

Apart from the thermodynamic improvements, the addition of fuel cells to the turbine cycles was also investigated for the electrochemical improvement. Multiple novel integrated systems were investigated where the cycles were equipped with a single fuel cell or the configuration where three fuel cells are positioned in series. The triple fuel cell design combined with the thermodynamic improvements elevated the Graz cycle efficiency to a potential 84% LHV [73].

The results of this research are incredibly promising for future power generation, the improved cycles developed by Schouten [73] are however extremely complicated and suggest operating conditions not yet proven possible. Nonetheless, the integration of fuel cells in power cycles are proven to be an excellent solution as a method for efficiency increase of power cycles. The Siemens-Westinghouse cycle [33][49] developed the first small scale all electric SOFC micro-gas turbine system with theoretical efficiencies reaching 80%. Nakata et al. investigated different energy systems of varying system sizes and came up with the efficiency function presented in figure 2.10, from which the same conclusion can be drawn: a fuel cell addition to a turbine cycle is explicitly favourable [56].

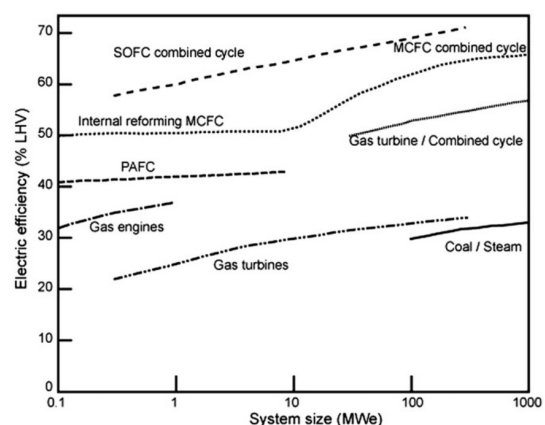


Figure 2.10: Electric efficiency as a function of the rated load for a fuel cell power plant compared with thermal power plants [56]

3

The Solid Oxide Fuel Cell

This chapter describes the literature regarding the solid oxide fuel cell. The basic principles are discussed first, followed by an elaboration about its components and the governing equations and reaction kinetics. The last part of this chapter covers the advantages of integrating a SOFC into a power cycle.

3.1. Fuel cell principles

A fuel cell is a device that converts the chemical energy of a fuel directly to electrical energy and heat without combustion. Without combustion, significantly higher conversion efficiencies are achieved compared to conventional thermomechanical methods. A fuel cell consists of a negatively charged electrode (anode) and a positively charged electrode (cathode) separated by an electrolyte. The method via which a fuel cell generates electricity is similar as for batteries. A large advantage of a fuel cell compared to batteries is that a fuel cell does not run down or require recharging, it operates as long as there is enough fuel and oxidant provided to the cell. The most widely used and developed fuel cell type is the Solid Polymer Fuel Cell, also known as the Proton Exchange Membrane Fuel Cell (PEMFC), depicted in figure 3.2. The PEMFC was first developed by General Electric in the 1960s for the first manned space missions by NASA. The mobile ion in the polymers is the H^+ ion that moves through the electrolyte from the anode to the cathode. The cell has a low operating temperature of approximately 100°C , which has the advantage of short start-up times [43]. Another type of fuel cell is the solid oxide fuel cell, a schematic representation of the electrochemical process of a SOFC is depicted in figure 3.1. The ions transported through the electrolyte are O^{2-} ions that transfer from the cathode to the anode. SOFCs can operate at high temperatures reaching 1000°C , it allows the fuel cell to reform the fuel internally, which enables the use of a wide variety of fuels and reduces the costs in the system.

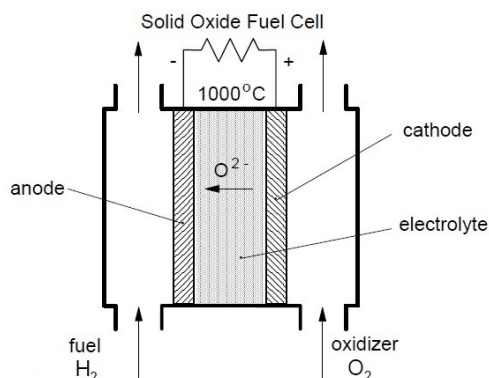


Figure 3.1: Schematic of the basic working principle of a SOFC fuelled by H_2 and O_2 [48]

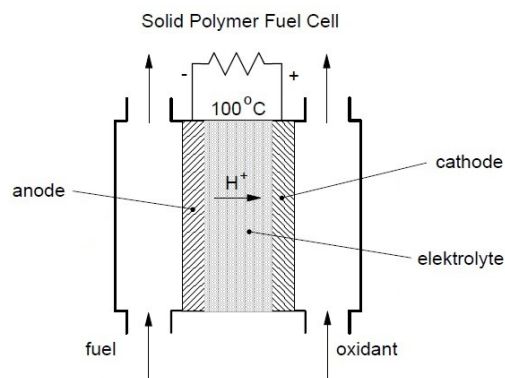


Figure 3.2: Schematic of the basic working principle of a SPFC/PEMFC [48]

The type of fuel cell is classified by the electrolyte material, this determines the electrochemical reactions taking place in the cell, the range of operating temperature, the required fuel and several

other factors. An overview of currently used and developed fuel cell types is stated in table 3.1, where the abbreviations represent: Polymer Electrolyte Membrane (PEM), Alkaline (AFC), Phosphoric Acid (PAFC), Molten Carbonate (MCFC) and Solid Oxide (SOFC). The electrical efficiency stated in the table is an approximate maximum LHV efficiency [27].

Table 3.1: A comparison of fuel cell technologies [9][27][43][45]

Fuel Cell Type	Common Electrolyte	Operating Temperature	Typical stack size	Ion transfer	Electrical efficiency
PEM	Perfluorosulfonic acid	<120°C	<1-100 kW	H^+	40-60%
AFC	Aqueous potassium hydroxide soaked in a porous matrix, or alkaline polymer membrane	<100°C	1-100 kW	OH^-	60%
PAFC	Phosphoric acid soaked in a porous matrix	150-200°C	5-400 kW	H^+	40%
MCFC	Molten lithium, sodium, and/or potassium carbonates, soaked in a porous membrane	600-700°C	300-3000 kW	CO_3^{2-}	50%
SOFC	Yttria stabilised zirconia	500-1000°C	1-2000 kW	O^{2-}	60-65%

Hydrogen-oxygen fed SOFC

When a fuel cell, in this case a SOFC is operated with hydrogen as fuel and pure oxygen as oxidiser, the hydrogen (H_2) is fed at the anode side where oxygen (O_2) is supplied at the cathode side of the cell. The reacting of hydrogen with negatively charged oxygen ions at the anode results in the forming of steam. During this chemical reaction, two negatively charged electrons e^- are released, as stated in Eq. 3.1. Due to the reaction at the anode side, a concentration gradient is formed over the electrolyte which drives the oxygen ions from the cathode to the anode through the electrolyte. The electrons released from the anode side reaction react with the supplied oxygen at the cathode due to a connected wire between the anode and cathode, forming negatively charged oxygen ions O^{2-} at the cathode side (Eq. 3.2). Since a flow of electrons passes through the wire, electrical power is generated [80]. The electrochemical reaction at the anode side is stated as Eq. 3.1.



The electrochemical reaction at the cathode side is defined as Eq. 3.2.



The overall reaction with stoichiometric ratio of hydrogen to oxygen 2:1 is the combined anode and cathode chemical reaction and is stated as Eq. 3.3.



The electrochemical fuel cell principle has higher combined thermal & electrical efficiencies compared to conventional combustion engines since it is not limited by the Carnot efficiency. The SOFC realises its power from the energy released during the overall reaction 3.3, however, not all energy can be converted to useful electric power, the unwanted byproduct is the heat generated by the exothermic reaction. The maximum efficiency of a fuel cell is limited by the ratio of available Gibbs free energy and the enthalpy released stated in Eq. 3.4.

$$\eta_{max} = \frac{\Delta G_r}{\Delta H_r} = \frac{\Delta H_r - T \Delta S_r}{\Delta H_r} \quad (3.4)$$

Where the enthalpy change is ΔH_r , which is the total available thermal energy from the chemical reaction at given temperature. The Gibbs free energy ΔG_r is the enthalpy change minus the amount of heat produced during the reaction ($T \Delta S_r$), with T as operating temperature and ΔS_r the entropy

change [12]. The subscript r implies that a chemical reaction is involved [83]. From Eq. 3.4 can be concluded that increasing the operating temperature of a fuel cell has a negative effects on the maximum efficiency since it lowers the Gibbs free energy. This phenomena is depicted in figure 3.3 together with the temperature dependence of the maximum efficiency of a standard heat engine (Eq. 2.3) and an integration of the two systems. This figure makes particularly clear that when a fuel cell is coupled with a heat engine, the fuel cell can operate at elevated temperatures and reach its ambient temperature maximum efficiency, which makes the integration of a fuel cell and heat engine system especially advantageous [43].

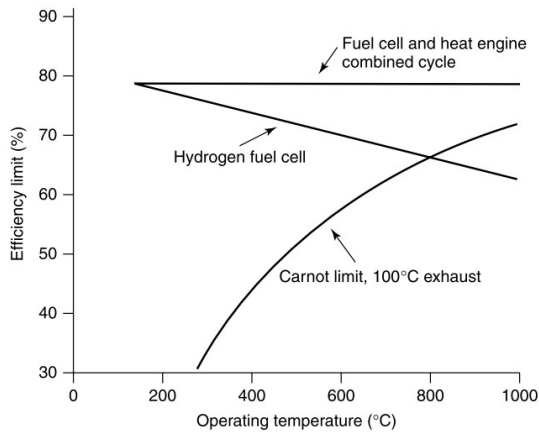


Figure 3.3: Efficiency limit comparison of a Carnot process, a fuel cell and a FC integrated CCGT cycle [43]

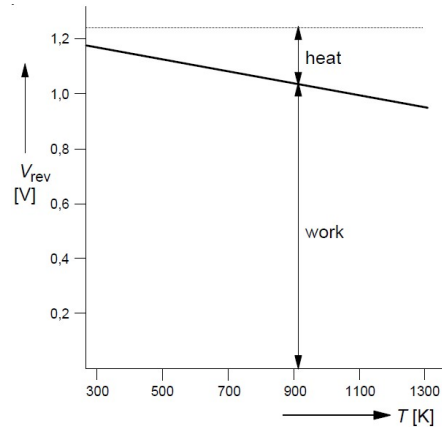


Figure 3.4: Theoretical Temperature-Voltage curve of a single cell [11]

Figure 3.4 depicts the theoretical representation of the linear decrease in cell voltage output with increasing operating temperature. A standalone SOFC system only uses the "work part" of the curve, whereas in a fuel cell and heat engine combined cycle, the heat is used efficiently as well.

3.2. SOFC Components

The SOFC components such as the anode, electrolyte and cathode are further explained in the upcoming part together with the interconnect material and sealing. Some of the advantages of the SOFC are high achievable efficiencies, fuel flexibility and the fact that the electrolyte is solid. The largest disadvantage is the high operating temperature of the SOFC, this results in large temperature gradients and an increase in thermal stresses. With this come higher material costs, corrosion of the materials and breakdown of cell components together with the expected lifetime of the system [27]. The majority of SOFCs constructed today are of a planar (figure 3.5) or tubular (figure 3.6) configuration, each coming with its advantages and disadvantages. Selecting the best configuration is based on basic design considerations such as the required power, size, weight, response and operating conditions.

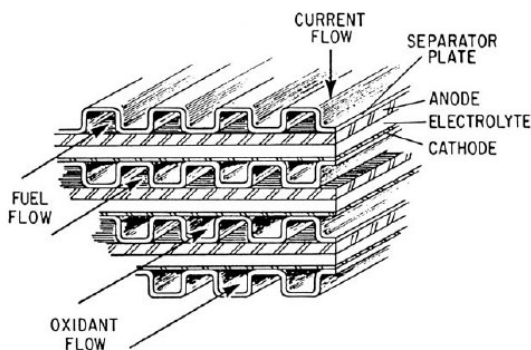


Figure 3.5: Flat plate fuel cell stack with parallel flow [11]

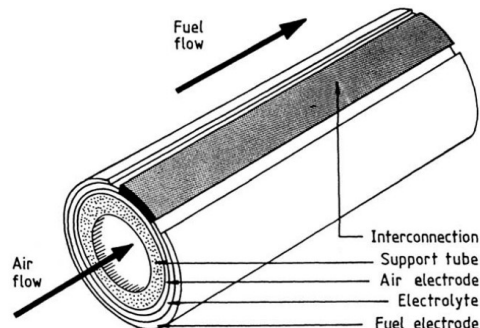


Figure 3.6: Tubular fuel cell design from Siemens-Westinghouse [11] [33]

Anode

The SOFC anode is a composite material that is made out of ceramic (cer) and metal (met), defined as a cermet. The metallic part of the anode is usually made out of nickel because of its high electronic conductivity and stability under part-reducing and chemically reducing conditions. The ceramic skeleton is generally made from Yttria-stabilized zirconia (YSZ), this prevents sintering of the nickel and has a thermal expansion coefficient that is similar to that of the electrolyte. When a fuel cell operates at lower temperatures, other materials have to be considered due to the YSZ operating temperature of 800-1000°C [3]. Gadolinia-doped ceria (CGO) is a proven material alternative for low temperature operation, where operating temperatures below 600°C result in competitive levels of efficiency compared to its high temperature YSZ alternative [3]. The mass transport of the reactant and product gases is not inhibited due to the high porosity of the anode material (20-40%) [43]. There are however some losses at the interface between the electrolyte and the anode, the so called contact losses between the components. The requirements for high quality anodes are a high electrical conductivity, high electrocatalytic activity for fuel oxidation and chemical stability in a reducing environment [11]. The electrochemical reaction stated in equation 3.1 occurs in the presence of three phases at the anode-electrolyte boundary, these triple phase boundaries are thus the electrochemically active parts of the anode.

Electrolyte

The high operating temperature of the SOFC is to ensure high ion conductivity in the electrolyte and thus to prevent high resistance losses (further elaborated in chapter 3.3) associated with the electrolyte material. The best suited electrolyte material thus depends on the operating temperature of the cell, the most effective electrolyte for SOFC's operating at high temperatures are zirconia doped with 8% to 10% mole Yttria-stabilised zirconia. The highly stable zirconia is the most optimal material in both reducing and oxidising environments for the anode and cathode conditions [43]. The conduction of O^{2-} ions in HT-SOFCs is achieved via a system where some of the Zr^{4+} ions are replaced by Y^{3+} ions in the fluorite crystal structure of the zirconia. This ion exchange results in a number of vacant sites for oxide-ions because of three O^{2-} ions replacing four O^{2-} ions. The electrolyte can be made extremely thin to ensure that the ohmic loss of the SOFC is as low as possible. For low temperature fuel cells, CGO is used, which has a far higher ionic conductivity compared to YSZ, which in turn allows the operating temperature to drop to 500°C. The downside to CGO is that it is less chemically stable which eventually leads to an internal short-circuit in the cell, resulting in open circuit cell voltage- and efficiency losses [45].

Cathode

The cathode is made from a porous material similar to the anode that allows fast mass transport of product and reactant gasses. Most commonly used material is a p-type semiconductor made from strontium-doped lanthanum manganite ($La_{0.84}Sr_{0.16}MnO_3$). Other compliant options are p-type conducting perovskite structures that exhibit ionic conductivity as well as electronic conductivity. When the temperature of the SOFC is lowered, the polarisation of the cathode increases significantly and is therefore important for the overall efficiency [43].

Interconnect material

The means by which connection to the neighbouring cells is accomplished is called the interconnect or bipolar plate. Metals can be used for these kind of applications, but the downside is that only expensive austenitic nickel-chromium-based super alloys so called "incone" stainless steels can withstand the regular operating temperature of 800 to 1000°C [43]. Widely used steels also have the disadvantage that the thermal expansion coefficient is not a match with the YSZ electrolyte and tend to form oxide coatings, which limits the electrical conductivity and has negative consequences regarding mass transport. For tubular designs, ceramic material is favoured for the interconnect, especially lanthanum chromite. The downside is that this material needs to be sintered to high temperatures to produce a dense phase, which brings to light one of the major challenges of a SOFC, the fabrication.

Fabricating the compatibility between all the cell components with respect to mechanical compliance (thermal expansion coefficients) and chemical stability has proved itself to be difficult. A balance has to be found between finding a sintering temperature that ensures good adherence but not too high of a temperature such that the material starts to degrade [43] [11].

Sealing

To ensure that the SOFC is gas tight, sealing of the ceramic components is essential, this is a key issue in fabricating (especially planar) SOFC's. The material most widely used is glass with transition temperatures close to the operating temperature of the fuel cell. When the fuel cell operates, this glass softens and creates a seal around the cell. There are however problems that can occur, such as the migration of silica from such glass types, specifically onto the anodes which causes a decline in cell performance [43].

3.3. SOFC performance & characteristics

The objective of a Solid Oxide Fuel Cell, or any other fuel cell is to deliver power P to the load, which in an electrochemical device is the voltage E times the current I (Eq. 3.5).

$$P = EI \quad (3.5)$$

For every mole of hydrogen, two moles of electrons pass through the electric load, to convert this electron flow, the Faraday constant must be used. The voltage of a fuel cell directly affects the power output, the maximum voltage, or theoretical value of the open circuit voltage (OCV) is determined via the Gibbs Free Energy and the Faraday constant via equation 3.6.

$$E_0 = -\frac{\Delta G_r}{nF} \quad (3.6)$$

The operating conditions such as the pressure, temperature and concentration affect the Gibbs free energy and thus the voltage of the fuel cell. For every chemical reaction, the reactants and products have an associated activity. For ideal gasses, the activity can be stated in the form of equation 3.7.

$$a_i = \frac{p_i}{p_0} \quad (3.7)$$

Where p represents the partial pressure of the evaluated reactant or product gas. Linking the activity (Eq. 3.7) to the partial pressures is particularly useful for fuel cells since fuel cells can be considered as gas reactors [43]. The activities a_i of the reaction products and reactants alter the change in Gibbs free energy and thus the maximum voltage of the cell. The activity influence of the overall chemical reaction stated in Eq. 3.3 is expressed in the Nernst equation stated in equation 3.8.

$$E_{Nernst} = E_0 - \frac{RT}{2F} \ln \left[\frac{a_{H_2O}}{a_{H_2} a_{O_2}^{0.5}} \right] \quad (3.8)$$

Integrating the activity equations for the products and reactants of the hydrogen-oxygen reaction results in the Nernst equation with the partial pressures included (Eq. 3.9).

$$E_{Nernst} = E_0 - \frac{RT}{2F} \ln \left[\frac{\left(\frac{p_{H_2O}}{p_0} \right)}{\left(\frac{p_{H_2}}{p_0} \right) \left(\frac{p_{O_2}}{p_0} \right)^{0.5}} \right] \quad (3.9)$$

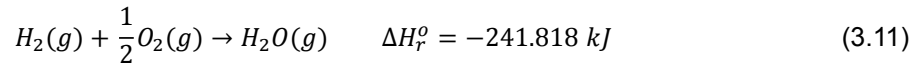
When the pressures are stated in bar, equation 3.9 simplifies to Eq. 3.10 since p_0 equals 1.

$$E_{Nernst} = E_0 - \frac{RT}{2F} \ln \left[\frac{p_{H_2O}}{p_{H_2} p_{O_2}^{0.5}} \right] \quad (3.10)$$

Where the maximum voltage E_0 is earlier stated in equation 3.6, the universal gas constant is represented by R , the operating temperature T is in Kelvin and the Faraday constant is F . The stoichiometrics of the chemical reaction can be recognised from the partial pressures powers. The Nernst equation determines the electromagnetic force (EMF) in terms of product and/or reactant activity at a given temperature and pressure [43].

When a chemical reaction takes place, energy will be released or absorbed, which indicates if the reaction is exothermic or endothermic. The amount of energy is dependent on the conditions under

which the reaction takes place. When the reaction is carried out at standard conditions, the superscript $^{\circ}$ is used, these conditions correspond to: pure components, 1 atm and 25°C. This energy/heat release is stated as the standard heat of reaction ΔH_r° [83]. Now again, evaluating the overall chemical reaction (Eq. 3.3), stated with the standard heat of reaction gives equation 3.11.



The enthalpy change of the overall reaction ΔH_r° is negative, the chemical reaction is therefore exothermic and the heat of reaction $-\Delta H_r^{\circ}$ is thus positive. It is usually more convenient in process design calculations to express the heat of reaction on a basis of moles of product produced. The standard heat of reaction is thus stated as kJ/mol of produced steam. Appendix A.1 gives an in depth formulation and calculation method of the enthalpy and entropy of the chemical reaction to determine the Gibbs Free Energy of the fuel cell.

Reaction kinetics

A solid oxide fuel cell can be modelled as a chemical plug flow reactor but with more complicated reaction kinetics compared to a regular reactor. The greatest difference is that the reaction rate term is more comprehensive than the usual kinetic reactions used in plug flow reactors. The fuel cell current is in proportional relation to the reaction rate, the rate of species (R_i) generated or consumed in the fuel cell are defined as.

$$R_{H_2} = -\frac{I_{cell}}{2F}, \quad R_{H_2O} = \frac{I_{cell}}{2F}, \quad R_{O_2} = -\frac{I_{cell}}{4F}$$

With the total current leaving the cell, stated as I_{cell} . The current is often defined per unit of area of the cell so that a comparison between cells of different sizes can be made, this results in the current density: $i = I_{cell}/A_{cell}$. For clarification purposes, two perspectives of the fuel cell voltages and currents are introduced and depicted in figure 3.7. The cell perspective E_{cell} stated in equation 3.12, where the cell voltage equals the Nernst voltage E_{Nernst} minus the total voltage losses E_{loss} . Continuing with the load perspective E_{load} stated in equation 3.13, where the voltage equals the load current I_{load} times the load resistance R_{load} in the case of a purely resistive load. Once the cell is connected to the load, the cell current needs to be equal to the load current and the cell voltage needs to be equal to the load voltage, meaning that equations 3.14 and 3.15 must be satisfied.

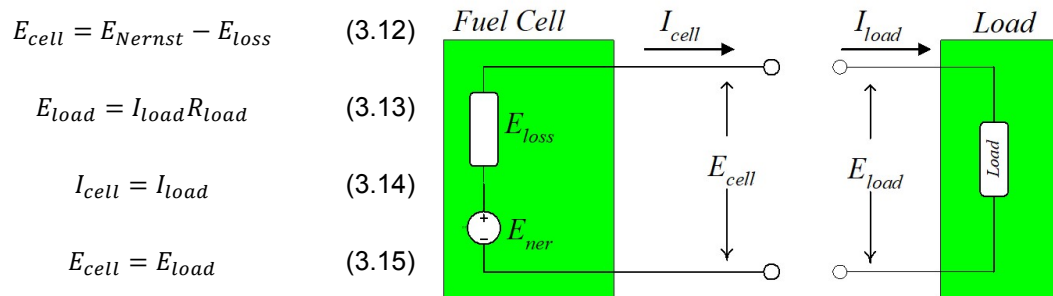


Figure 3.7: Schematic electric circuit of a fuel cell / load system

The voltage loss E_{loss} stated in equation 3.12 and depicted in figure 3.7 mainly consists of the following irreversibilities taking place in the fuel cell. Fuel crossover and internal currents will not be elaborated in detail due to the fact that their contribution to the combined losses is usually not of great importance for high-temperature cells in terms of operating efficiency [43].

1. Activation losses
2. Ohmic losses
3. Concentration losses
4. Fuel crossover and internal currents

1. Activation losses

The activation losses are caused by the speed of the reactions taking place on the surface of the electrodes and can be derived from the Butler-Volmer equation. A percentage of the generated voltage is wasted due to the fact that a part of the generated voltage is required to drive the chemical reaction that transfers the electrons to and from the electrodes [43]. Activation losses become more important in low- and intermediate-temperature fuel cells, the amount of voltage drop is defined via equation 3.16, where A and b are constants that depend on the type of cell and its conditions and the electrode material, with $i > b$ and i is the current density in Acm^{-2} .

$$\Delta E_{act} = A \ln \left(\frac{i}{b} \right) \quad (3.16)$$

2. Ohmic losses

The ohmic losses are is due to the electrical resistance of the electrodes and resistance of the flow of ions in the electrolyte. The voltage drop is directly proportional to the current and stated in equation 3.17.

$$E = IR \quad (3.17)$$

The ohmic voltage loss is thus an increasing function of current and in most fuel cells mainly caused by the electrolyte, yet the interconnects or bipolar plates can also be of importance [43]. When the ohmic losses are expressed in terms of current density, the quantity area-specific-resistance (ASR) is defined. The ASR corresponds to the resistance of 1 cm^2 , the equation of the ohmic voltage drop then becomes equation 3.18, where i is the current density in Acm^{-2} and the ASR in Ωcm^2 .

$$\Delta E_{ohm} = iASR \quad (3.18)$$

3. Mass transport or concentration losses

The mass transport or concentration losses of a fuel cell are due to a decline in concentration of the reactants. For instance, when the anode of a fuel cell is supplied with hydrogen, there will be a small pressure drop due to the fact that the hydrogen is consumed as a result of a current drawn from the cell. "This reduction in pressure results from the fact that there will be a flow of hydrogen down the supply ducts and tubes and this flow will result in a pressure drop due the their fluid resistance. This pressure reduction will depend on the electric current from the cell (and hence H_2 consumption) and the physical characteristics of hydrogen supply system" (J. Larminie, 2003, p.57) [43]. The same holds for the reaction at the cathode side of the fuel cell resulting in a pressure drop of the supplied oxygen. In short: the reduction of the supplied fuel and oxidiser pressures result in a reduction in voltage. There is however no analytical expression developed for this phenomena, an empirical equation developed by Kim et al., and Laurencelle et al. [44] is most widely used and describes the voltage transport losses with two constants, the mass transport coefficient m and the growth rate n , which must be chosen accurately depending on fuel cell type and operation parameters [43]. The growth rate n is frequently fitted iterative to experimental data, where the mass transport coefficient decreases linearly with temperature [44].

$$\Delta E_{trans} = me^{ni} \quad (3.19)$$

Combining the irreversibilities

Now that the major losses that make up E_{loss} are defined, equation 3.12 can be stated more extensive and is done so in equation 3.20, where E_{loss} is the summation of the activation, ohmic and transport losses.

$$E_{cell} = E_{Nernst} - (\Delta E_{act} + \Delta E_{ohm} + \Delta E_{trans}) \quad (3.20)$$

Figure 3.8 shows the typical behaviour of decreasing cell voltage with increasing current density due to the three major losses, plotted together with the theoretical or ideal voltage. For solid oxide fuel cells operating at high temperatures 800-1000 °C, the losses in the cell components are governed mainly by ohmic losses [43]. This behaviour is depicted in figure 3.9 where the linear decrease in cell

voltage is only due to ohmic resistances, plotted with the maximum power of the cell. Since the fuel cell power equals the voltage times the current (Eq. 3.5) or current density (i), the optimum region of operating can be found, this is depicted in figure 3.9 by the grey area. At low current density, the power is low because the current density is low. At high current density, the power is low since the voltage is low and the losses are high.

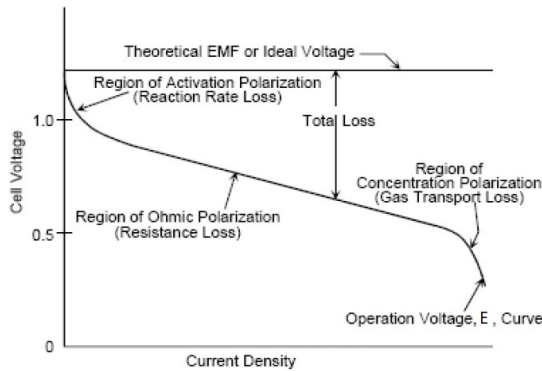


Figure 3.8: Schematic relation between the current density versus cell voltage of a standard SOFC with the specific loss regions [11]

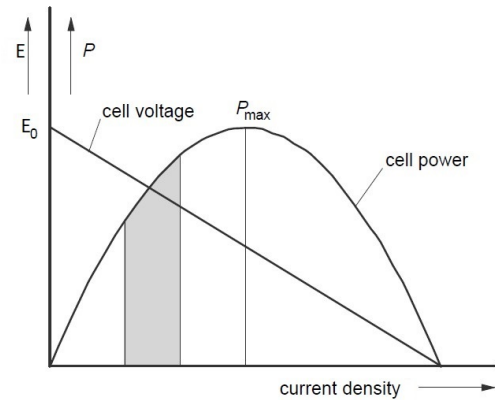


Figure 3.9: Schematic current density versus cell voltage together with the optimum power of the FC [11]

3.4. Advantages of integrating a SOFC into a power cycle

As elaborated in chapter 2.4, most advanced electric power plants built today use a combined heat and power cycle to produce electricity with maximum efficiencies of approximately 62% LHV [32]. Electrical efficiencies of state-of-the-art solid oxide fuel cells fabricated today exceed those of conventional power cycles with electrical efficiencies of 65% [9]. Which, theoretically, indicates that 35% of the LHV energy of the converted fuel is transformed into heat. As stated in chapter 2.3, the most significant losses or irreversibilities occurring in power cycles are related to the heat addition to the cycle. An integrated SOFC-GT system exploits the complementary features of the two power systems, where the gas turbine recuperates the thermal energy from the SOFC exhaust and thereby increasing the overall system efficiency [84]. Theoretically, in a perfectly integrated combined power system, the efficiency of a SOFC combined cycle with the technology available today can simply be calculated as $65 + (35 - 62) / 100 = 86.7\%$, which is more than a 20% increase compared to state of the art combined cycle power plants today [32]. This however is not feasible due to the differences in optimal fuel cell operating conditions and the optimal combined cycle operating conditions regarding temperature and pressure regions. A combination of the two is still extremely promising since the integration of a SOFC in a combined cycle can still lead to theoretical efficiencies of 70-80% [73]. Multiple researches have been conducted about the integration of fuel cells in power cycles, some of them have been built such as the Siemens-Westinghouse cycle [33]. Despite the fact that the first SOFC-GT cycle was proposed more than 30 years ago, the technology has not been widely implemented for actual power generation. Table 3.2 states an overview of notable SOFC-GT cycle researches since the year 2000 in chronological order with their corresponding electrical efficiencies [90]. The stated combined fuel cell cycles are primarily fuelled with natural gas, except for the cycle developed by Schouten [73], which is fuelled with pure hydrogen.

Table 3.2: SOFC-combined cycle studies conducted in the past years in chronological order [90]

Reference	Year	Thermal cycle	Electrical efficiency (LHV)
Siemens-Westinghouse [49]	2000	Pr. GT	67.3 %
Calise et al. [18]	2006	Pr. GT	60 %
Roberts et al. [67]	2006	Amb. GT	66 %
Rokni [68]	2010	RC	67 %
Gandiglio et al. [29]	2013	RC / Pr. GT + RC	64.6 / 71.9 %
Park et al. [62]	2014	Amb. GT / RE	58.6 / 59.5 %
Campanari et al. [19]	2016	RC / Pr. GT	75.2 / 78.7 %
Whiston et al. [94]	2017	Pr. GT	52.9 %
Schouten [73]	2020	Pr. GT + RC	74-85 %

The thermal cycle abbreviations represent: Pressurised SOFC-Gas Turbine (Pr. GT), ambient pressure SOFC-Gas Turbine (Amb. GT), SOFC-Rankine Cycle (RC) and SOFC-Reciprocating Engine (RE). An example of an integrated SOFC-GT cycle is depicted in figure 3.10 where the fuel cell is placed upstream of the combustor and downstream of the compressor. The burner in this image can be considered as a conventional afterburner since the majority of the hydrogen and oxygen is reacted in the fuel cell, resulting in fewer exergy losses contributed by combustion.

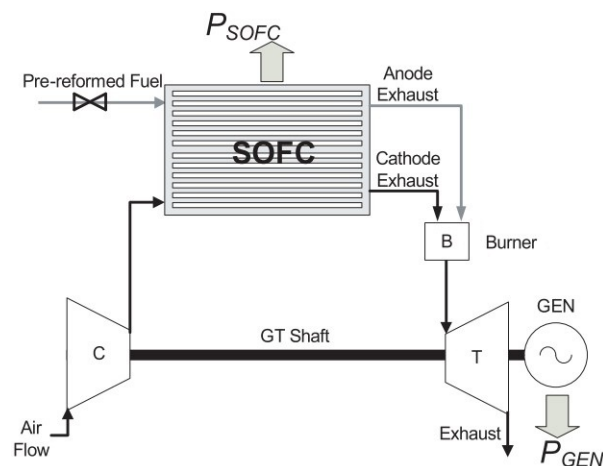
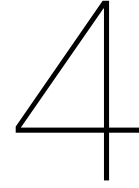


Figure 3.10: Schematic example of a hybrid SOFC-GT configuration [84]



Power cycle equipment

This chapter contains the required literature for the preliminary design of the power cycle components so that, in the end, a first indication regarding the volume and scale of the cycle can be made. This preliminary design will contain basic design criteria for the compressor, turbines and heat exchangers.

4.1. Compressor & turbine selection

The performance of turbomachinery can be described with the operating temperature, pressure, mass flow and rotational speed of the device. These parameters however, are dependent on the physical properties of the working fluid at varying temperature and pressure levels. Any attempt to allow for full variations of all these quantities over the working range of the turbomachinery would involve excessive computations and a concise presentation of the results impossible [23]. Dimensional analysis is used to combine the variables and work with a more manageable amount of numbers. The solution of the problem can then be formulated as a function of all the variables equal to zero and is stated in equation 4.1. The dimensions of temperature are combined with the universal gas constant R , so that the combined variable RT has the dimensions L^2T^{-2} , which is equal to velocity squared. It is customary to not include the viscosity as variable since it would ultimately result in the emergence of the Reynolds number. It is found from experience that the influence of this group is negligibly small over the normal turbomachinery operating range [23].

$$f(D, N, m, p_{01}, p_{02}, RT_{01}, RT_{02}) = 0 \quad (4.1)$$

Where D is a length scale, usually taken as the impeller tip diameter and N is the rotational speed. The 7 variables are now expressed in 3 fundamental units: mass M , length L and time T . By the principle of the Buckingham Pi theorem, this will result in $7-3=4$ non-dimensional groups. In theory, it is possible to obtain an infinite variety of self-consistent sets of these groups, the four frequently used groups stated below are the pressure ratio, efficiency, mass flow parameter group and the shaft speed parameter group respectively [23][91].

$$\frac{p_{02}}{p_{01}}, \quad \eta, \quad \frac{m\sqrt{RT_{01}}}{D^2 p_{01}}, \quad \frac{ND}{\sqrt{RT_{01}}}$$

Other, more practical non dimensionless numbers generated from the same dimensional analysis include the flow coefficient ϕ , load coefficient Ψ , power coefficient \bar{P} and Mach nr Ma stated below.

$$\phi = \frac{Q}{UD^2}, \quad \Psi = \frac{\Delta p_0}{\rho_0 U^2}, \quad \bar{P} = \frac{P}{\rho U^3 D^2}, \quad Ma = \frac{U}{c}$$

Where Q is the volumetric flow rate in m^3/s , U the velocity in m/s and c the speed of sound in the corresponding medium. The flow number ϕ provides a comparison of the output velocity with the reference velocity, the load coefficient Ψ relates the change in pressure to the available dynamic pressure. The Mach nr. Ma takes into account the importance of compressibility effects and the power coefficient \bar{P} is a dimensionless form of power the output.

The preliminary design of the compressor and turbines in this research is based on the data and methodology developed by Baljé, which determines the best suited turbomachinery using two other examples of non dimensional parameter groups, the specific speed (N_s) and specific diameter (D_s) [79]. The specific speed is a characteristic coefficient which allows the comparison between sizes in impellers and pumps when the operating conditions are unequal. It can classify the optimum impeller design and the corresponding characteristic curves. Just as the specific speed, the specific diameter is developed as a non-dimensional scaling parameter for the comparison of the turbomachinery performance. With these two dimensionless parameters and the corresponding Baljé diagrams the type of compressor and turbine are selected. The correlations presented in these diagrams are based on numerous test data, state of the art knowledge and loss correlations. The specific speed is defined as Eq. 4.2 [69] [79].

$$N_s = \frac{\left(\frac{\dot{m}}{\rho_{av}}\right)^{0.5} \Omega}{\Delta h_s^{0.75}} \tag{4.2}$$

Where N_s is dependent on the mass flow \dot{m} in kg/s , the averaged density of the working fluid ρ_{av} in kg/m^3 , the shaft speed Ω in rad/s and the enthalpy rise over the compressor or turbine Δh_s in J/kg . The specific diameter is stated in equation 7.1, where the impeller tip diameter d_t is given in m according to [69] [79].

$$D_s = \frac{d_t \Delta h_s^{0.25}}{\left(\frac{\dot{m}}{\rho_{av}}\right)^{0.5}} \tag{4.3}$$

Turbomachinery used in power cycles can generally be of two different types, axial or centrifugal/radial. Centrifugal compressors are mainly used for low mass flow applications with a good efficiency range of $0.4 < N_s < 1.8$, with optimum efficiency values for $0.6 < N_s < 0.8$. Axial compressors are better suited for high mass flow applications and have higher specific speed values ranging from 1.5 to 20 [79]. Maximum radial turbine efficiency is realised for a specific speed of $0.5 < N_s < 0.6$, maximum axial turbine efficiency has a wider operating range of $0.5 < N_s < 0.9$, for efficiencies exceeding 90% [79]. The single stage compressor and expander Baljé diagrams depicted in figure 4.1 and 4.2 display the relation between the optimum efficiency of the equipment related to the specific speed and specific diameter. The characteristics of constant efficiency are depicted by the solid curves, the dashed curves represent lines of constant head coefficients. The head coefficient is yet another dimensionless parameter which relates the head produced by a single impeller to the square of the impeller tip speed [69].

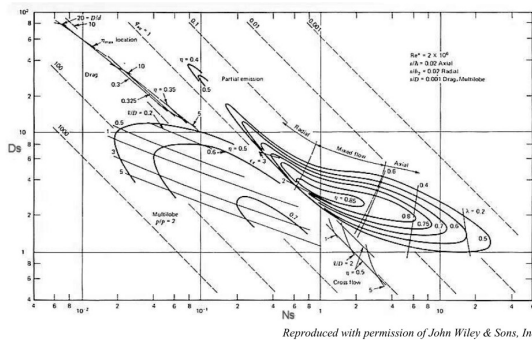


Figure 4.1: The Baljé diagram for single stage compressors [69][79]

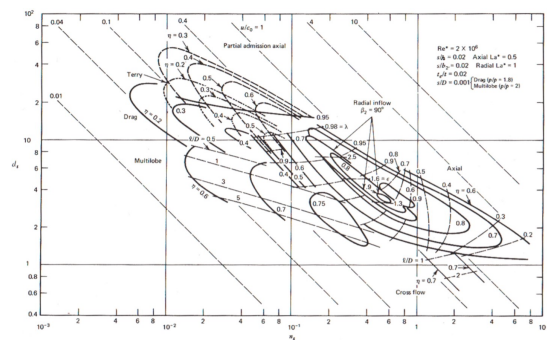


Figure 4.2: The Baljé diagram for single stage expanders [46][79]

In chapter 7, the compressor and expander Baljé diagrams are also presented but larger to see the graphs in more detail. Figures 4.4 and 4.3 state the general differences in operating conditions for axial and radial flow turbomachinery, where +++ is rated as excellent, ++ as good and + as moderate.

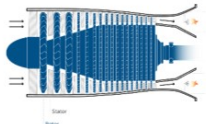
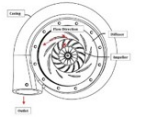
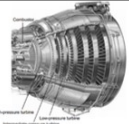
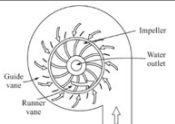
Compressor specifics	Axial flow	Radial flow	Turbine specifics	Axial flow	Radial flow
					
Pressure ratio per stage	Low	High	Pressure ratio per stage	Low	High
Overall pressure ratio	+++	+	Overall pressure ratio	+++	+
Maximum pressure ratio	High	Low	Maximum pressure ratio	High	Low
Airflow	High	Low	Airflow	High	Low
Size	+	+++	Size	+	+++
Simplicity	+	+++	Simplicity	+	+++
Investment costs	+	+++	Investment costs	+	+++
Efficiency range	High PR	Low PR	Efficiency range	>5 MW	<5 MW

Figure 4.3: General axial and radial compressor operating characteristics

Figure 4.4: General axial and radial turbine operating characteristics

4.2. Preliminary turbomachinery design steps

Based on the differences in operating conditions presented in figure 4.3 and 4.4, a choice between the type of turbomachinery will be made. Determining factors between the axial and radial configuration are the maximum pressure ratio per stage and the amount of airflow through the turbomachinery. When the type of machinery is selected, the Baljé diagram is used to determine the best specific speed and diameter according to the high efficiency ranges in the figures. The preliminary design procedure can be summarised in the following five steps, chapter 7.1 will discuss these steps in more detail.

1. Select the type of turbomachinery based on maximum pressure ratio and mass flow
2. Determine the range of optimum N_s with Baljé diagram
3. From N_s range, determine number of stages and corresponding shaft speed
4. Determine range of optimum D_s with Baljé diagram corresponding to the selected N_s range
5. From range of D_s , calculate impeller tip diameter d_t

4.3. Heat Recovery Steam Generator

A heat recovery steam generator (HRSG) is an assembly of heat exchangers that recovers the heat from a hot gas stream, usually coming from a turbine exhaust. It is most widely used for cogeneration and combined cycle power plants, where it transfers the waste heat from the top cycle to the bottom cycle, briefly discussed in chapter 2.4. HRSGs are important components for industrial waste heat recovery, the performance of the steam cycle and thus the performance of the overall combined cycle are directly affected by the design of the HRSG. There are three conventional types of HRSGs, single pressure, dual pressure and triple pressure, depending on the amount of pressure regimes and drums in the boiler.

The important design parameters are the pinch point, approach point, and gas side pressure drop, which are directly related to the heat exchange effectiveness [7]. The pinch point T_{pp} is defined as the difference between the flue gas temperature exiting the evaporator (T_{g3} in figure 4.6) and the water saturation temperature at the drum operating pressure T_{sat} . The definition is stated in equation 4.4, where the subscripts correspond to the design points in figure 4.6.

$$T_{pp} = T_{g3} - T_{sat} \quad (4.4)$$

Commonly adopted pinch points are dependent on the equipment but are generally in the range of 5-15°C for optimal combined cycle efficiencies. The approach point T_{ap} is defined as the difference in water saturation temperature and the temperature of the water entering the evaporator at the corresponding drum operating pressure (T_{w2}) stated in Eq. 4.5 [81].

$$T_{ap} = T_{sat} - T_{w2} \quad (4.5)$$

Minimum approach temperatures of 5 to 8°C avoid flashing of feed water and two phase flow problems such as erosion and hydraulic shock [81]. The pinch-and approach point are depicted in the schematic single pressure HRSG TQ-diagram in figure 4.6, where the flue gas temperature decreases (from left to right) and the water/steam temperature increases (right to left).

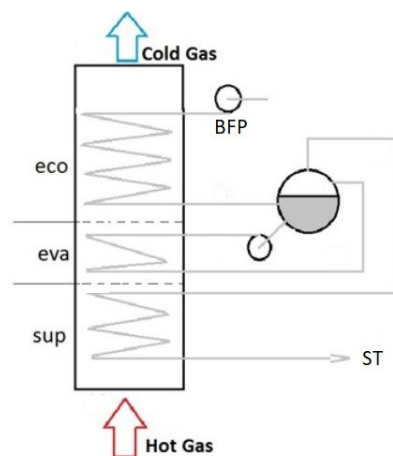


Figure 4.5: Schematic diagram of a single pressure HRSG [57]

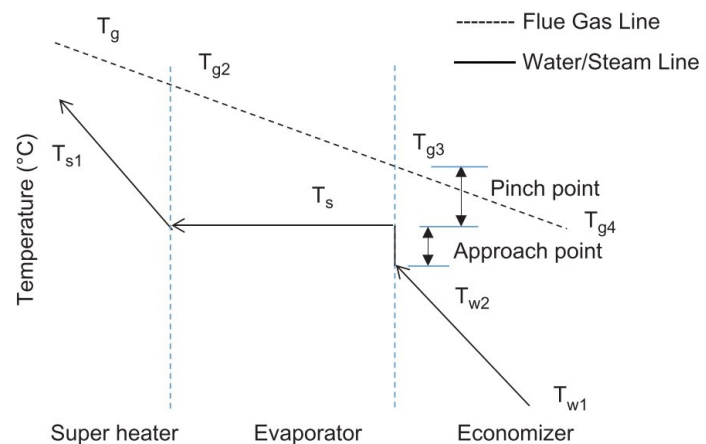


Figure 4.6: Schematic TQ-diagram of a single pressure HRSG with its approach and pinch points [4]

4.3.1. Single pressure HRSG

Hot flue gasses enter the HRSG with high temperatures and transfer heat to the water/steam in three components to eventually leave the HRSG. The standard, single pressure HRSG consists of an economizer, evaporator and superheater shown in figure 4.5. The cold water is pumped into the HRSG via the boiler feedwater pump (BFP) and enters the economiser. The economiser is a heat exchanger that preheats the water to its saturation temperature at the corresponding pressure. After the economiser, the heated water enters the evaporator and is converted into steam via the heat transferred from the flue gas, exiting the evaporator with a vapour fraction of 1. After the evaporator, the steam enters the

superheater, in which saturated or wet steam is converted into superheated or dry steam up to temperatures reaching 600°C [58]. The energy balances for the economiser, evaporator and superheater can be stated as equation 4.6, 4.7 and 4.8 respectively.

Economiser:

$$\dot{m}_{fg} C_{p,fg} (T_{fg,i} - T_{fg,o}) = \dot{m}_w (h_{w,o} - h_{w,i}) \tag{4.6}$$

Evaporator:

$$\dot{m}_{fg} C_{p,fg} (T_{fg,i} - T_{fg,o}) = \dot{m}_w (h_{s,o} - h_{w,i}) \tag{4.7}$$

Superheater:

$$\dot{m}_{fg} C_{p,fg} (T_{fg,i} - T_{fg,o}) = \dot{m}_s (h_{s,o} - h_{s,i}) \tag{4.8}$$

With subscripts fg, o, i, w and s representing flue gas, outlet, inlet, water and steam respectively.

4.3.2. Multiple pressure HRSG

Single pressure heat recovery steam generators make use of a single steam drum operating at a constant drum operating pressure (DOP), multi pressure HRSGs employ two or three steam drums. As such, a dual pressure HRSG consists of two pressure sections, the triple pressure HRSG of three sections. A dual pressure HRSG consists of a low pressure (LP) and high pressure (HP) section, the triple pressure consists of a LP, intermediate pressure (IP) and HP section where each pressure regime has its steam drum and evaporator. In general, more pressure regimes results in higher efficiencies but also higher costs and complexity. The dual pressure HRSG is therefore often used due to its increased efficiency compared to the single pressure variant and lower investment cost and complexity compared to the triple pressure type [4]. Figure 4.7 shows a schematic diagram of a dual pressure HRSG, where figure 4.8 depicts the corresponding schematic temperature-enthalpy diagram [7] with its corresponding design points. Since the dual pressure HRSG has two evaporators, it also has two pinch points and two approach points.

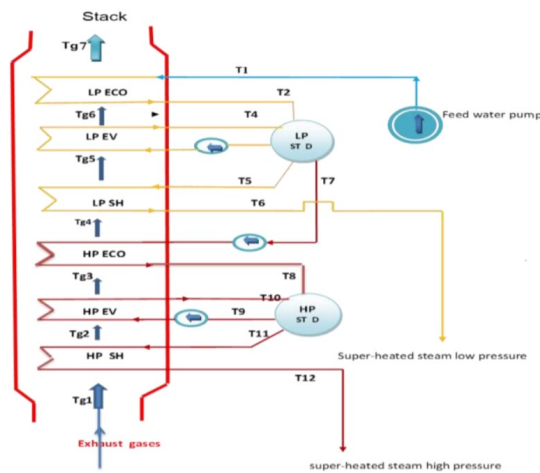


Figure 4.7: Schematic diagram of a dual pressure HRSG [7]

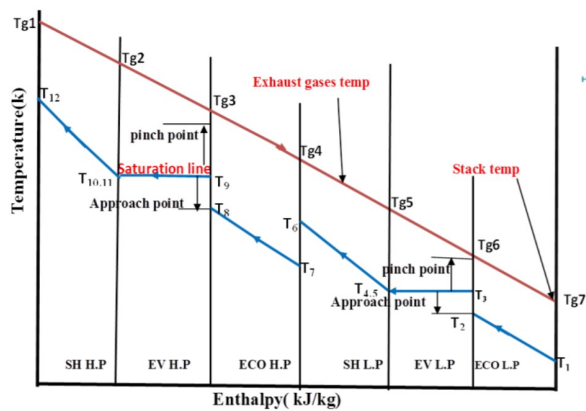


Figure 4.8: Temperature-Enthalpy diagram of a dual pressure HRSG [7]

4.4. Heat exchange equipment

This section covers the different kinds of heat exchange equipment available for the heat transfer within the cycle. Different configurations regarding their best suitable applications are discussed and compared with each other to find the best solution for each process.

Shell & tube heat exchanger

The most common type of heat exchanger (HEX) used in process industries is by far the shell & tube type heat exchanger [76][83]. The advantages of this type are that the mechanical layout gives opportunity for large pressure and temperature ranges, relatively simple fabrication methods, flexibility in material use and its possibility to clean [83]. The shell and tube exchanger is able to operate at pressures reaching 200 bar and has a temperature range of approximately -200 to 750°C. The disadvantages of the shell & tube HEX are however the minimum temperature difference of 10°C between the hot and cold streams and the low area density, which is the heat transfer area per unit of volume in m^2/m^3 [76]. A schematic diagram of a shell and tube heat exchanger is shown in figure 4.9

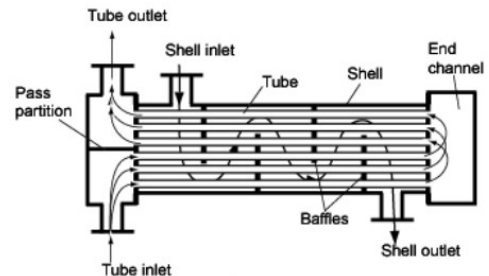


Figure 4.9: Schematic shell & tube heat exchanger diagram

Gasket plate & frame heat exchanger

The next most commonly used in industry is the gasket plate and frame heat exchanger, which is significantly cheaper compared to its shell & tube variant. It consists of a series of parallel plates separated by gaskets to provide a fluid seal. The plates are held together and compressed in a frame using lateral bolts. The use of corrugated plates ensures turbulent fluid flow between the plates and creates mechanical stability to the overall design of the exchanger. The turbulence results in a significant increase of the heat transfer coefficient and reduces fouling between the plates. Due to the possibility of pure counter current flow, the minimum temperature difference between the hot and the cold streams can be reduced to 1°C [36]. The limitations of this design however come with the gaskets, the seals are restricted to operating conditions between -40 and 200°C and pressures not preceding 20 to 28 bar. A variant of the gasket plate heat exchanger is the semi welded plate and frame heat exchanger, which can cope with higher pressures reaching approximately 30 to 32 bar. Semi-welded plate exchangers are used when the gaskets cannot cope with one of the process medias, for example refrigerants. A schematic exploded view of a gasket plate heat exchanger is depicted in figure 4.10.

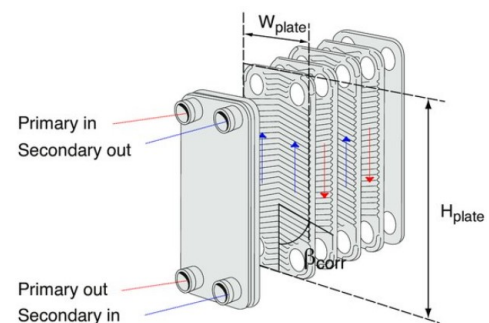


Figure 4.10: Schematic exploded view of a plate & frame heat exchanger

Plate & shell heat exchanger

The shell and plate heat exchanger combines the best features of the shell and tube exchanger and plate exchanger, resulting in the fact that it can cope with the more extreme operating conditions of the shell and tube, while having the high area density of the plate heat exchangers. This combination results in a light weight, compact and efficient heat exchanger that can withstand severe operating conditions. The plates are not separated by gaskets but are welded together which makes it suitable for heat exchange between more corrosive fluids. It is made up out of round plates inside a shell as can be seen in figure 4.11.

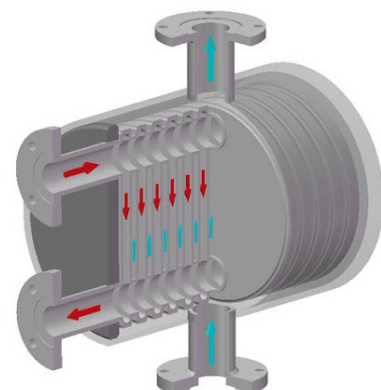


Figure 4.11: Schematic plate & shell heat exchanger

Fully welded plate heat exchanger

The standard welded plate heat exchanger has the same properties as the gasket plate heat exchanger regarding the pure counter flow and allowing the low temperature difference between the hot and cold streams. The elimination of the gaskets broadens the range of application significantly with operating temperatures now possible from -60 to 350°C and pressures reaching 40 to 50 bar. The costs of welded plate heat exchangers are higher compared to the gasket variant but are lower compared to shell and tube exchangers [76]. Welded plate heat exchangers can reach an area density of up to $700\text{ m}^2/\text{m}^3$, making it similar in performance compared to the gasket plate and frame HEX. A modified version of the welded plate and frame exchanger is the Bloc type heat exchanger, which is also fully welded and can cope with more extreme operating temperatures. The maximum pressure is approximately 50 bar and the temperature ranges from -200 to 400°C or in some special cases 700°C [42]. An example of a fully welded plate heat exchanger is depicted in figure 4.12.

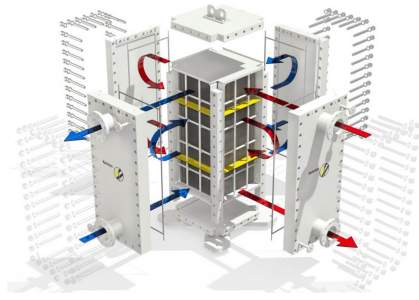


Figure 4.12: Exploded view of a fully welded plate heat exchanger [42]

An overview of the distinctive parameters corresponding to each of the four designs is stated in table 4.1. The abbreviations in the table represent Shell & Tube (S&T), Gasket Plat Heat Exchanger (GPHE), Plate & Shell Heat Exchanger (PSHE) and Welded Plate Heat Exchanger (WPHE).

Table 4.1: Overview of the operating parameters of the four discussed heat exchanger designs

Type	T_{max} $^\circ\text{C}$	P_{max} bar	ΔT_{min} $^\circ\text{C}$	β m^2/m^3
S&T [76][83]	-200-700	200	10	40-500
GPHE [36][83]	-40-200	28	1	100-700
PSHE [77][89]	10-400	40	1	100-700
WPHE [42][76]	-200-700	50	1	100-700

4.4.1. Preliminary design steps

The main purpose of designing a heat exchanger is to determine the area A for the rate of heat transfer Q , also referred to as duty, using the logarithmic temperature difference ΔT_{lm} and the overall heat transfer coefficient U_0 . The general heat transfer equation across a surface is given by Eq. 4.9 [83].

$$Q = U_0 A \Delta T_{lm} \quad (4.9)$$

The design procedures developed for different heat exchange equipment follow the same first few steps. Beyond these first steps, the equipment geometry differs per design and the design procedures starts to deviate from each other. The first design steps of heat exchange equipment are summarised as stated below.

1. Define duty Q
2. Collect physical properties
3. Assume an overall heat transfer coefficient U_0
4. Calculate the logarithmic mean temperature difference ΔT_{lm}
5. Determine the heat transfer area A with the assumed U_0

The assumed overall heat transfer coefficient is in a later design step verified via an iterative method. Chapter 7.3 gives an elaborated explanation of these first design steps including further explanation about the logarithmic mean temperature difference, the complete heat exchange design steps are presented in appendices A.3 and A.4.

5

Thermodynamic design of the basic power cycle

5.1. Starting points

Now that the theoretical foundation has been laid in the previous chapters, this chapter presents the designed power cycle with its thermodynamic features. As stated previously, the designed cycle is an integrated SOFC-Brayton cycle coupled with a bottoming Rankine cycle connected with a heat recovery steam generator. A schematic principle flow scheme of the cycle is depicted in figure 5.1. From power cycle- and fuel cell literature, a few thermodynamic states in the cycle were known in advance, these are depicted in the figure [71][72]. The thermodynamic states in the cycle where the pressure and temperature were still unknown are represented with P or T respectively.

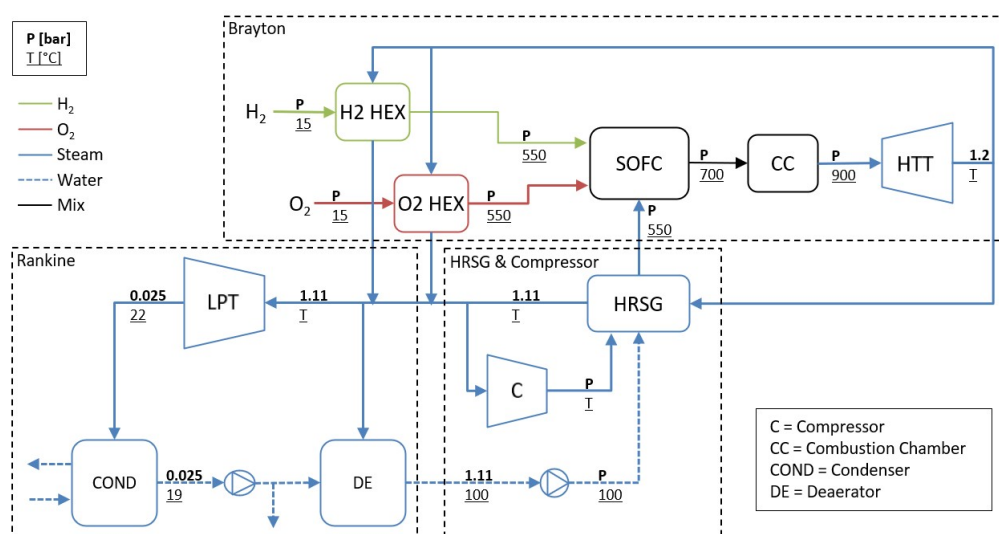


Figure 5.1: Principle flow scheme of the preliminary SOFC integrated combined cycle

The outlet temperature of the combustion chamber is limited to 900°C due turbine material limitations [17][60]. The cooling steam temperature for the solid oxide fuel cell cannot be lower than the required 550°C [73]. Condenser pressures and approximate temperatures in the Rankine part of the cycle are standard vapour power cycle values. An overview of the thermodynamic starting points is stated in table 5.1. Two, yet to be defined, important variables of the cycle have a large influence on the efficiency and power output of the system. The pressure ratio over the HTT and the minimum temperature differences of the sensible gas to gas heat exchangers discussed in the upcoming subchapter.

Table 5.1: Thermodynamic input data from literature

Inputs	Value	Unit
H_2 & O_2 cycle entry temperature	15	°C
Inlet temperature SOFC	550	°C
Maximum temperature difference SOFC	150	°C
Maximum high temperature turbine inlet temperature	900	°C
Low pressure turbine inlet pressure	1.11	bar
Condenser pressure	0.025	bar

5.1.1. Pressure analysis

To determine the optimal operating pressures for the proposed cycle, it must be taken into account that the HTT PR has a large effect on the temperatures, compressor work and eventually steam quality in the bottom cycle. Selecting a high HTT PR results in more power generated by the turbine but has the effect of a lower outlet temperature. Since the inlet and outlet temperatures are approximately known, an initial range of HTT pressure ratio was determined with the equation for isentropic expansion stated in Eq. 5.1, where k is the specific heat ratio C_p/C_v and is considered constant. A HTT pressure ratio between 6 and 8 was determined to be good starting point.

$$\frac{p_{in}}{p_{out}} = \left(\frac{T_{in}}{T_{out}} \right)^{\frac{k}{k-1}} \quad (5.1)$$

The limiting parameters for each simulation are the SOFC cooling steam inlet temperature, H_2 & O_2 preheater outlet temperature and the steam quality at the LPT exit. The next important variable is the minimum temperature difference (ΔT_{min}) of the gas-to-gas heat exchangers within the cycle. The minimum temperature difference in a heat exchanger is highly dependent on the type of exchanger. Shell & Tube heat exchangers require a minimum ΔT_{min} of approximately 10°C, where plate heat exchangers can transfer heat efficiently with a ΔT_{min} of 1°C. To determine the best minimum temperature difference in the gas-to-gas heat exchangers, the ΔT_{min} was varied for each pressure simulation for the values of 2, 5, 10, 15 and 20°C. The optimum ratio between minimum temperature differences in the heat exchangers and the HTT pressure ratios has a significant influence on the maximum generated power by the system. With a larger temperature difference, a lower pressure ratio over the HTT is feasible and thus, less work can be extracted from the medium. The results from the thermodynamic simulations showed that for each ΔT_{min} the SOFC inlet temperature was the limiting factor for the maximum pressure ratio of the HTT. Figure 5.2 shows the results of the simulations where the HTT-PR is plotted against the SOFC cooling steam inlet temperature for each ΔT_{min} (dT in figure).

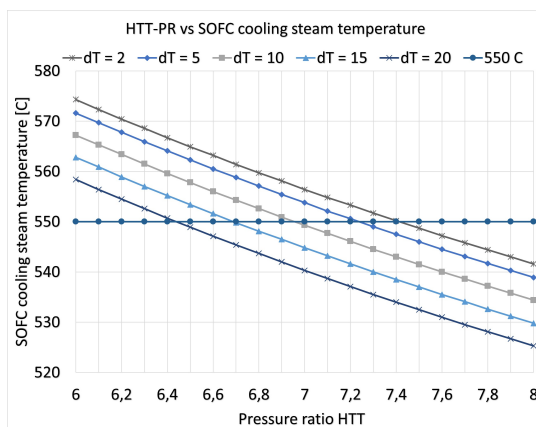


Figure 5.2: HTT-PR vs SOFC cooling steam inlet temperature for each ΔT_{min}

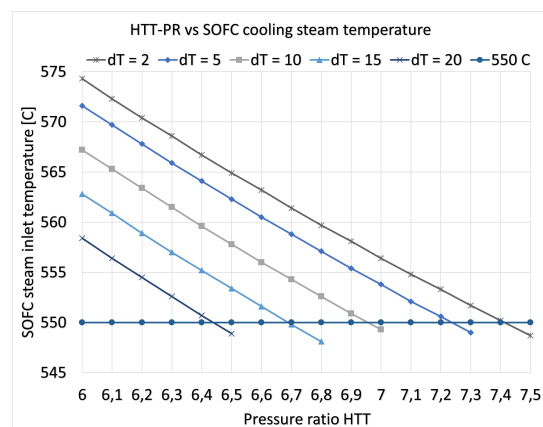


Figure 5.3: HTT-PR vs SOFC cooling steam inlet temperature cutoff for max PR for each ΔT_{min}

From the data can be concluded that the predictions about the relation between the PR and ΔT_{min} proved to be true. Smaller temperature differences in the heat exchangers result in a higher achievable

HTT PR before the SOFC inlet temperature drops below the required temperature of 550°C. For clarity reasons, each ΔT_{min} case was cut off for its maximum HTT-PR before the SOFC inlet temperature became below the 550°C with a 2°C margin, this is depicted in figure 5.3. The figures show that the optimum HTT-PR lies between 6.5 and 7.5 for heat exchanger minimum temperature differences varying between 2 and 20°C. When focusing on the turbines in the cycle, the results are clear. Figure 5.4 and 5.5 show the HTT & LPT power output per ΔT_{min} for the limiting HTT-PR displayed in figure 5.3. A low ΔT_{min} heat exchanger setting results in a higher HTT power output, due to the larger achievable PR but a lower power output from the LPT. A high ΔT_{min} results in the opposite, namely a lower HTT power output but a higher LPT power output. The differences in power output scale however are significant and it is therefore justified to focus on the HTT power output when selecting the best HTT pressure ratio and ΔT_{min} .

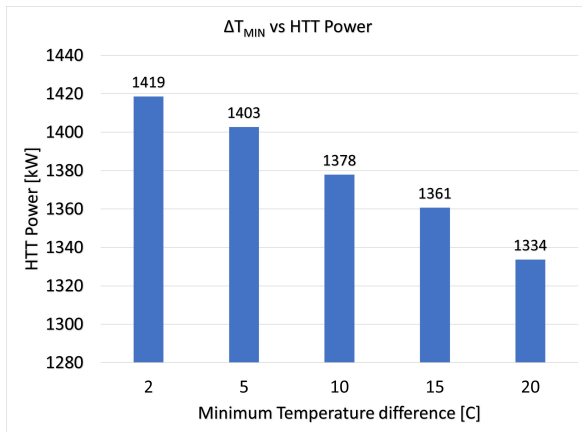


Figure 5.4: Heat exchangers ΔT_{min} vs HTT power output

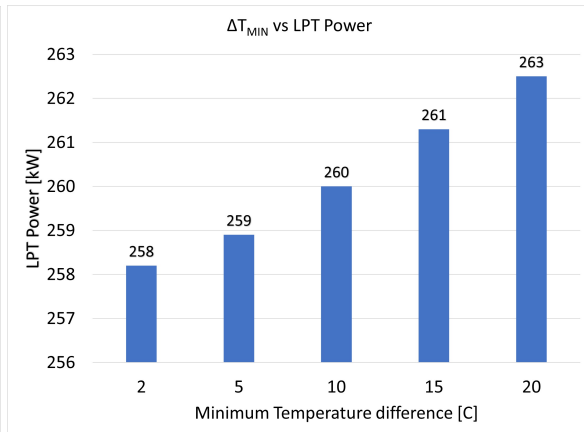


Figure 5.5: Heat exchangers ΔT_{min} vs LPT power output

When focusing on the gross power output of the combined cycle, higher HTT pressure ratios are the favourable option due to the fact that with a high PR, more energy is extracted from the medium and converted into useful power. Figure 5.6 shows the relation between the HTT-PR and gross power output of the combined cycle (excluding SOFC) where each ΔT_{min} case is cutoff for its maximum pressure ratio. Comparing the gross power output to the thermal efficiency of the cycle results in the expected outcome considering how the thermal efficiency of a cycle is defined in chapter 2.3, namely (Power output)/(Energy input). Figure 5.7 depicts the relation between the HTT-PR and thermal efficiency for each ΔT_{min} case cutoff at its maximum pressure ratio.

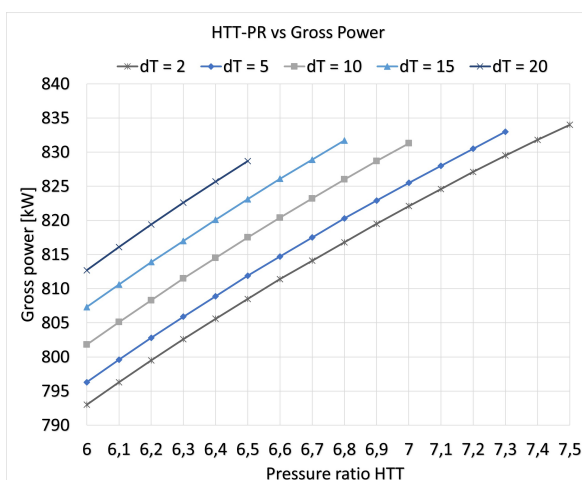


Figure 5.6: HTT-PR vs Gross power output of the combined cycle (excl. SOFC power)

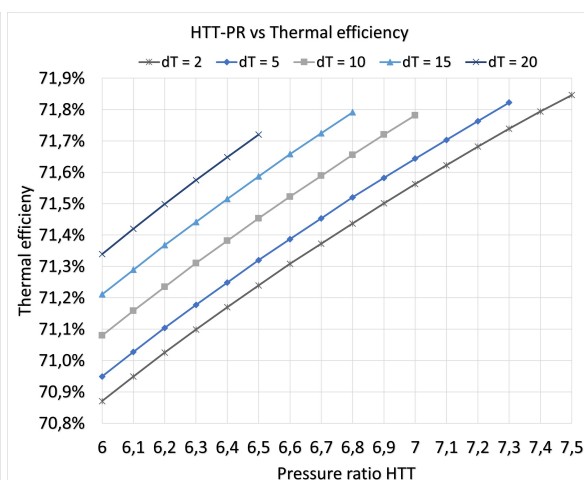


Figure 5.7: HTT-PR vs Thermal efficiency of the combined cycle (incl. SOFC power)

From the results generated by the thermodynamic simulations, the decision was made for a mini-

imum temperature difference of the gas to gas heat exchangers of 15°C. The decision was based on a number of factors that influence the system. The good thermal efficiency, combined with a relatively low pressure ratio of 6.8 is favourable for the turbomachinery equipment within the cycle. A ΔT_{min} of 15°C has the advantage that Shell & Tube heat exchangers can be employed for the heat transfer, as well as welded plate heat exchangers. Small ΔT_{min} values result in large heat transfer equipment, which is not desired in a basic cycle design, furthermore, a value of 15°C is a common value in combined cycle literature and is proven to operate properly [71][72].

5.1.2. Starting points of the cycle

Now that the minimum temperature difference of the gas to gas heat exchangers and pressure ratio of the high temperature turbine are selected, the defined starting points and key parameters of the cycle are presented in table 5.2. Component efficiencies, losses and supplied hydrogen and oxygen conditions are common and standard values presented in literature [72][71]. With the values presented in table 5.2, a definitive thermodynamic simulation of the cycle was made. For the thermodynamic simulations, the modelling software Thermoflex was used.

Table 5.2: Component efficiencies and key parameters of the proposed cycle thermodynamic simulation

Key parameters	Value
Fuel	Pure hydrogen
Oxidiser	Pure oxygen
Hydrogen LHV	120.07 MJ/kg
Hydrogen HHV	141.89 MJ/kg
Chemical exergy hydrogen	117.11 MJ/kg
Chemical exergy oxygen	124.06 kJ/kg
Chemical exergy water	49.96 kJ/kg
Oxygen purity	100%
Oxygen excess	0%
Reactants supplied pressurised	Yes
Steam property formulation	IAPWS-IF-97
Ambient conditions	15°C, 1.01324 bar
Supply temperature reactants	15°C
Fuel cell pressure loss	2%
Fuel cell heat loss	2%
Combustor pressure loss dP/P	4.25
Combustor heat loss dQ/Q	0.25% of fuel in
Gas turbine inlet temperature	900°C
Gas turbine inlet pressure	8.19 bar
Turbine isentropic efficiency	HTT: 87.37%, LPT: 82.74%
Maximum turbine metal temperature	900°C
Compressor isentropic efficiency	80%
Steam turbine inlet pressure	1.11 bar
Pump isentropic efficiency	70%
Heat exchange heat loss dQ/Q	0.5%
HRSG pressure loss, cold side	3.15% per heat exchanger
HRSG pressure loss, hot side	2% per heat exchanger
Economiser ΔT_{min}	5°C
Superheater ΔT_{min}	15°C
Condenser pressure	0.025 bar
Condenser subcooling	2°C
Condenser & deaerator pressure loss	0%
HRSG normalised heat loss	0.5%
Mechanical efficiency	99.6%
Generator efficiency	98.5%
Auxiliary losses	0.35% of heat input

5.2. Basic power cycle thermodynamics

This chapter is, just as the proposed cycle, divided into the three main segments, the top cycle, HRSG and bottom cycle. The components making up each segment are discussed individually for their key parameters and operating conditions. A preliminary schematic overview of the basic cycle was stated in figure 5.1, in the end of this chapter, all thermodynamic states within the cycle will be known and presented again in a final flow scheme. The power cycle is designed to be of the order of magnitude of approximately 3 MW, which for instance could be used to propel the newest electrical powered inland shipping vessels. Electrical power is generated via the fuel cell, the high temperature turbine and the low pressure turbines connected to generators. The hydrogen mass flow was scaled according to the total power output of the system, the oxygen mass flow was determined with the $H_2:O_2$ mass ratio from the overall chemical reaction stated (Eq. 3.3) so that the medium downstream of the combustor has a theoretical steam percentage of 100%. A hydrogen mass flow of 0.035 kg/s was determined when taking into account the fuel cell efficiencies and standard Graz cycle efficiency values [9][71]. This hydrogen mass flow results in an oxygen mass flow of 0.28 kg/s.

5.2.1. SOFC integrated Brayton cycle

This subchapter covers the thermodynamic design of the individual components that make up the top cycle. Each part will provide the key parameters and operating conditions of the component and the reasoning why there was chosen for the specific setup.

Solid Oxide Fuel Cell

The performances of the Solid Oxide Fuel Cell were introduced in chapter 3, in the thermodynamic design stage, the fuel cell is considered as a black box in which three incoming flows enter and one exits. It is important that the incoming hydrogen, oxygen and cooling steam have a minimum temperature of 550°C. The mass flow of cooling steam ensures a maximum temperature rise of 150°C, the amount of mass flow is calculated via the energy balance presented in equation 5.2.

$$\dot{m}_{H_2O,cool} = \frac{\Delta Q}{\Delta h} = \frac{(Q_{H_2,out} + Q_{O_2,out} + Q_{H_2O,prod} + P) - (Q_{H_2,in} + Q_{O_2,in})}{h_{H_2O,out} - h_{H_2O,in}} \quad (5.2)$$

Since the LHV efficiency and fuel conversion of the fuel cell are 65% and 80% respectively, the generated power can for now be calculated by equation 5.3 [9][72].

$$P_{SOFC} = \dot{m}_{H_2} LHV_{H_2} \eta_{LHV} \eta_{conv} \quad (5.3)$$

Where η_{LHV} and η_{conv} are the LHV efficiency and fuel utilisation respectively. The percentage of fuel conversion inside the fuel cell has a significant effect on the size of the stack but also on the maximum temperatures downstream in the power cycle. A lower fuel conversion results in a larger fraction of hydrogen mass flow entering the combustor, leading to significantly higher temperatures in the combustion chamber and thus turbine inlet temperature. Since no cooling of the turbine blades is highly desired for a relatively basic design, a maximum fuel conversion in the fuel cell is necessary to keep the TIT approximately 900°C [17][60]. The specific thermodynamic operating parameters of the SOFC regarding the generated electrical power, efficiencies and losses are presented in table 5.3.

Table 5.3: Solid oxide fuel cell thermodynamic operating specifics

Parameters	Value	Unit
Power	2184.4	kW
Pressure drop	2.00	%
Heat loss	2.00	%
Efficiency η_{LHV}	65.00	%
Fuel conversion η_{conv}	80.00	%

High Temperature Turbine

The high temperature turbine in the Brayton part of the proposed cycle, together with the SOFC has the largest impact on the operating conditions of the cycle. Chapter 5.1.1 covered the analysis from which the best HTT pressure ratio was selected with as initial starting point the equation of isentropic expansion. As mentioned in the thermodynamic SOFC section, the turbine inlet temperature, or combustion chamber outlet temperature depends on the fuel conversion of the fuel cell and limited by the maximum temperature of the blade material. State of the art maximum turbine inlet temperatures without active blade cooling are 900°C, which is therefore set to be the inlet temperature of the HTT [17][60]. The thermodynamic operating specifics of the gas turbine are presented in table 5.4.

Table 5.4: Gas Turbine thermodynamic operating specifics

Parameters	Value	Unit
Pressure Ratio	6.80	-
Shaft power	1360.7	kW
Mechanical loss	5.47	kW
Polytropic efficiency $\eta_{\infty t}$	85.00	%
Isentropic efficiency $\eta_{t,s}$	87.37	%

H2-O2 Preheaters

The heat exchangers that ensure the temperature elevation of the incoming hydrogen and oxygen to 550°C are referred to as the H_2 & O_2 preheaters. To bring the reactants up to temperature, these exchangers use a precise fraction of the mass flow of the gas turbine exhaust. The decision for the minimum temperature difference of the heat exchangers is presented in chapter 5.1.1, from that analysis, a ΔT_{min} of 15°C was selected. This minimum pinch indicates that the turbine outlet temperature cannot drop below 565°C to get the reactants up to SOFC operating temperature. Only sensible heat transfer occurs in the exchangers, this indicates that the mass flow coming from the HTT is adjusted accordingly so the steam HEX outlet temperature does not drop below its saturation point. The energy balances of the inlet hydrogen and oxygen preheaters are stated in equation 5.4 and 5.5 respectively. With the energy balances, the necessary steam mass flows \dot{m}_{H_2O} are determined to heat up the incoming product streams.

$$\dot{m}_{H_2} C_{p,H_2} (T_{H_2,o} - T_{H_2,i}) = \dot{m}_{H_2O} C_{p,H_2O} (T_{H_2O,i} - T_{H_2O,o}) \quad (5.4)$$

$$\dot{m}_{O_2} C_{p,O_2} (T_{O_2,o} - T_{O_2,i}) = \dot{m}_{H_2O} C_{p,H_2O} (T_{H_2O,i} - T_{H_2O,o}) \quad (5.5)$$

Where the subscripts i and o represent the inlet and outlet conditions, furthermore, the gasses are treated as ideal gasses, implying constant heat capacity's. The specific thermodynamic parameters of the overall performances of the reactant heat exchangers are stated in table 5.5.

Table 5.5: Reactant hydrogen & oxygen heat exchanger thermodynamic operating specifics

Preheater parameters	H_2	O_2	Unit
Heat transfer	271.7	147.6	kW
Heat loss	1.37	0.74	kW
Reactant pressure drop	0.22	0.22	bar
Steam pressure drop	29.4	29.4	mbar

Combustion chamber

The combustion chamber is arranged downstream of the SOFC and burns the unreacted hydrogen and oxygen in the SOFC outlet stream. Since the SOFC fuel conversion is defined as 80%, the combustor thus burns 20% of the hydrogen and oxygen supplied to the cycle. The medium downstream of the combustor is assumed to consists of 100% steam which indicates that all hydrogen and oxygen are reacted to H_2O . The combustion chamber operation specifics are presented in table 5.6.

Table 5.6: Combustion chamber operating specifics

Parameters	Value	Unit
Normalised heat loss dQ/Q	2.27	kW
Heat loss	2.27	kW
Pressure loss dp/p	0.04	-

Now that all the top cycle components are elaborated, a detailed schematic overview of the top cycle can be presented in figure 5.8, presenting the temperature, pressure and mass flow for each point in the Brayton part of the proposed cycle.

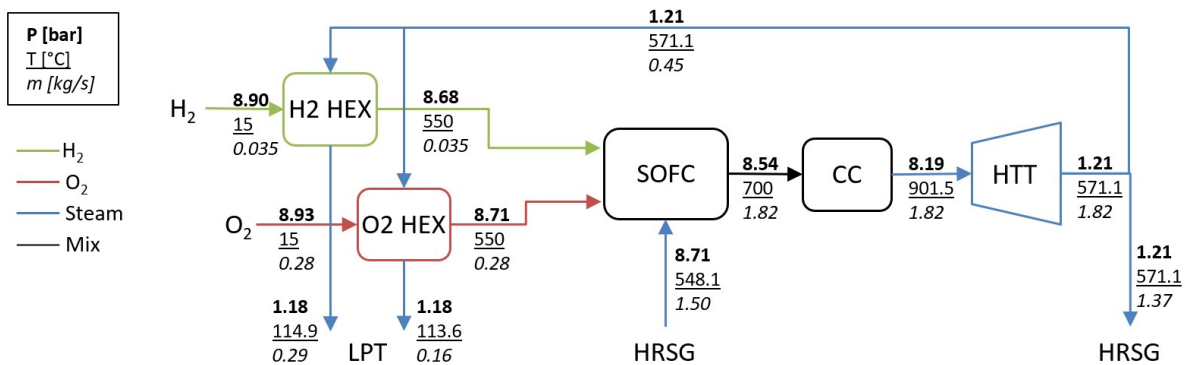


Figure 5.8: Schematic overview of the designed SOFC-Brayton part of the integrated SOFC combined cycle

5.2.2. Single pressure heat recovery steam generator

The basic SOFC integrated combined cycle is equipped with a relatively simple heat recovery steam generator. It is a single pressure HRSG consisting of an economiser, evaporator and two superheaters. For clarity reasons, the hot stream that transfers its heat to the cold stream is referred to the flue gas stream, coming from the HTT, passing through the HRSG and eventually leaving for the LPT. The cold stream that receives the heat from the flue gas stream is referred to as steam, entering the HRSG from the boiler feedwater pump BFP and leaving the HRSG as cooling steam for the SOFC. Up until now, the HRSG was presented in the figures as a black box, figure 5.9 unveils the components of the assemblage that is referred to as the heat recovery steam generator with the corresponding stream pressures, temperatures and mass flow.

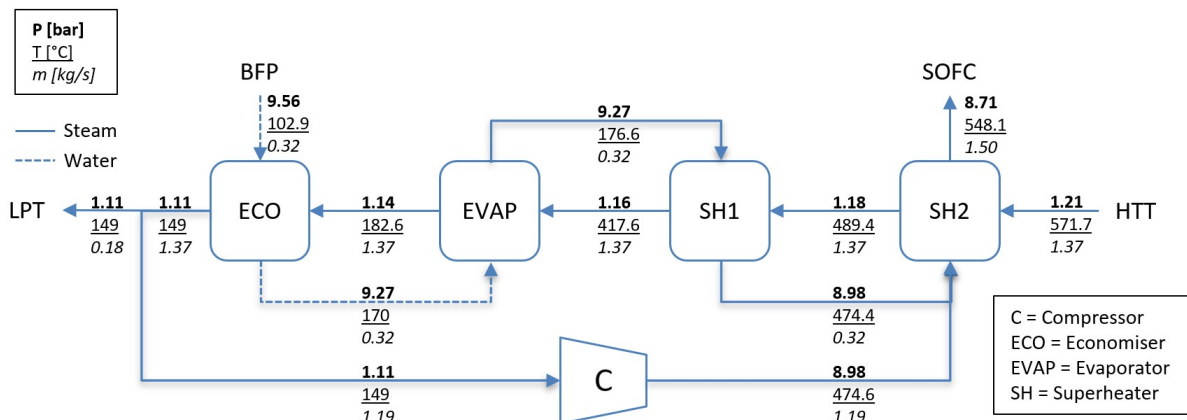


Figure 5.9: Schematic overview of the basic, single pressure heat recovery steam generator and compressor

Important parameters of the HRSG are the steam outlet temperature of 550°C, which will serve as the SOFC cooling steam, together with the pinch- and the approach point of the evaporator. The

pinch point is on the lower side of commonly adapted temperature differences namely 5°C but still within the tolerable range as explained in chapter 4.3. The approach point is 6.6°C, which is enough to prevent two phase flow problems and flashing of the feedwater. The thermodynamic parameters of the components presented in figure 5.9 are stated below in table 5.7 regarding the amount of heat transferred, heat losses and pressure drops. The compressor is discussed separately in the upcoming subchapter 5.2.2.

Table 5.7: Basic HRSG thermodynamic operating specifics

Parameters	ECO	EVAP	SH1	SH2	Unit
Heat transfer	90.7	648.2	205.3	240.6	kW
Heat loss	0.46	3.257	1.03	1.21	kW
Flue gas pressure drop	24.9	20.0	24.9	24.9	mbar
Steam pressure drop	0.29	0	0.28	0.27	bar

The corresponding Temperature-Heat transfer (TQ) diagram of the designed HRSG is presented in figure 5.10. The temperature increase of the steam (blue) and decrease of the flue gas (red) are presented into divided sections corresponding to the discussed components of the HRSG. The sections are stated in the figure together with the heat transferred within the component in kW from the flue gas to the steam. From the TQ diagram becomes especially clear that the major part of heat is transferred in the evaporator at relatively low temperature. Improvements regarding this design will be discussed in more detail later on.

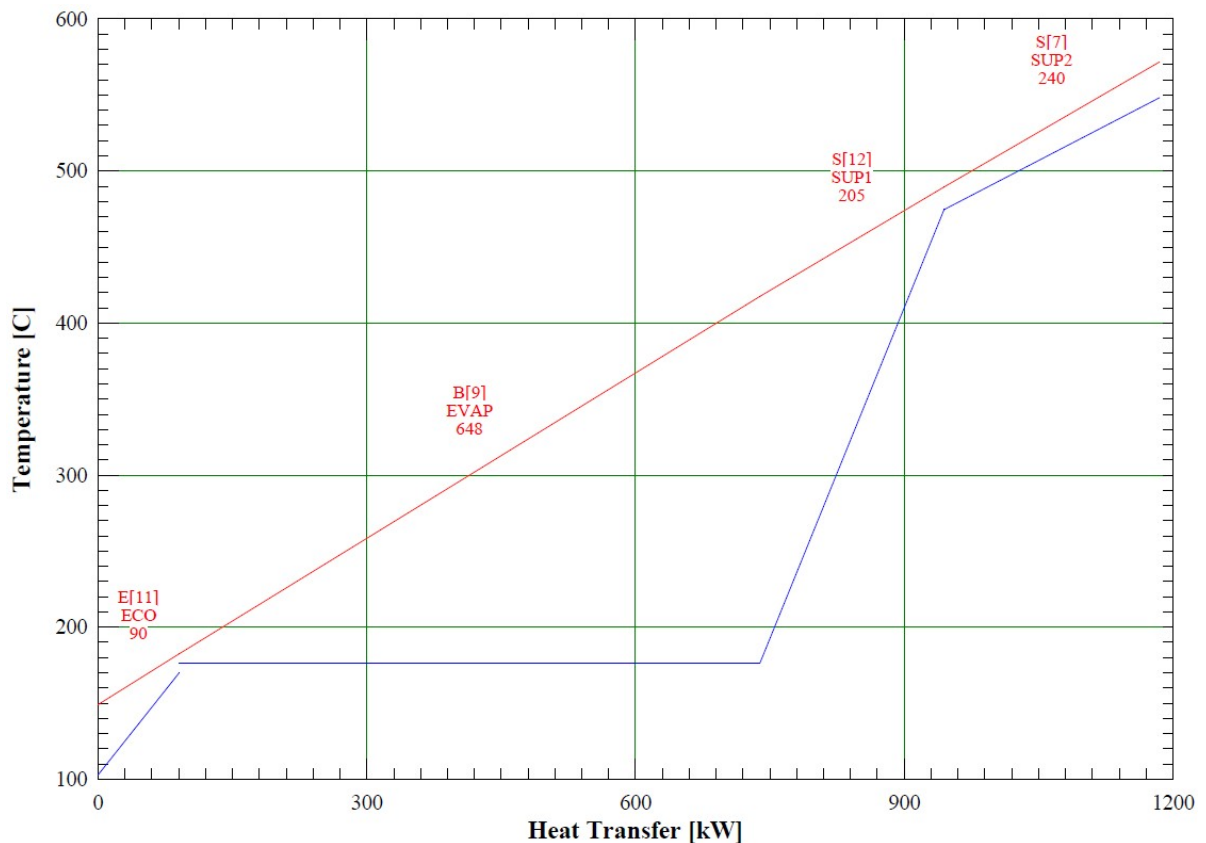


Figure 5.10: Temperature-Heat transfer diagram of the basic, single pressure heat recovery steam generator

Compressor

After the flue gas stream exits the HRSG, a fraction of its mass is sent to the compressor (C in figure 5.9), while the remaining mass fraction is sent to the Rankine part of the combined cycle. To supply the required amount of cooling steam mass flow for the SOFC, the large mass fraction of approximately 86% of the HRSG flue gas outlet stream is supplied to the compressor, to be later merged with the steam flow through the HRSG upstream of SH2. The two streams added together amount to the required cooling steam mass flow of approximately 1.50 kg/s determined with equation 5.2, elaborated in the thermodynamics part of the SOFC. This mass fraction is thus sent back into the Brayton cycle before releasing its latent heat of vaporization by condensation in the Rankine part of the cycle, optimising the overall efficiency of the combined cycle. The compressor PR determines the outlet temperature of the steam according to a similar relation as the gas turbine pressure and temperature ratios. Equation 5.6 states the isentropic relation of the PR and TR of compression [91].

$$\frac{p_{out}}{p_{in}} = \left(\frac{T_{out}}{T_{in}} \right)^{\frac{k}{k-1}} \quad (5.6)$$

The pressure ratio over the compressor is dependant of the pressure ratio of the HTT in the Brayton cycle, the pressure loss of the second superheater in the HRSG and the fuel cell pressure loss. The largest influence, the HTT PR of 6.80 results in a PR of 8.1 for the compressor. With this compression ratio, the outlet temperature results in approximately 475°C. Downstream of the compressor, extra heat addition to the steam is therefore required before the steam can be used as cooling medium for the SOFC.

Since the work of compression increases with increasing compressor inlet temperature, it is important to lower the compressor inlet temperature as much as possible. The work required for compressing a fluid is often presented in an enthalpy-entropy diagram, where the (isentropic) compression work resembles the vertical distance between the two isobars. The relation between increasing entropy with increasing temperature and the diverging isobars in the hs-diagram confirms the increase of compressor work with increasing compressor inlet temperature. It is therefore more efficient to split a mass fraction of the flue gas downstream of the economiser, send it to the compressor and then add heat, than for instance splitting the flue gas flow between the evaporator and economiser and ending up with the desired outlet temperature directly after compressing. The isentropic compression efficiency of the compressor was set to 80%, a common value for the used PR. The required work input to achieve the desired pressure ratio with the selected isentropic efficiency results in approximately 777 kW. The thermodynamic parameters of the compressor are presented in table 5.8.

Table 5.8: Compressor thermodynamic operating specifics

Parameters	Value	Unit
Pressure Ratio	8.1	-
Mass flow	1.19	kg/s
Shaft power	776.7	kW
Mechanical loss	3.1	kW
Isentropic efficiency $\eta_{c,s}$	80.00	%

A determining design feature of the cycle is where the mass flow of the SOFC cooling steam originates from. From the details in figure 5.9 can be seen that approximately 80% of the mass flow is provided by the compressor and only 20% by the evaporator. In the evaporator, a lot of entropy is generated due to the large amount of heat transferred at relatively low temperature. This relation was elaborated in the closed system entropy balance in chapter 2.2. It is therefore beneficial to have a higher mass flow through the compressor compared to the evaporator from an exergetic point of view.

5.2.3. Rankine cycle

This chapter consists the thermodynamic operating parameters of each component in the bottom cycle of the proposed basic power cycle. It is a relatively standard Rankine cycle consisting of a steam turbine, condenser, deaerator and pumps. Figure 5.11 shows the individual components and the corresponding stream parameters regarding pressures, temperatures and mass flows. Since the HRSG is discussed separately in the previous chapter, it is not shown in the figure.

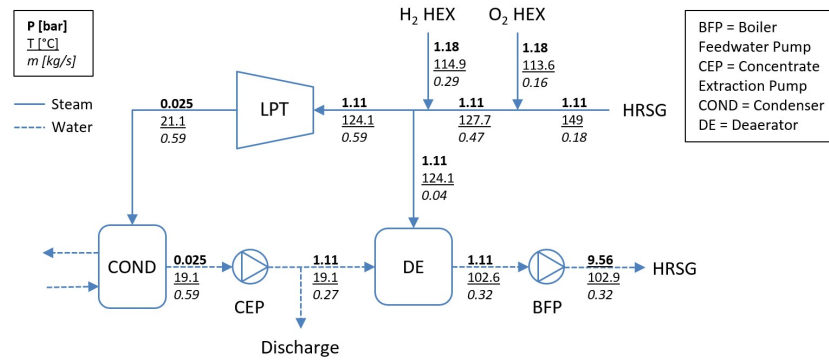


Figure 5.11: Schematic overview of the designed Rankine part of the integrated SOFC combined cycle

Low Pressure Turbine

The LPT inlet conditions depend on the outlet conditions of the HRSG and H_2 & O_2 preheaters. Before the dry steam enters the turbine, a small mass fraction is sent to the deaerator. The efficiency of the steam turbine section is dictated by the dry step efficiency, which is the efficiency of each stage within the steam turbine section. Thermoflex corrects the dry step efficiency when the vapour quality of the steam decreases along the turbine stages. Table 5.9 presents the overall steam turbine operating specifications.

Table 5.9: Low Pressure Turbine thermodynamic operating specifics

Parameters	Value	Unit
Pressure Ratio	44.40	-
Mass flow	0.59	kg/s
Shaft power	261.3	kW
Exhaust vapour quality	0.893	-
Mechanical loss	1.05	kW
Dry step efficiency η_{dry}	85.00	%
Overall isentropic efficiency η_{ST}	83.07	%

The outlet vapour quality of the wet steam is an important parameter for the design of the low pressure turbine. When the vapour quality drops below a certain threshold, liquid droplets in the vapour-liquid mixture can erode the turbine blades which decreases the turbine efficiency and results in more frequent necessary maintenance. A minimum steam turbine exit vapour quality of approximately 0.90 is considered to be allowable by common practices [55][71][72]. The LPT expansion path is depicted in the enthalpy-entropy diagram, also referred to as Mollier diagram in figure 5.12, where the lines of constant vapour quality are depicted together with the two isobars and the linear steam expansion path.

The Wilson line depicted in the Mollier diagram defines the quality at the beginning of condensation in the LPT. The default value is 0.97, below this value an efficiency decrement is applied to the stages below this via equation 5.7.

$$\eta_{ST} = \eta_{dry} - B(1 - x_M) \quad (5.7)$$

Where η_{ST} is the corrected step efficiency, η_{dry} is the dry step efficiency, x_M the mean step quality and B the Baumann coefficient, which is the moisture efficiency penalty. When a stage is partially

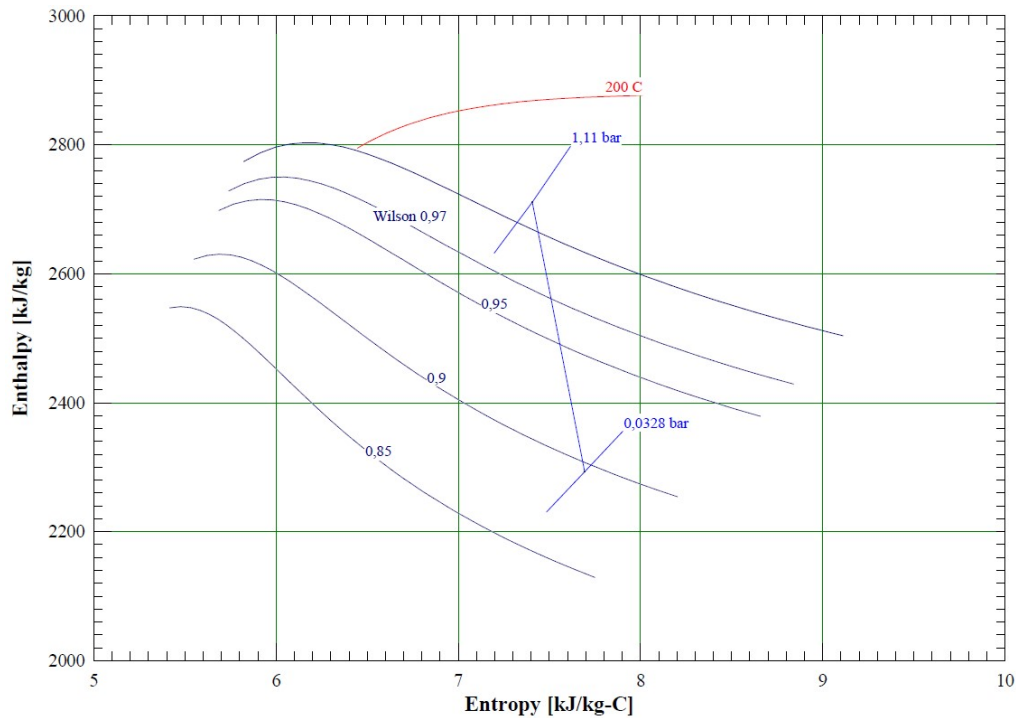


Figure 5.12: Mollier diagram with the LPT expansion path, the corresponding isobars and lines of constant vapour quality

above and partially below the Wilson line, the part below the Wilson line is corrected proportionate with a default Baumann coefficient of 0.72 [31].

Condenser

The condenser (COND in figure 5.11) is a heat exchanger in which latent heat transfer occurs to condense the incoming vapour-liquid mixture to a pure liquid stream. The supplied cooling water, is sub cooled with an incoming temperature of 5°C where the design point minimum pinch is set to 3°C and the operating pressure 0.025 bar [71]. Chapter 7.4 discusses the design of the condensers in depth for a more detailed understanding of the component. The operating specifics are presented in table 5.10.

Table 5.10: Condenser operating specifics

Parameters	Value	Unit
Operating pressure	0.025	bar
Saturation Temperature	21.08	°C
Minimum pinch	3.00	°C
Condensate subcooling	2.00	°C
Heat rejection	1288.1	kW

Deaerator

The Rankine cycle is equipped with a deaerator (DE in figure 5.11) for the initial removal of dissolved gasses from the boiler feedwater, which is its primary task [59]. The deaerator consists of two tanks, a smaller deaeration head tank that is placed onto a larger water tank, also referred to as the feedwater tank. The feedwater tank ensures a small amount of water storage for the feedwater pump in the case the water supply from the condenser is lost. The deaerator is situated upstream of the boiler feedwater pump and downstream of the concentrate extraction pump. The presence of oxygen in the feedwater with a concentration exceeding eight parts per billion (ppb) can result in severe corrosion and tube failure within the boiler, it is therefore an essential part of the cycle [59]. The deaerator operates at a pressure of 1.11 bar and has an outlet temperature of 102.5°C which implies a fully saturated liquid at the outlet.

Pumps

The basic cycle is equipped with two pumps, the concentrate extraction pump CEP arranged downstream of the condenser and the boiler feedwater pump BFP, downstream of the deaerator. The concentrate extraction pump pressurises the condensed water coming from the condenser to approximately atmospheric pressure so that a mass fraction of the water equal to that of the summation of the incoming hydrogen and oxygen mass flow can be discharged to prevent a buildup in the closed cycle. The boiler feedwater pump elevates the water pressure to the desired SOFC and HTT operating pressure, taking into account the steam side pressure losses of the individual components within the HRSG. The overall performances of the pumps are presented in table 5.11.

Table 5.11: Pump operating specifics

Parameters	CEP	BFP	Unit
Pressure rise	1.09	8.45	bar
Required shaft power	0.14	0.61	kW
Pump isentropic efficiency	70.00	70.00	%

Final schematic overview of the basic cycle

With the Rankine part of the combined cycle specified, the concluding schematic flow scheme of the basic proposed SOFC integrated combined power cycle is stated in figure 5.13. The thermodynamic properties at each stage of the cycle regarding pressure, temperature and mass flow are stated in the figure. Appendix B gives an even more in depth overview of the designed cycle, including enthalpy values for each stream.

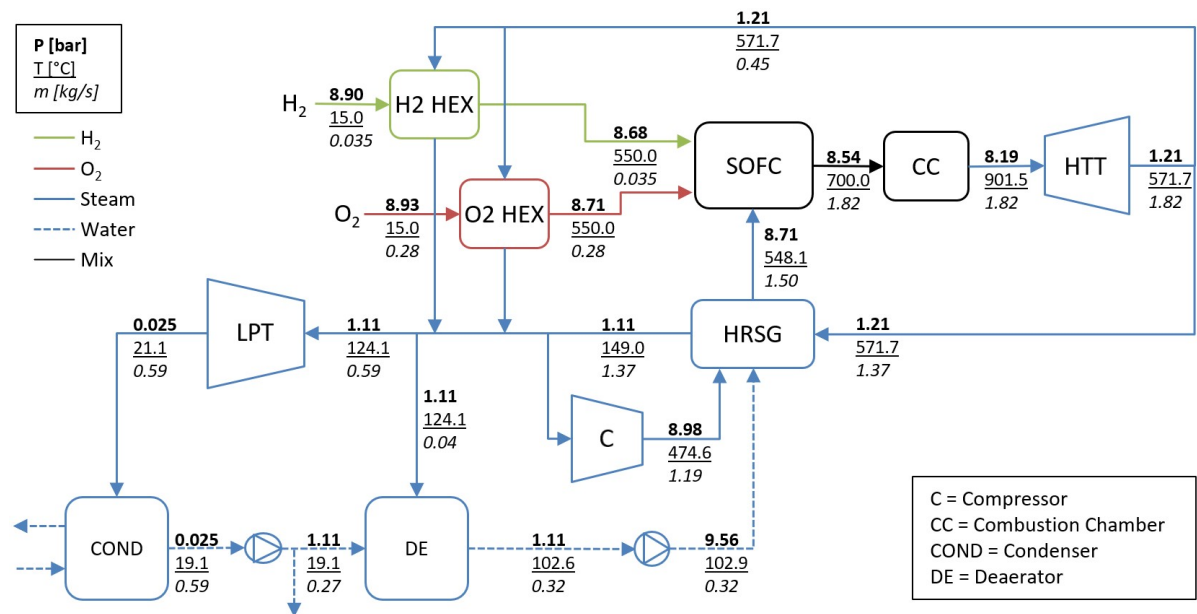


Figure 5.13: Schematic overview of the designed integrated SOFC combined power cycle

An overview of the power generating and consuming components within the SOFC-integrated combined cycle together with the overall losses is stated in table 5.12. The total electrical power output amounts to 3016 kWe, where 2184 kWe is supplied by the SOFC and 832 kWe is supplied by the combined power cycle.

Table 5.12: Basic cycle power distribution overview

Parameters	Value	Unit
HTT expansion power	1366.1	kW
Compression power	773.6	kW
LPT expansion power	264.4	kW
Total pumping power	0.8	kW
Total mechanical loss	9.6	kW
Total heat loss	94.3	kW
Gross power cycle output	844.6	kW
Net power cycle output	831.7	kWe
SOFC power output	2184.4	kWe
Total power output	3016.1	kWe

5.3. Basic cycle exergy analysis

As introduced in chapter 2.2, an exergy analysis reveals the losses of each component in a power cycle and thus reveals where improvements can be made for a more efficient system. For each component, the exergy destruction E_d (frequently referred to rate of exergy loss) was defined with the methods introduced in chapter 2.2. The exergy destruction for each component was divided by the total exergy supplied to the system E_{sup} , to get a clear insight about the percentage of supplied exergy lost in that specific component. Table 5.13 presents the losses per component in the cycle as exergy destruction in kW and as percentage of the total supplied exergy to the cycle. The overall exergy efficiency η_{Ex} of the cycle is defined as the ratio between the total exergy that leaves the system and the total exergy supplied to the system [95], stated in equation 5.8. The thermal efficiency of the SOFC integrated combined power cycles is determined via the ratio between generated power and the energy supplied to the system stated in Eq. 5.9. Where P_{cycle} is the electrical power generated by the combined cycle with a generator efficiency η_{gen} of 98.5%, and P_{SOFC} being the electrical power generated by the fuel cell [71].

$$\eta_{Ex} = \frac{E_{sup} - \sum E_d}{E_{sup}} \quad (5.8)$$

$$\eta_{LHV} = \frac{P_{cycle} + P_{SOFC}}{\dot{m}_{H_2} LHV_{H_2}} \quad (5.9)$$

A graphical representation of the losses is given in the exergy flow diagram depicted in figure 5.14. The diagram shows how the exergy supplied to the system is either used to generate useful power, or is lost in percentage per component. The green flows represent the exergy leaving the system as useful power, whereas the red flow represents the exergy flow leaving the system as losses. The remaining approximate 2% is the additional exergy put into the system due to compressor and pump work. The width of the flows are scaled according to the contribution of the flows.

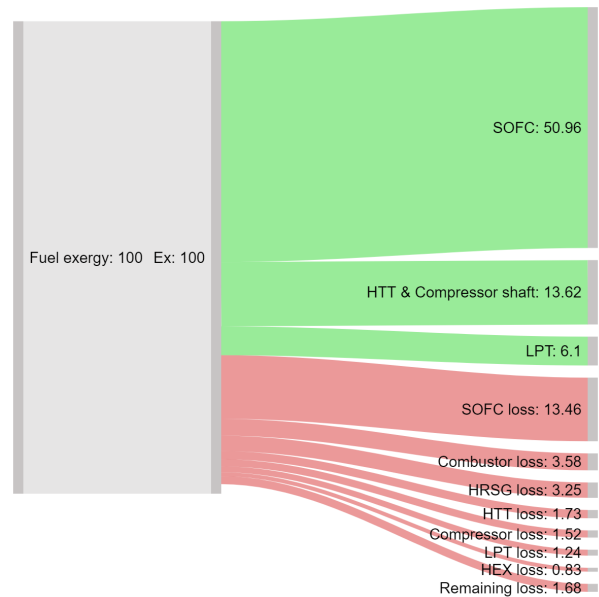


Figure 5.14: Exergy flow diagram of the basic cycle

Table 5.13: Exergy analysis results of the basic power cycle

Component	E_d , kW	Loss, %
SOFC	577.1	13.46
Combustor	153.5	3.58
HRSG	139.2	3.25
High temperature turbine	73.8	1.73
Compressor	65.1	1.52
Rankine Steam Turbine	53.2	1.24
Heat exchangers	35.7	0.83
Drainage	15.7	0.36
Deaerator	9.8	0.23
Condenser	26.6	0.62
Mixing	3.7	0.09
Pumps	0.3	0.01
Exergy efficiency η_{Ex}	73.09%	
Thermal efficiency η_{LHV}	71.79%	

6

Thermodynamic design of the improved power cycle

The improved cycle has a lot of similarities with the basic cycle, the main difference between the cycles is the improved heat transfer between the top and bottom cycle. From the basic cycle exergy analysis became clear that the largest losses occur in the fuel cell, combustor and HRSG. Exergy losses in the fuel cell and combustor are difficult to prevent and/or reduce for a relatively basic power cycle. The HRSG is therefore altered for the improved power cycle. Chapter 4.3 stated that introducing multiple pressure regimes results in loss reduction of the component. A dual pressure HRSG is therefore implemented which is a more efficient solution compared to its single pressure counterpart and a more simple solution compared to a triple pressure HRSG. Due to the fact that the improved HRSG contains more components, higher pressure losses are inevitable. It is therefore that in SOFC integrated Brayton part of the combined cycle operates at a slightly elevated pressure to ensure equal pressure ratios over the LPT and HTT in the top and bottom cycles.

The new design contains a high pressure HP economiser, evaporator and superheater together with the initial LP economiser, evaporator and two superheaters. An additional high pressure turbine is integrated downstream of the HP superheater to extract power from the steam while expanding the medium to the lower pressure regime before entering the LP superheaters. For clarity reasons, the waste heat stream coming from the HTT, which transfers heat to the other stream is again referred to as the flue gas stream. The stream coming from the BFP and leaving for the SOFC as cooling medium is referred to as steam. Some of the thermodynamic states are determined on beforehand due to specified pressure losses of the equipment and the known HTT outlet conditions and LPT operating conditions. Figure 6.1 depicts the thermodynamic states in the improved HRSG that are known in advance, the remaining states will become clear when the optimum pressure ratio of the HPT is determined.

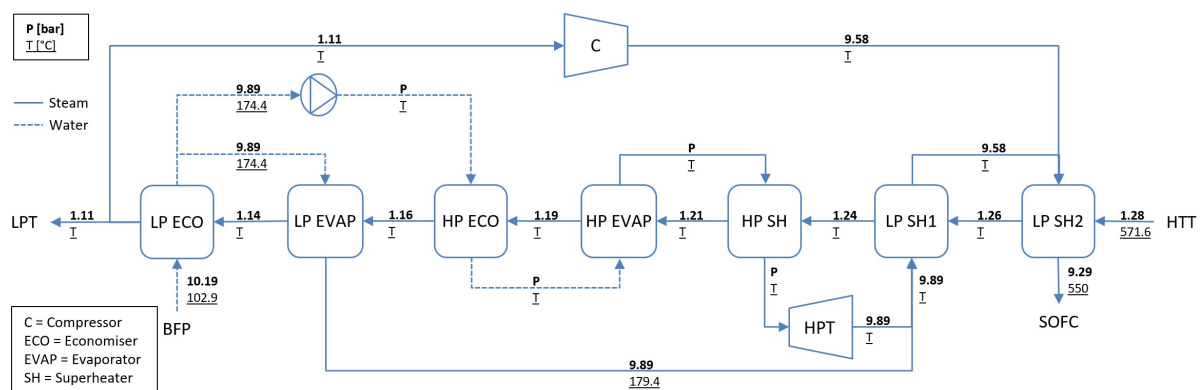


Figure 6.1: Principle flow scheme of the preliminary dual pressure HRSG, HPT and compressor

6.1. HRSG-Steam Turbine

The high pressure section of the HRSG makes it possible to add an additional steam turbine to the improved cycle and thus creating an extra point in the cycle where energy is extracted from the medium. The outlet pressure of the HPT is defined by the operating pressure of the SOFC, HTT and steam pressure losses in the low pressure superheaters of the HRSG. The HPT inlet pressure thus determines the pressure ratio over the turbine and thus the power output. To determine the optimum pressure ratio, the inlet pressure was varied between 15 and 100 bar and plotted against the power output of the combined cycle, excluding the SOFC electrical power output. The results are depicted in figure 6.2, from which can be concluded that the optimal HPT inlet pressure is 45 bar. Since the expansion is limited by the minimum outlet pressure, the outlet pressure and temperature are well above saturation conditions and thus no condensation losses occur.

Section 5.2.3 stated the definition of the steam turbine efficiency in equation 5.7, from this definition, it is logic that the HPT efficiency is higher compared to the LPT efficiency due to the improved mean step quality x_M . The dry step efficiency was stated as 85%, which results in a shaft power of approximately 80 kW. The thermodynamic parameters of the HPT are presented in table 6.1.

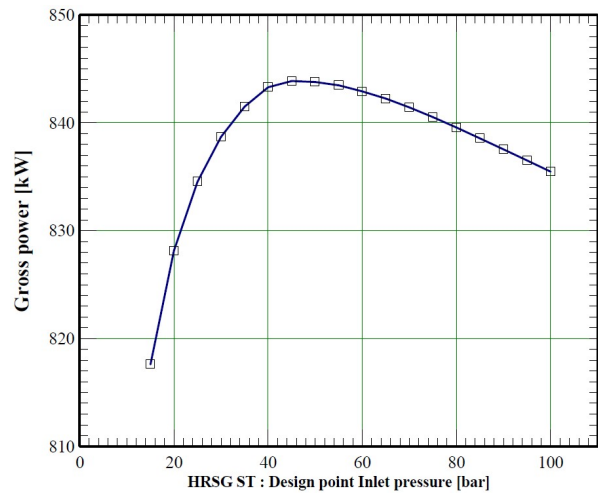


Figure 6.2: HPT inlet pressure variation versus the power cycle output, SOFC power excluded

Table 6.1: High Pressure Turbine operating specifics

Parameters	Value	Unit
Pressure Ratio	4.55	-
Shaft power	79.5	kW
Mass flow	0.23	kg/s
Exhaust vapour quality	1.00	-
Mechanical loss	0.32	kW
Dry step efficiency η_{dry}	85.00	%
Overall isentropic efficiency η_{ST}	86.90	%

Figure 6.3 shows the combined Mollier chart of both steam turbines in the improved cycle. The improved cycle LPT has the same expansion path compared to the basic cycle and expands from the lower isobars where the expansion path of the HPT is plotted between the high pressure isobars. The diagram confirms that the outlet conditions of the HPT are well above the saturation line which explains the higher turbine efficiency η_{ST} compared to the LPT.

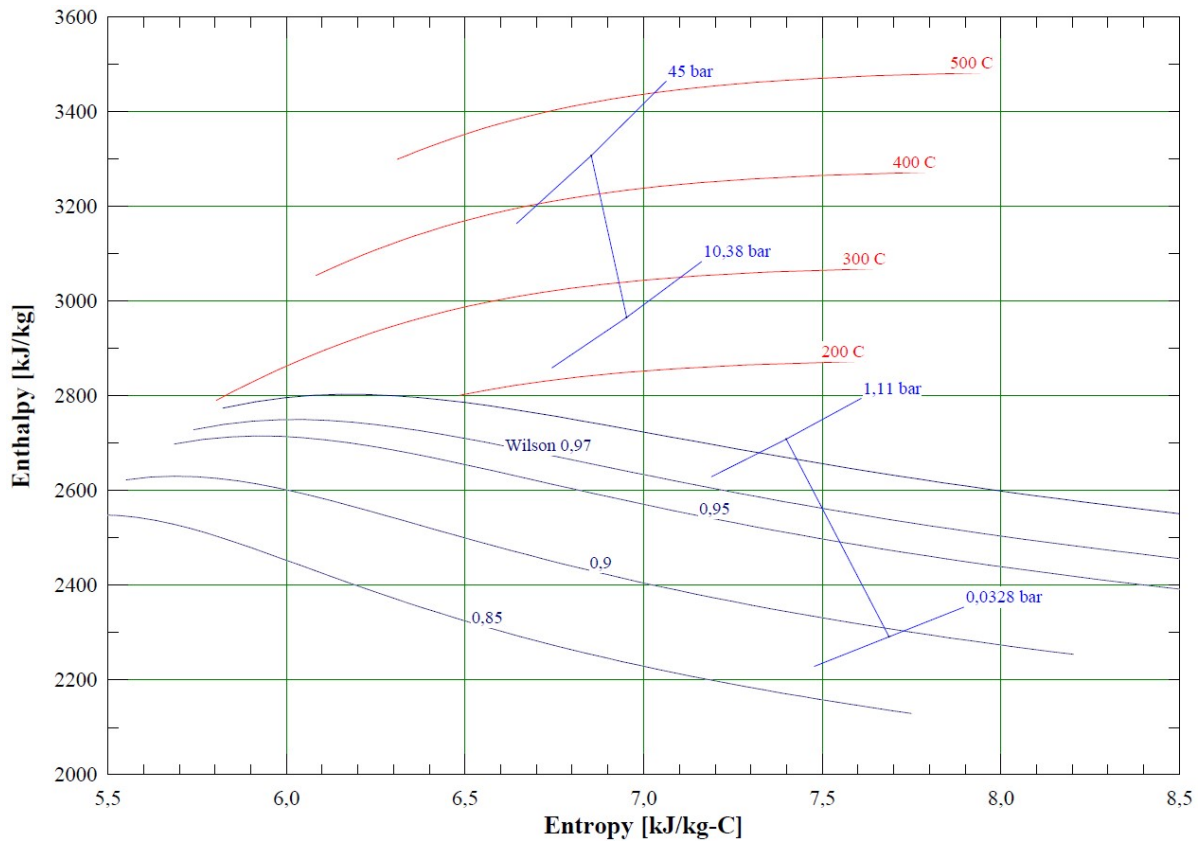


Figure 6.3: Mollier diagram with the expansion path of both steam turbines in the improved cycle

6.2. Dual pressure HRSG design

With the optimum pressure ratio of the HPT specified, most of the remaining thermodynamic states within the improved HRSG will fill in automatically due to the determined pinch points, approach points and saturation temperatures corresponding to the operating pressures. The heat transfer in the economisers is determined by the outlet temperature of the water, which must be saturated before entering the evaporators.

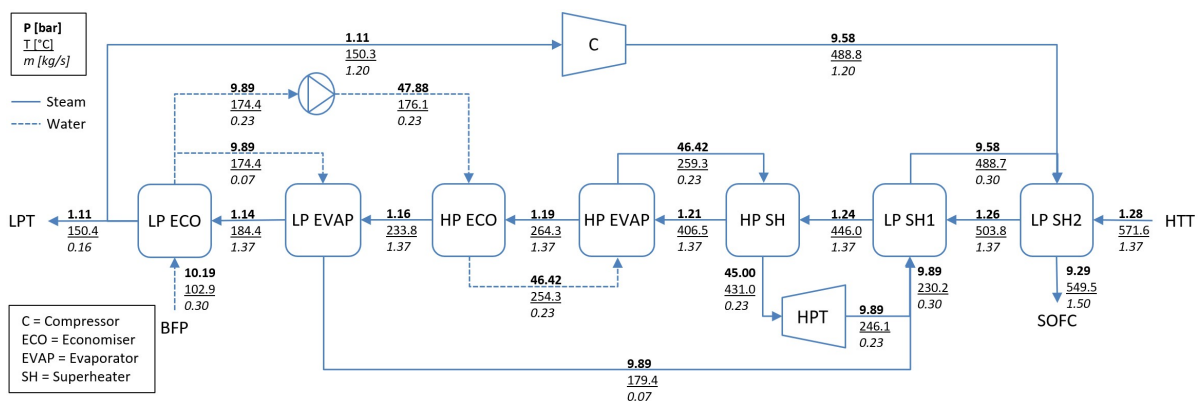


Figure 6.4: Schematic overview of the improved cycle, dual pressure HRSG, HPT and compressor

Although the compressor has slightly different operating conditions, it is not going to be discussed in detail for the improved design. The pressure ratio over the compressor is somewhat larger due to the earlier mentioned reasons, resulting in more compressor work required and an elevated outlet temperature of approximately 13°C. The thermodynamic stream parameters of each component in the

low pressure regime is stated in table 6.2, the high pressure specifics are stated in table 6.3.

Table 6.2: Improved HRSG LP regime thermodynamic operating specifics

Component parameters	LP ECO	LP EVAP	LP SH1	LP SH2	Unit
Heat transfer	91.9	137.0	166.2	198.8	kW
Heat loss	0.46	0.69	0.84	1.00	kW
Flue gas pressure drop	24.9	24.9	24.9	24.91	mbar
Steam pressure drop	0.31	0	0.30	0.29	bar

Table 6.3: Improved HRSG HP regime thermodynamic operating specifics

Parameters	HP ECO	HP EVAP	HP SH	Unit
Heat transfer	83.2	391.8	111.8	kW
Heat loss	0.42	1.97	0.56	kW
Flue gas pressure drop	24.91	24.91	24.91	mbar
Steam pressure drop	1.46	0	1.42	bar

The important design criteria to keep in mind are the pinch points, approach points and steam outlet temperature. The LP & HP pinch and approach points are all 5°C, which is on the lower side but still within an acceptable range. The outlet steam temperature is 549.5°C, and thus within the acceptable margin of 2°C of the mandatory 550°C. The Temperature-Heat transfer diagram of the improved HRSG is depicted in figure 6.5 where the corresponding economisers, evaporators and superheaters are labelled for the specified regions in which they operate. In the figure, the amount of heat transferred from the flue gas stream (red) to the steam (blue) is stated per component. The large discontinuity in the steam line between the HP superheater and first LP superheater is where the HPT extracts energy from the steam after which the HPT exit and the LP steam merge together and enter the first LP superheater.

The high pressure regime results in higher saturation temperatures of the water and thus higher operating temperatures of the HP evaporator compared to the LP evaporator. Chapter 2.2 explained the relation between entropy, temperature and heat, from this can be concluded that higher saturation temperatures result in a smaller entropy increase, which is favourable from an exergetic point of view. It is therefore that approximately 77% of the water/steam mass flow is sent through the high pressure regime of the HRSG and only 23% to the LP EVAP. From figure 6.5 and tables 6.2 and 6.3 can be concluded that the amount of heat transferred in the HP EVAP at higher temperature is more than twice as much as the LP EVAP at low temperature, which will result in a decrease in exergy losses. The exergy analysis in chapter 6.3 will present the exergetic efficiency difference between the two HRSG designs and thus the efficiency increase with the added elevated pressure regime.

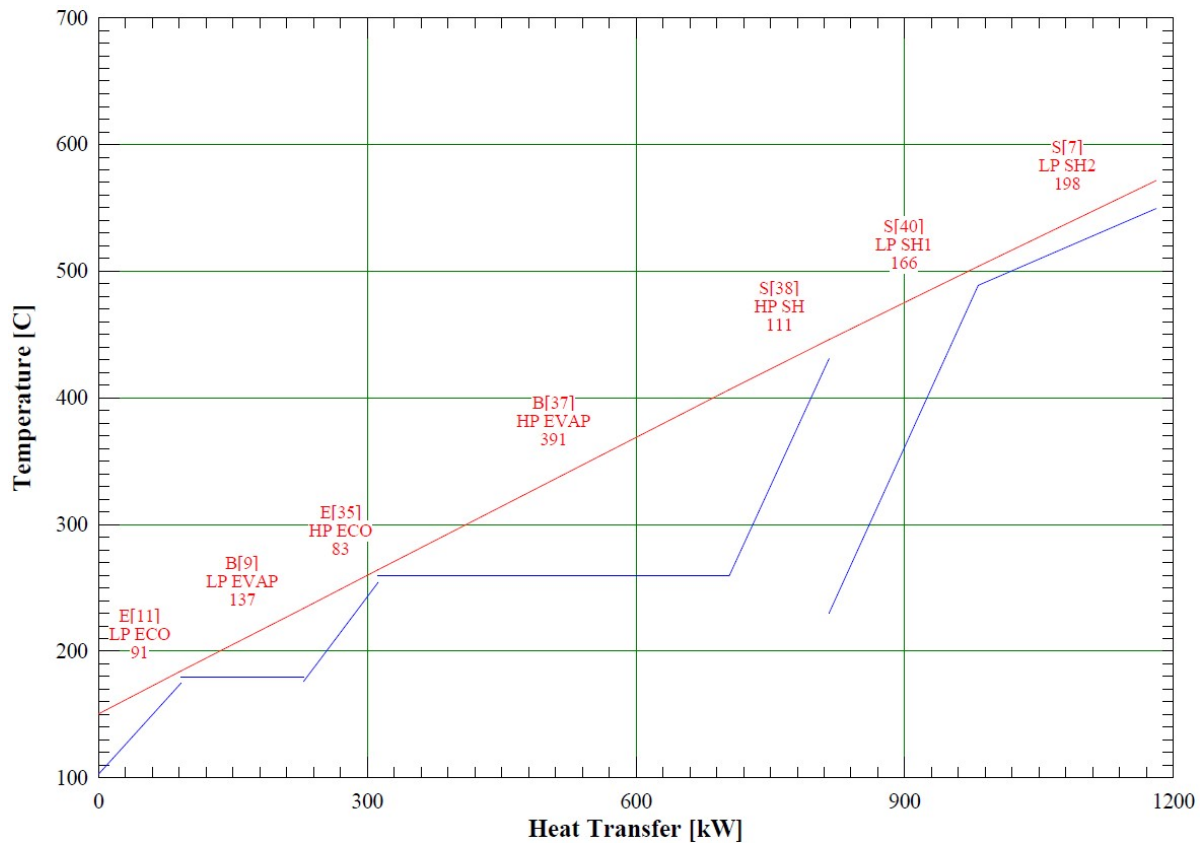


Figure 6.5: Temperature-Heat transfer diagram of the dual pressure HRSG

An overview of the power generating and consuming components within the improved cycle together with the overall losses is stated in table 5.12. The total electrical power output amounts to 3042 kWe, where 2184 kWe is supplied by the SOFC and 858 kWe is supplied by the improved combined power cycle.

Table 6.4: Improved cycle power distribution overview

Parameters	Value	Unit
HTT expansion power	1365.9	kW
Compression power	817.3	kW
LPT expansion power	255.9	kW
HPT expansion power	79.8	kW
Total pumping power	2.9	kW
Total mechanical loss	10.1	kW
Total heat loss	94.3	kW
Gross power cycle output	871.3	kW
Net power cycle output	858.0	kWe
SOFC power output	2184.4	kWe
Total power output	3042.4	kWe

6.3. Improved cycle exergy analysis

With the new design of the HRSG and the added high pressure turbine, a new exergy analysis was made for the improved cycle. The same methods are used to evaluate the system, which are the exergy destruction per component (E_d) and the ratio of exergy destruction with the exergy supplied to the system. A percentage delta was added to the table to compare the loss percentage of the basic cycle to the improved cycle per component. A negative delta indicates a decrease in percentage loss and thus an improvement to the cycle. A positive delta indicates an increase in loss and has thus a negative effect on the overall exergetic efficiency of the cycle. The results of the improved cycle exergy analysis are stated in table 6.5 ending with the final exergetic and thermal efficiencies of the improved cycle.

Table 6.5: Exergy analysis results of the improved power cycle

Component	E_d , kW	Loss, %	$\Delta\%$
SOFC	580.66	13.54	0.08
Combustor	153.59	3.58	0
HRSG	99.36	2.51	-0.74
High Temperature Turbine	74.07	1.73	0
Compressor	68.01	1.59	0.07
Low Pressure Turbine	52.30	1.22	-0.02
High Pressure Turbine	6.99	0.16	-
Heat exchangers	35.67	0.83	0
Drainage	15.64	0.36	0
Deaerator	9.32	0.22	-0.01
Condenser	26.03	0.61	-0.01
Mixing	6.86	0.16	0.07
Pumps	7.32	0.03	0.02
Exergy efficiency η_{Ex}		73.47%	0,38
Thermal efficiency η_{LHV}		72.44%	0,65

From the basic and improved cycle exergy results can be concluded that the improved cycle has an increased total exergetic efficiency of 0.38 percent from 73.09 to 73.47%. The improved HRSG has an exergetic efficiency increase of 0.74%, but due to the elevated operating pressures, compressor and pump losses increased also. An increase in mixing losses in the improved cycle is due to the fact that the number of mixers has doubled compared to the basic configuration. A total exergetic efficiency increase of 0.38% is a fine improvement for a large scale power plant but for a small scale power system such as the SOFC-integrated proposed cycle, not worth implementing due to the extra complexity of the system. The exergy flow diagram of the cycle is depicted in figure 6.6 with the exergy leaving the cycle as loss (red) and the exergy leaving the cycle as useful power (green). Where the remaining approximate 2% is the additional exergy put into the system via compressor and pump work.

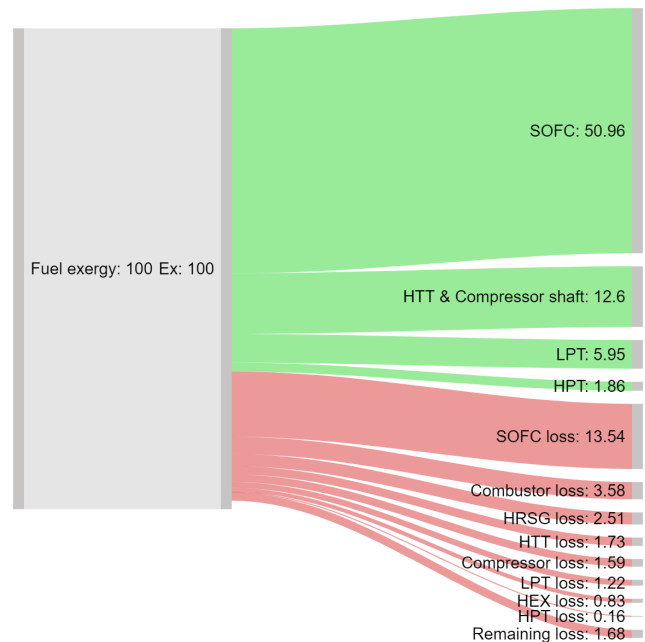


Figure 6.6: Exergy flow diagram of the improved cycle

7

Preliminary equipment design

Chapter 5 and 6 elaborated the thermodynamic design of the basic and improved power cycle, it stated the important parameters for each component and its operating specifics. This chapter will focus on the preliminary design of each individual component, with the exception of the pumps, combustion chamber and deaerator. At the end of this report, a thermodynamic analysis, together with a preliminary component design will give a straightforward concept of the complete SOFC integrated combined power cycle. This chapter is divided into a turbomachinery design part, containing the preliminary design of the HTT, compressor, LPT and HPT. Followed by the preliminary solid oxide fuel cell design, continuing with the sensible and latent heat exchanger designs containing the condenser and evaporator. The chapter ends with a quick comparison between the components and commercially available equipment.

7.1. Turbomachinery design

Chapter 4.1 explained the non-dimensional groups via which the turbomachinery is sized together with the preliminary design steps. The specific speed and the specific diameter, together with the presented Baljé diagram give a good first indication about what type of turbomachinery is best suited for each application. Baljé (1962,1981) generated one of the most iconic comparisons between the specific speed, specific diameter, efficiency and head coefficient for compressors and turbines. The compressor Baljé diagram, shown in figure 7.1 gives a substantial amount of information with a large variety of specific speed and diameter values. In practice, only a small portion of the data is used, radial compressors for instance are best characterised within a N_s range of 0.4-1.8 and values of 1.0-20.0 regarding the specific diameter [47]. For a quick recap, the statements for the non dimensional specific speed and the specific diameter are stated below.

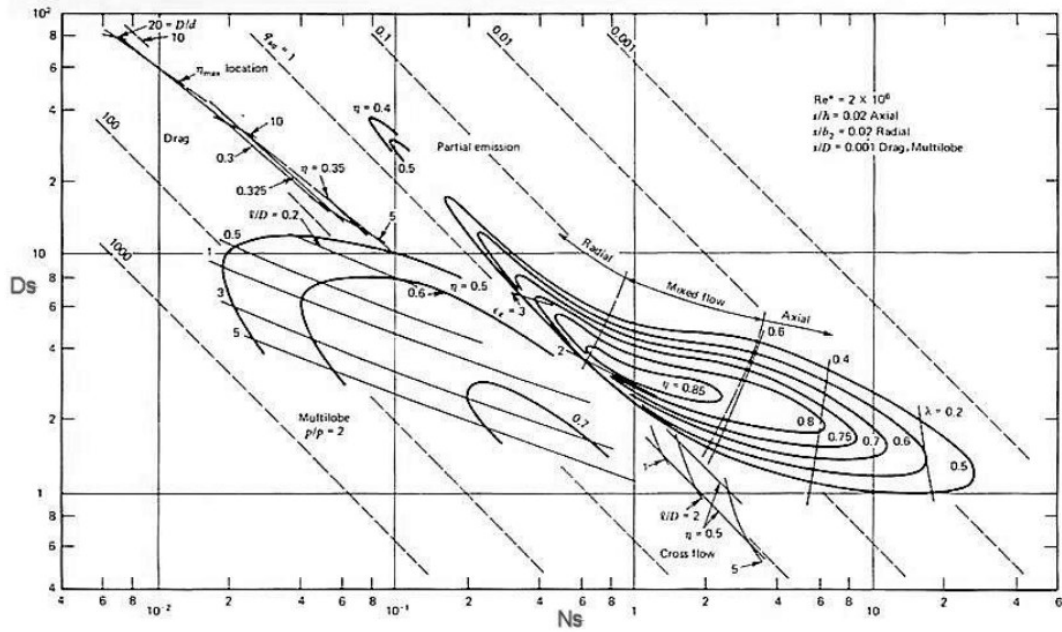
$$N_s = \frac{\left(\frac{\dot{m}}{\rho_{av}}\right)^{0.5} \Omega}{\Delta h_s^{0.75}}, \quad D_s = \frac{d_t \Delta h_s^{0.25}}{\left(\frac{\dot{m}}{\rho_{av}}\right)^{0.5}}$$

Step 1: Select the type of turbomachinery based on maximum pressure ratio and mass flow

Chapter 4.1 presented two morphological charts in figures 4.3 and 4.4 with the general differences in operating characteristics between axial and radial flow turbomachinery. When focusing on the mass flows in the system, both the high temperature turbine and the compressor are within the radial regime with low mass flows of approximately 1.8 and 1.2 kg/s respectively. When concentrating on the pressure ratio's, the HTT and compressor PR are also within the radial configuration, either single stage or dual stage. The LPT is a condensing turbine, which generally have low outlet pressures that result in high overall pressure ratio's. Due to a high PR of 44.4, the LPT is of the axial configuration. The HPT in the improved cycle has a pressure ratio of 4.55 and a low volumetric flow rate of $0.04 \text{ m}^3/\text{s}$, making it a typical micro turbine. Micro turbines are typically of the single stage radial configuration.

Step 2: Determine the optimum N_s range with Baljé diagram

From the Baljé diagrams presented in figures 7.1 and 7.2 can be concluded that the best specific speed operating range for radial turbines is approximately between 0.5 and 0.6 with efficiencies reaching 90%. For radial compressors, the highest efficiency range lies between 0.6 and 0.8 with corresponding efficiencies of approximately 80-85%. Axial turbines have a wider optimum operating range where the efficiency is 90% and more, this operating range is related to a specific speed of $0.5 < N_s < 0.9$ [79].



Reproduced with permission of John Wiley & Sons, Inc.

Figure 7.1: The Baljé N_s - D_s diagram for single stage compressors [69]

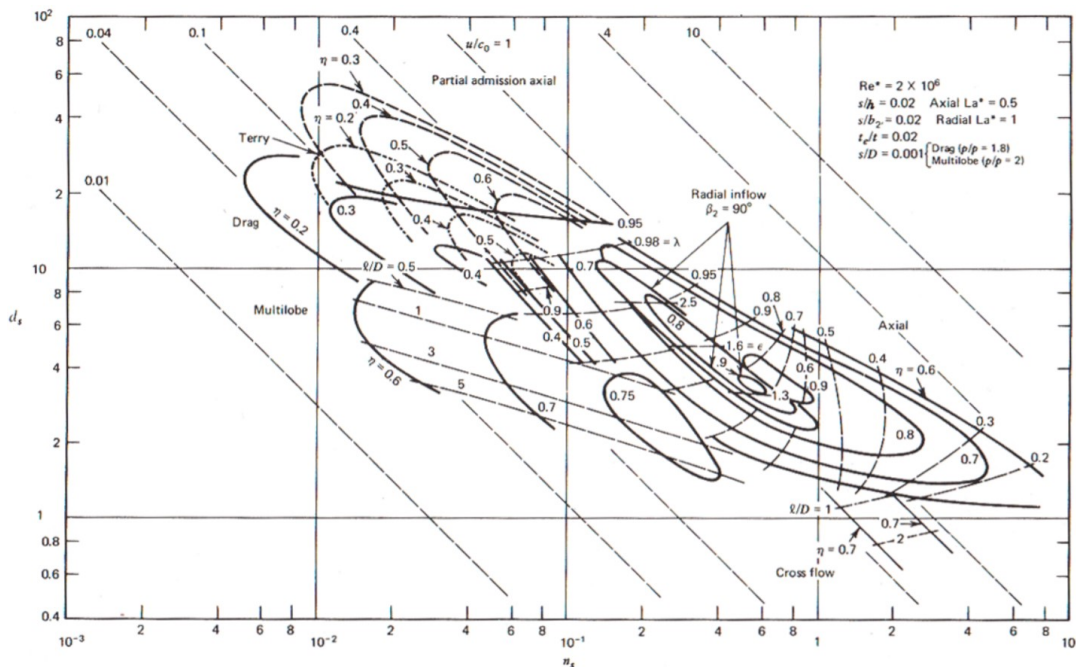


Figure 7.2: The Baljé N_s - D_s diagram for single stage expanders [46]

Step 3: From N_s range, determine number of stages and corresponding shaft speed

To determine the corresponding shaft speeds via the range of specific speed, the volumetric flow rate was calculated with averaged density values between the inlet and outlet conditions of the stages. The mean density values are considered more conform the actual fluid properties since the density varies significantly between inlet and outlet conditions with increasing pressure ratios over the stages [79]. From the definition of N_s can be stated that with low volumetric flow rate a higher rotational speed is required to operate in the desired high efficiency specific speed regime [8]. The rotational shaft speed Ω used in the specific speed definition is expressed in rad/s , converting this to shaft speed N in RPM is realised via the relation $N = 60\Omega/2\pi$.

In an ideal situation, the HTT and the compressor can be arranged on the same shaft where the turbine drives the compressor and the remaining mechanical energy is converted to electrical energy via a generator. To do so, the compressor and turbine must have equal shaft speeds. After several computations became clear that a single stage compressor and single stage HTT do not lie within the same shaft speed for attractive efficiency ranges. A single stage HTT combined with a dual stage compressor do have overlapping shaft speed regions for high efficiency specific speed regions. Figure 7.4 shows the correlation of increasing shaft speed with increasing specific speed for the single stage HTT in its optimum N_s region and both compressor stages. The overlap in shaft speed N is at approximately 75,000 RPM where the Baljé efficiencies of the components are 90%, 85% and 75% for the HTT, first and second compressor stage respectively. The operating points are marked with red circles in figure 7.4 with the corresponding N_s values of 0.4, 0.58 and 0.73.



Figure 7.3: Unshrouded compressor impeller (front left) vs shrouded compressor impeller (right) [78]

Another advantage with this configuration is that with a dual stage compressor, the pressure ratio per stage drops from 8.1 to 2.8, which is a PR suited for shrouded compressors. Shrouded centrifugal compressors are known to operate more efficiently compared to their unshrouded counterparts but have the downside of a lower PR per stage [78]. An example of an unshrouded and shrouded compressor are depicted in figure 7.3 on the front left and right side respectively.

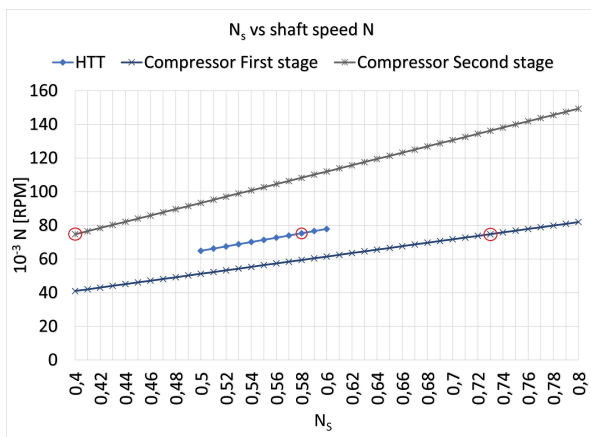


Figure 7.4: Radial turbomachinery N_s versus shaft speed N per stage

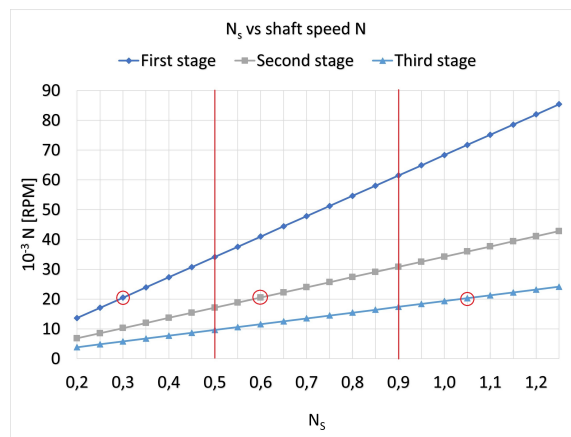


Figure 7.5: Axial LPT N_s versus shaft speed N per stage

To select the shaft speed of the axial LPT, first the amount of stages has to be determined. The optimum number of stages for the LPT is selected according to the maximum PR per stage and design simplicity of the turbine. Increasing the number of stages results in negative effect regarding the simplicity of the design but has a positive effect on the efficiency of the turbine. The optimum pressure ratio per stage is roughly between 2 and 4 for axial turbines, exceeding a stage PR of 4 results in significant

efficiency losses [2]. The axial LPT is therefore designed as a three stage turbine with a stage PR of 3.54.

To determine the shaft speed of the axial LPT, the volumetric flow rate per stage was determined first. From the volumetric flow rate and enthalpy change per stage, the correlation between the specific speed and shaft speed was determined. From this analysis became clear that the three stages do not have matching shaft speeds in the optimum N_s range of 0.5-0.9. The N_s range had to be broadened in order to arrange the three stages on the same shaft. Figure 7.5 depicts the correlation of the increase in shaft speed N with increasing N_s values over a specific speed range of 0.2-1.2 with the optimal N_s range marked with vertical red lines. From the results plotted in figure 7.5 can be concluded that only the second stage operates within the 90% efficiency range and the first and last stage operate in the range of approximately 85% efficiency. A shaft speed N of 20,000 RPM was selected which resulted in N_s values of 0.3, 0.6 and 1.05 for the first, second and last stage respectively (marked in red circles in figure 7.5).

As mentioned earlier, the HPT is a radial micro turbine, which are typically of the single stage radial configuration with high shaft speeds, generally operating between 40,000 and 120,000 RPM [16]. When the HPT is designed for its optimum specific speed range $0.5 < N_s < 0.6$, the corresponding shaft speeds ranges from 360,000 to 435,000 RPM, which is too high. The specific speed has to be scaled down to lower the shaft speed within the acceptable operating window, this results in an efficiency decrease from the optimum 90% to approximately 70% and a N_s value of 0.15.

Step 4: Determine range of optimum D_s corresponding to the selected N_s range

When the optimum specific speed is selected and the corresponding RPM is determined, the corresponding specific diameter can be selected according to the Baljé diagrams. For single stage radial turbines, optimum D_s values range from approximately 3.0 to 3.5. The optimum specific diameter corresponding to 80-85% efficiency for a single compressor stage varies between 3.0 and 4.0. For the axial LPT, the specific diameter has a wider optimum range of approximately $3.1 < D_s < 4.8$. The optimal D_s values for each corresponding N_s are stated in table 7.1, 7.2 7.3 for the radial compressor, HTT and axial LPT respectively. The optimal HPT D_s , corresponding with a N_s value of 0.15 comes down to 10.

Table 7.1: Analysed N_s - D_s coordinates in the Baljé diagram for a radial compressor stage

N_s	0.40	0.44	0.48	0.52	0.56	0.60	0.64	0.68	0.72	0.76	0.80
D_s	6.5	6.1	5.7	5.3	4.9	4.5	4.3	4.1	3.9	3.7	3.5

Table 7.2: Optimal N_s - D_s coordinates in the Baljé diagram for 90% efficiency radial turbines

N_s	0.50	0.51	0.52	0.53	0.54	0.55	0.56	0.57	0.58	0.59	0.60
D_s	3.50	3.45	3.40	3.35	3.30	3.25	3.20	3.15	3.10	3.05	3.00

Table 7.3: Analysed N_s - D_s coordinates in the Baljé diagram for an axial turbine stage

N_s	0.2	0.3	0.4	0.5	0.6	0.7	0.8	0.9	1.0	1.1	1.2
D_s	9.0	7.0	5.0	4.8	4.0	3.4	3.2	3.1	3.0	2.9	2.8

Step 5: From the D_s range, calculate impeller tip diameter d_t

The impeller tip diameter d_t is calculated via the specific diameter equation. For the radial compressor stages and HTT, d_t values were calculated for the points in the Baljé diagram presented in table 7.1 and 7.2. Figure 7.6 shows the decline in impeller tip diameter with increasing specific speed values for the two compressor stages and the single HTT stage. Since the decision was made for a single stage HTT and a dual stage compressor and the most optimal N_s values were selected in step 3, the

corresponding impeller tip diameters are 19.8, 19.2 and 20.6 cm for the HTT and compressor stages respectively.

The design of each stage of the axial LPT is done similar to the radial equipment. From the selected N_s resulted the most optimal value for D_s and with the enthalpy change per stage and the average volumetric flow rate per stage known, a single value of d_t is determined. Figure 7.7 depicts the impeller tip diameter per stage for varying points in the Baljé diagram, with the selected N_s values of 0.3, 0.6 and 1.05, the diameter per stage results in 43.8, 63.8 and 73.1 cm.

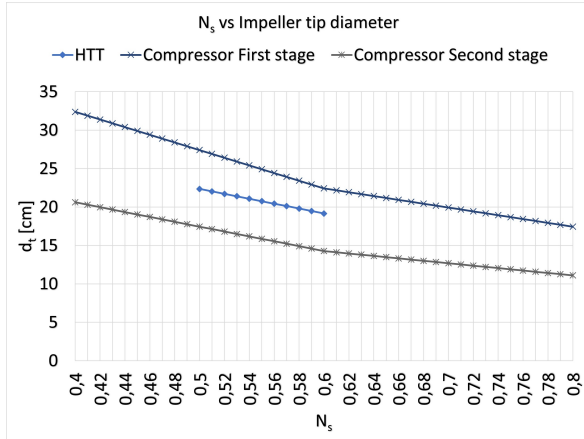


Figure 7.6: Radial turbomachinery N_s versus impeller tip diameter d_t per stage

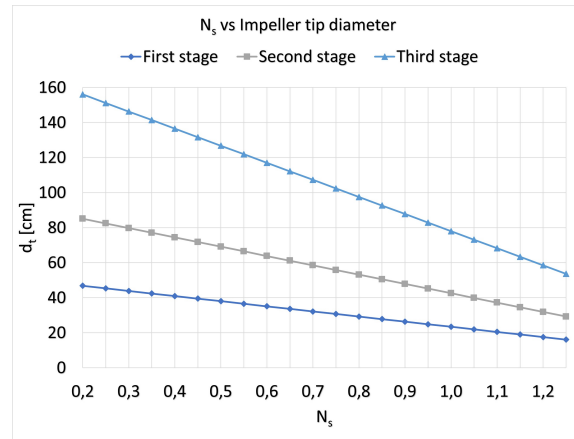


Figure 7.7: Axial LPT N_s versus impeller tip diameter d_t per stage

An overview of the preliminary design results of the basic cycle turbomachinery including the HPT from the improved cycle is stated in table 7.4. The average volumetric flow rate is represented by Q_{av} , which is equivalent to the \dot{m}/ρ_{av} term stated in the specific speed and diameter expressions. The enthalpy rise per stage is represented by Δh_s , the stage pressure ratio by PR_s and the maximum operating efficiency region in the Baljé diagram is defined by η_{Balje} . The differences between the basic and improved cycles regarding the HTT, compressor and LPT are not significant and therefore not discussed separately.

Table 7.4: Preliminary turbomachinery design specifics

Parameter	HTT	Compressor		LPT			HPT	Unit
	Radial	Radial		Axial			Radial	
Stage	Single	First	Second	First	Second	Third	Single	-
P_{shaft}	1361	330	447	103	85	74	80	kW
PR_s	6.80	2.85	2.85	3.54	3.54	3.54	2.55	-
Δh_s	752.3	285.5	384	175.2	145.5	126.8	344.3	kJ/kg
Q_{av}	3.53	1.33	0.62	1.43	4.32	13.55	0.04	m ³ /s
N_s	0.58	0.73	0.40	0.30	0.60	1.05	0.15	-
D_s	3.10	6.50	3.85	7.50	4.00	2.95	10.00	-
d_t	19.8	19.1	20.6	43.9	63.8	73.1	7.7	cm
N	75	75	75	21	21	21	109	10 ³ RPM
η_{Balje}	90.0	85.0	75.0	85.0	90.0	85.0	70.0	%

7.2. Solid Oxide Fuel Cell design

The general principles, operating characteristics and reaction kinetics of a SOFC are well discussed in chapter 3, together with the advantages of integrating a SOFC within a power cycle. This chapter describes the electrochemical performances of a preliminary single planar cell design, to be later on, scaled to a stack size large enough to provide the required power output. The model developed will give a first insight about the operating specifics of the SOFC, its eventual stack size and power densities for such a configuration.

Cooling

The cooling is an important aspect of the fuel cell since the generated heat must be extracted from the cells. As discussed in previous chapters, the essential cooling is done by adding steam, which will be supplied at the cathode side of the cells. This however has a negative effect on the Nernst voltage, the electrochemical driving force stated in equation 3.10 in chapter 3.3. Adding steam to the anode side is however more disadvantageous when focusing how E_{Nernst} is defined. The amount of cooling steam required is dependent on the operating conditions and fuel utilisation of the cell. This mass flow calculation was stated previously in equation 5.2 in chapter 5.2.1.

Design

The data from a metal supported solid oxide fuel cell (M-SOFC) designed by Ceres Power Ltd. is used as a basis for the calculations. Normally, the ceramic oxide material used in a SOFC is yttria stabilised zirconia (YSZ) as the ion conducting electrolyte. The operating temperature of the SOFC (550-700°C) however dictates that another material has to be used since YSZ operates at typically 800-1000°C [3]. Ceres developed a SOFC design suited for low and intermediate temperatures (LT & IT) with a thick film PEN structure (Positive-Electrolyte-Negative) supported by ferritic stainless steel substrates for the mechanical support of the cells [15][45]. Ceres uses gadolinia-doped ceria (CGO) as electrolyte material, which has a far higher ionic conductivity compared to YSZ, allowing operating temperatures down to 500 °C [45]. A schematic diagram of the metal supported cell is depicted in figure 7.8 with the material labelled for the components.

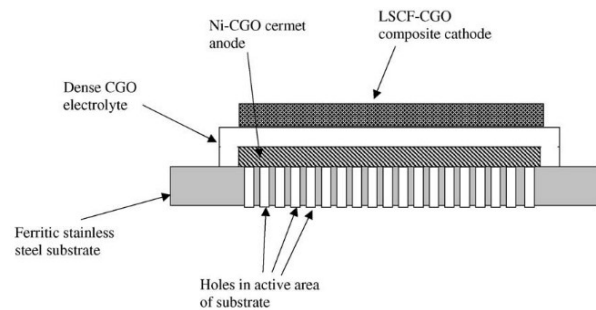


Figure 7.8: Schematic overview of a Ceres Power metal supported cell structure [45]

Table 7.5: Parameters used in the electrochemical model for the metal-supported cell [3][45]

Parameter	Description	Value	Unit
τ_a	Anode thickness	$1.5 \cdot 10^{-5}$	m
τ_{el}	Electrolyte thickness	$1.5 \cdot 10^{-5}$	m
τ_c	Cathode thickness	$5.0 \cdot 10^{-5}$	m
τ_{ic}	Interconnect thickness	$5.0 \cdot 10^{-4}$	m
τ_{ss}	Substrate thickness	$3.0 \cdot 10^{-4}$	m
σ_a	Anode electrical conductivity	$8.0 \cdot 10^4$	S/m
σ_c	Cathode electrical conductivity	$8.4 \cdot 10^3$	S/m
R_{cont}	Contact resistance	$8.46 \cdot 10^{-6}$	Ωm^2
K_i	Ionic conductivity	$2.71 \cdot 10^6$	SK/m

Performance

Several of the critical parameters were fixed on beforehand of the simulation, the LHV efficiency was defined as 65%, the fuel utilisation was fixed at 80%, which in term fixed the cooling steam mass flow and eventually the cell voltage. The cell is operated in steady state conditions, the energy balance of the cell is stated in equation 7.1 where the subscript a and c represent the anode and cathode respectively.

$$\dot{m}_{a,in}h_{a,in} + \dot{m}_{c,in}h_{c,in} = \dot{m}_{a,out}h_{a,out} + \dot{m}_{c,out}h_{c,out} + P_{FC} + \dot{Q} \quad (7.1)$$

The pressure loss over the entire stack is assumed to be 2% of the inlet pressure, the heat loss of the stack to the environment is assumed to be 2% of the hydrogen LHV. The energy balance stated in Eq. 7.1 and the electrochemical behaviour of the cell are dependent on the incoming flows at the anode and cathode, the equations are thus calculated simultaneous. For the model, a lumped parameter model is used which implies that there is no temperature gradient in all directions, the current density has a constant value and the voltage potential is a constant developed by the outlet compositions. The Nernst voltage is at its minimum at the outlet due to the compositions of the reactants and steam [72].

As explained in chapter 3.3, the main losses within a cell are due to activation, ohmic and concentration polarisation. The concentration losses become more relevant when operating at the limiting current density, this will not be the case and therefore the concentration overpotential will not be taken into account. The area specific ohmic resistance of the PEN structure is calculated via equation 7.2 and the Ceres specific data stated in table 7.5 and amounts to $0.19 \Omega cm^2$. The total area specific resistance (ASR) of the PEN structure is taken from literature at the average operating temperature of the SOFC and amounts to $0.31 \Omega cm^2$ [15][45]. With the area specific ohmic losses determined and the total ASR of the PEN structure known from literature, the contribution of the area specific activation overpotential is thus approximately 40% of the total ASR.

$$R_{ohm} = \frac{\tau_a}{\sigma_a} + \frac{\tau_c}{\sigma_c} + \frac{\tau_{el}}{\sigma_{el}} + R_{cont} \quad (7.2)$$

The electrochemical results of the designed single metal supported solid oxide fuel cell are stated in table 7.6.

Table 7.6: Electrochemical results of the M-SOFC

Parameter	Description	Value	Unit
T_{out}	Outlet temperature	700	°C
p_{out}	Outlet pressure	8.54	bar
x_{H_2}	Outlet anode mol percentage	0.20	-
x_{O_2}	Outlet cathode mol percentage	0.02	-
E_0	Potential voltage	1.01	V
E_{Nernst}	Nernst voltage	0.91	V
E_c	Cell voltage	0.83	V
ASR	Area Specific Resistance	0.31	Ωcm^2
P_{dens}	Power density	203.7	mW/cm^2
i	Current density	0.24	A/cm^2
P_{cell}	Cell power	3.10	W

The relation between the current density, cell voltage and power density is plotted in figure 7.10, which shows the expected parabola considering how the power is defined ($P=EI$). The relation between the cell voltage, power density and fuel cell efficiency is plotted in figure 7.9. For each power density, the fuel cell can be operated at two cell voltages (apart from the voltage corresponding to the maximum power density), the higher voltage or the lower voltage. For instance, when focusing on figure 7.9, a power density of $0.3 W/cm^2$ can be operated at a cell voltage of $0.8 V$ or $0.12 V$. The higher voltage will correspond to a cell efficiency of approximately 62%, where the lower voltage will only operate with an efficiency of approximately 10%. The higher voltage is therefore typically the operating voltage for a certain power density. It also explains why, from an efficiency standpoint, a higher operating voltage is chosen compared to the one with maximum power density. For the LHV efficiency of 65%, the corresponding surface power density is $0.20 W/cm^2$ at an operating cell voltage of $0.83 V$, this, in turn, corresponds to a current density of $0.24 A/cm^2$ which can be seen from figure 7.10.

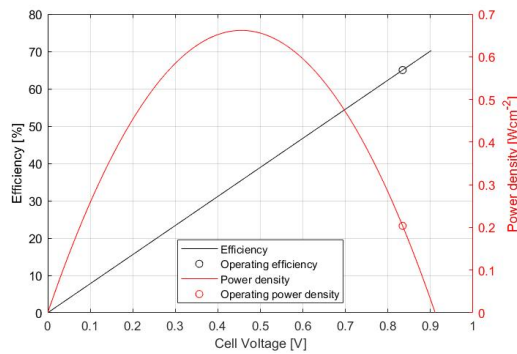


Figure 7.9: Cell voltage vs efficiency vs power density of the M-SOFC

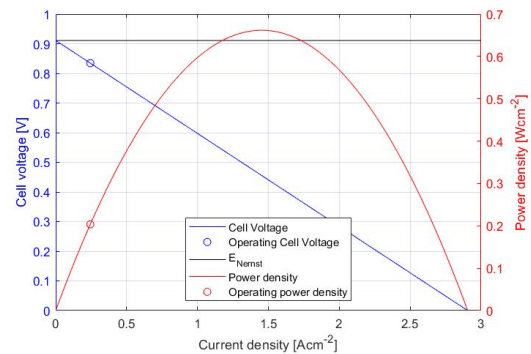


Figure 7.10: Current density vs cell voltage vs power density curves of the M-SOFC

Stack design

The developed performances showed the behaviour at the outlet conditions of a single cell. A single cell however, does not produce a useful power output, multiple cells are therefore connected both in series and/or parallel to compose a bipolar plate. Multiple bipolar plates make up a stack that is capable of producing a usable amount of power. The size of a stack, capable to deliver the required power output is determined in this section. A schematic side view of a co-flow SOFC stack can be seen in figure 7.11, where the single cell unit consists of the PEN structure, an air/oxidiser channel, a fuel channel and interconnect on both sides. A schematic top view of the bipolar plate is showed in figure 7.12, where can be seen that it consists of nine cells. The active cell area of a single cell taken as 15.2 cm^2 , which is a standard cell size [45]. A bipolar plate thus contains a total active cell area of 136.8 cm^2 . The total bipolar plate size, including its air and fuel manifolds is determined to be 250 cm^2 , with this, an indication about the final stack size can be computed.

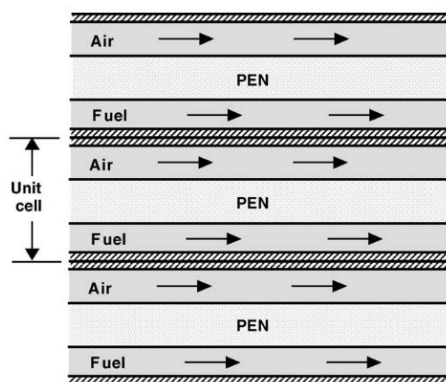


Figure 7.11: Schematic side view of a part of the planar SOFC stack showing the unit cell [45]

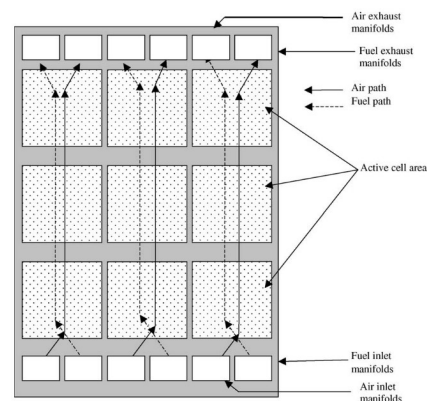


Figure 7.12: Schematic top view of a 9-cell bipolar plate [45]

The computed results give a first indication about the total stack volume based on the bipolar plate area and thickness. Typical specific marine fuel cell power modules are stacks with a power output of 200 kW, multiple 200 kW blocks, electrically-configured in parallel, are currently developed by Ballard [13] for approximate power sizes of 1-3 MW. In this case eleven 200 kW modules would be able to deliver the required power output, the results of a possible stack size are stated in table 7.7. What must be emphasised is that this is not the total size of the complete fuel cell system but only the volume of the stack.

Table 7.7: Geometrical and total power result of the designed M-SOFC stack

Parameter	Description	Value	Unit
A_{cell}	Active cell area	15.20	cm^2
A_{BP}	Bipolar plate area	250	cm^2
$Nr_{cells,stack}$	Nr of cells per stack	64163	-
$Nr_{BP,stack}$	Nr of bipolar plates per stack	7129	-
Nr_{stack}	Nr of stacks	11	-
V_{stack}	Single stack volume	0.30	m^3
P_{stack}	Single stack power	200	kW
Nr_{BP}	Total nr of bipolar plates	78422	-
Nr_{cells}	Total nr of cells	$705.8 \cdot 10^3$	-
V_{FC}	Total combined stack volume	3.30	m^3
P_{FC}	Total combined stack power	2200	kW

7.3. First steps of the heat exchanger design procedure

As stated in chapter 4.4, the design procedures of the heat exchangers in the cycle are executed according to the method introduced by Sinnott & Towler [83]. To make a fair comparison between different types of heat exchangers, two designs were made. A shell and tube design and a welded plate design. The first steps of both design procedures are similar and stated below, the remaining design steps are further elaborated in appendix A.3 for the shell & tube configuration and appendix A.4 for a detailed insight in the welded plate heat exchanger designs.

Step 1: Specification & Duty

The first step in the design procedures is to define the duty of the heat exchanger, this is achieved with the mass flow, specific heat of the stream and temperature differences and is stated in equation 7.3.

$$Q = \dot{m}C_p\Delta T = \dot{m}\Delta h \quad (7.3)$$

Step 2: Collect physical properties

The next step is to collect all relevant physical properties of the streams at corresponding temperatures and pressures. Properties such as the specific heat, thermal conductivity, density and viscosity at both inlet and outlet conditions need to be determined. The NIST database was used to retrieve the required thermodynamic properties of the substances via the program REFPROP [74].

Step 3: Assume overall coefficient U_0

Up next, a value for the overall coefficient $U_{0,ass}$ must be assumed. The general equation of heat transfer across a surface was stated in chapter 4.4 and now again in equation 7.4.

$$Q = U_0A\Delta T_{lm} \quad (7.4)$$

A value of U_0 must be assumed in the beginning of the design stages to be validated iterative later on in the process. The assumed U_0 based on the properties and phases of the hot and cold streams together with the type of heat exchanger. This assumption is done according to data found in tables from Sinnott & Towler [83].

Step 4: Calculate the logarithmic mean temperature difference ΔT_{lm}

Before the area of the heat exchanger can be determined, the logarithmic mean temperature difference ΔT_{lm} needs to be determined, which is the effective driving force in a heat exchanger. The logarithmic mean temperature difference is only applicable to sensible heat transfer in co-current or counter current flow, for design simplicity, true counter current flow is assumed. Equation 7.5 is used when the specific heats and overall heat transfer coefficient are assumed to be constant and heat losses are negligible.

$$\Delta T_{lm} = \frac{(T_1 - T_4) - (T_2 - T_3)}{\ln \frac{(T_1 - T_4)}{(T_2 - T_3)}} = \frac{\Delta T_1 - \Delta T_2}{\ln \frac{\Delta T_1}{\Delta T_2}} \quad (7.5)$$

With T_1 being the temperature of the hot fluid at its inlet, T_2 being the hot fluid temperature at its outlet, T_3 being the cold fluid temperature at its inlet and T_4 the cold fluid temperature at its outlet. Figure 7.13 shows the temperature development of both streams with the corresponding temperature differences ΔT_1 and ΔT_2 to determine ΔT_{lm} .

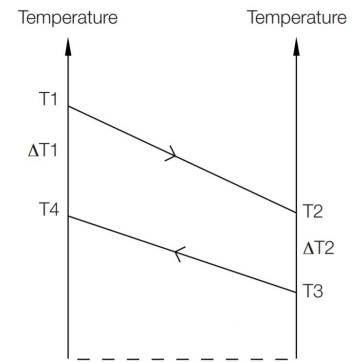


Figure 7.13: Standard heat exchanger temperature diagram

Step 5: Calculate heat transfer area

Now that the duty is determined, the overall coefficient U_{ass} is assumed and the logarithmic mean temperature difference is calculated, a first indication of the heat exchanger area can be determined via equation 7.6.

$$A = \frac{Q}{U_0 \Delta T_{lm}} \quad (7.6)$$

This area indication is highly dependent on the assumed value of the overall heat coefficient U_0 , the validation of this coefficient is therefore a crucial step of the design procedure. The final overall coefficient of heat transfer is the reciprocal of the overall resistances to heat transfer, which is the sum of the individual resistances [83]. For shell and tube heat exchangers, the formula for heat exchange across a typical tube is used which is stated in equation 7.7. The subscripts o , i indicate the outside and inside tube coefficients and od & id express the corresponding dirt coefficients.

$$U_0 = \left[\frac{1}{\alpha_o} + \frac{1}{\alpha_{od}} + \frac{d_o \ln \left(\frac{d_o}{d_i} \right)}{2\lambda_w} + \frac{d_o}{d_i} \frac{1}{\alpha_{id}} + \frac{d_o}{d_i} \frac{1}{\alpha_i} \right]^{-1} \quad (7.7)$$

For plate heat exchangers (PHE), the overall heat transfer coefficient differs from its shell and tube alternative due to obvious geometry differences. The PHE overall heat transfer coefficient is stated in Eq. 7.8 with subscripts h indicating the hot stream and c the cold stream.

$$U_0 = \left[\frac{1}{\alpha_h} + \frac{1}{\alpha_{hd}} + \frac{P_t}{\lambda_w} + \frac{1}{\alpha_c} + \frac{1}{\alpha_{cd}} \right]^{-1} \quad (7.8)$$

7.3.1. Shell & tube versus welded plate heat exchangers

A comparison was made between the shell and tube results and the welded plate results regarding overall dimensions and a few operating parameters. The results of this comparison are depicted in table 7.8 for the minimum pinch of 15°C for the gas to gas heat exchangers and a minimum pinch of 5°C for the economiser. Where 5 and 15°C are typical values for shell and tube heat exchangers and are frequently used values used in Graz cycle literature [71] [72]. The compactness of the heat exchangers is expressed in the term β , which is the heat transfer surface area density and is defined as the ratio of heat transfer area over the volume of the exchanger in m^2/m^3 .

Table 7.8: Shell & tube vs welded plate heat exchanger comparison

Parameter	H_2		O_2		ECO		SH1		SH2		Unit
	S&T	PHE	S&T	PHE	S&T	PHE	S&T	PHE	S&T	PHE	
Q	271.7	271.7	147.6	147.6	90.7	90.7	205.3	205.3	240.6	240.6	kW
U_0	5.2	127.1	5	95	36.4	122.5	7.5	58.8	8.6	86.3	$W(m^2\text{ }^\circ C)^{-1}$
A	1046	44.2	574	30.7	88	29.3	391	45.8	1818	158.9	m^2
V	7.2	0.075	4.0	0.045	0.8	0.08	2.7	0.16	12.2	0.49	m^3
β	145	591.5	142	679.7	107	360.7	144	282.5	149	324.2	m^2/m^3

It is well known that plate heat exchangers have a significant higher area density compared to shell & tube exchangers, a graphical representation of this difference is depicted in figure 7.14 where both heat exchangers are used for an equal duty. Focusing on the results presented in the table, the main differences between the two designs are the overall heat transfer coefficient, volume and thus compactness of the exchangers. When focusing on the basic heat transfer equation stated in Eq. 7.4, the duty and logarithmic mean temperature difference are independent on the type of heat exchanger, which implies that the only difference are U_0 and the area required. The significant difference in U_0 values between the two designs is directly related to the corrugated plates in the welded heat exchanger design. This design ensures turbulent flow between the plates and increases the overall heat transfer coefficient. When the overall coefficient increases, less area is required to transfer the heat between flows. Combining this with the fact that plate heat exchangers have a higher compactness results in a significant decrease in heat transfer volume V of the equipment. Standard heat transfer surface area density values of shell and tube heat exchangers are typically within the range of $60 < \beta < 500$, where for plate heat exchangers the typical range is $120 < \beta < 700$. From the results can be concluded that the welded plate heat exchangers are the better solution for the sensible heat transfer within the cycle. It is therefore that from now on, if possible, the remainder of the exchangers are going to be designed only as a welded plate heat exchanger. When the operating conditions exceed the feasible operating conditions of a WPHE, a shell and tube design will be made.

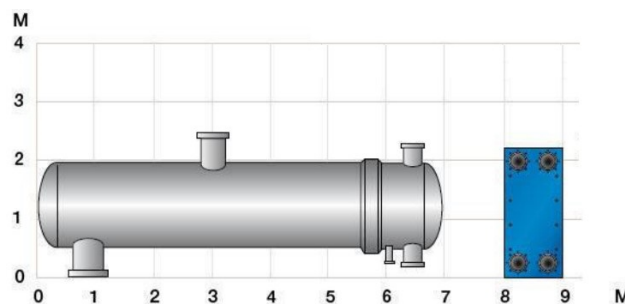


Figure 7.14: A size comparison between a Shell & tube design vs a plate heat exchanger design for equal heat transfer duty [36]

7.3.2. Sensible heat exchanger design results

All key parameters and results of the basic cycle sensible heat exchangers design are stated in table 7.9. The design was, as stated in previous section and section 5.1 made with a minimum temperature difference of 15°C for the gas to gas equipment and 5°C for the liquid to gas equipment. The maximum pressure drops defined in the thermodynamic simulations were leading parameters while designing the equipment. The hydrogen and oxygen preheaters have a maximum cold side pressure drop ΔP_C of 30 mbar and a maximum hot side pressure drop ΔP_H of 0.2 bar. The HRSG equipment has a maximum ΔP_C and ΔP_H of 28 and 25 mbar respectively. For the basic cycle, all equipment was designed as a welded plate heat exchanger, the complete WPHE design steps undertaken are elaborated further in appendix A.4.

Table 7.9: Welded plate exchanger design specifications for the basic cycle

Parameter	H_2	O_2	ECO	SH1	SH2	Unit
Q	271.7	147.6	90.7	205.3	240.6	kW
U_0	127.1	95	122.5	58.8	86.3	$W(m^2^\circ C)^{-1}$
A	44.2	30.7	29.3	45.8	158.9	m ²
ΔT_{lm}	51.2	50.8	25.8	81.4	18.9	°C
ΔP_H	28.1	29.7	23.8	24.8	24.7	mbar
ΔP_C	0.5	5.5	0.001	0.1	3.9	mbar
V	0.075	0.045	0.08	0.16	0.49	m ³
β	591.5	679.7	360.7	282.5	324.2	m ² /m ³

The improved cycle sensible heat exchangers are a mix between welded plate and shell & tube designs. For the high pressure regime in the HRSG, where pressures exceed 40 bar, a WPHE design is not feasible so the HP ECO and the HP SH are constructed as shell and tube exchangers. The results of the improved cycle sensible heat exchangers are given in table 7.10. The results of the hydrogen and oxygen preheaters are not stated in the table since the results are nearly identical compared to the basic cycle.

Table 7.10: Heat exchanger design specifications for the improved cycle

Parameter	LP ECO	HP ECO	HP SH	LP SH1	LP SH2	Unit
	WPHE	S&T	S&T	WPHE	WPHE	
Q	91.9	83.4	112.1	166.5	199.9	m
U_0	116.8	52.7	10.4	52.7	84.4	$W(m^2^\circ C)^{-1}$
A	28.1	51.1	193.4	44.2	136.4	m ²
ΔT_{lm}	27.2	27.2	57.9	75.4	18.3	°C
ΔP_H	21.3	22.6	22.3	24.8	23.0	mbar
ΔP_C	0.001	0.001	0.03	0.13	3.6	mbar
V	0.08	0.4	1.5	0.16	0.46	m ³
β	340.9	125.9	132.6	278.8	296.6	m ² /m ³

7.4. Latent heat exchanger design

7.4.1. Condenser design

The condensing of steam occurs in the bottom cycle where the latent heat of the steam is extracted from the medium. The condenser is designed as a plate heat exchanger due to its advantages compared to the shell and tube alternative discussed in the previous chapter. The design of the condensing heat exchangers is carried out via the design steps from Sinnott & Towler [83] and Infante Ferreira [38][36], where the first design steps are identical compared to the ones already discussed in chapter 7.3. The geometry of the condenser is equal to that of the designed sensible plate heat exchangers, the difference is in condensing heat transfer coefficients and pressure drops in the condensed steam. The modified correlation developed by Shah gives the best approach for the condensing heat transfer coefficient and is stated in equation 7.9 [30] [38].

$$\alpha = 0.023 Re_L^{0.8} Pr_L^{0.4} \frac{\lambda_L}{d_e} \left[(1-x)^{0.8} + \frac{3.8x^{0.76}(1-x)^{0.04}}{P_{reduced}^{0.38}} \right] \quad (7.9)$$

The equation is a modified correlation of the condensation inside tubes where the coefficients are altered to fit the plate design of the exchanger. The Reynolds number Re_L is defined as Gd_e/μ_L , with d_e being twice the channel spacing and G being the mass velocity or mass flux in kg/m^2s . The condensate frictional pressure drop is defined similarly to single-phase flow pressure drops in equation 7.10, the difference is the two-phase flow friction factor f_{TP} for which many correlations are developed through the years.

$$\Delta P = 2f_{TP} \frac{G^2 L_p}{\rho_{av} d_e} \quad (7.10)$$

The used two-phase friction factor is the one developed by Infante Ferreira and Tao stated in Eq. 7.11, which is derived from experimental databases and proved to be a better correlation compared to existing correlations [38][30].

$$f_{TP} = (4.207 - 2.673\phi^{-0.46})(4200 - 5.41B_d^{1.2})Re_{eq}^{-0.95} \frac{P_{sat}}{P_c} \quad (7.11)$$

With B_d as the Bond number, indicating the ratio of buoyancy to surface tension and differentiates the micro- and macro scale during condensation [38]. To determine the two-phase friction factor f_{TP} , the equivalent Reynolds number Re_{eq} , the equivalent mass flux G_{eq} and the bond number Bd are calculated via the formulas stated in Eq. 7.12.

$$Re_{eq} = \frac{G_{eq}d_e}{\mu_L}, \quad G_{eq} = (1-x) + x \left(\frac{\rho_L}{\rho_G} \right)^{0.5}, \quad B_d = \frac{(\rho_L - \rho_G)gd_e^2}{\sigma} \quad (7.12)$$

Where x is the vapour quality set to an average of 0.5, σ being the surface tension in N/m and g the standard gravitational acceleration in m/s^2 . With the condensing heat transfer coefficient and frictional pressure drop correlation determined, the results of the condenser of the basic and improved cycle are presented in table 7.11 where ΔP_s and ΔP_{cw} represent the steam and cooling water pressure drop respectively.

Table 7.11: Welded plate condenser design specifications for both cycles

	Basic cycle	Improved cycle	Unit
Q	1288	1257	kW
U_0	1100	1097	$W(m^2\text{ }^\circ\text{C})^{-1}$
A	123	120.1	m^2
ΔT_{lm}	9.5	9.5	$^\circ\text{C}$
ΔP_s	15	16	Pa
ΔP_{cw}	73	73	Pa
V	0.29	0.29	m^3
β	421.2	421.3	m^2/m^3

7.4.2. Evaporator design

The evaporators in the basic and improved cycle transfer the required heat from the flue gas to the water/steam so that when the stream exits the evaporator, all of the liquid has evaporated and thus has a vapour fraction of 1. To do so, two designs of evaporators were made, the welded plate evaporator for low pressure regimes and a shell and tube evaporator for the high pressure regime in the improved cycle HRSG.

Welded plate evaporator design

The welded plate evaporator design is similar to that of the welded plate condenser and sensible WPHE designs, especially the first steps in the design procedure. The heat transfer correlations for evaporation differ from the condensing and sensible ones, together with the pressure drop calculated over the evaporated medium. The evaporation heat transfer correlation defined by Yan and Lin stated in equation 7.13 gives the best approach for equivalent Reynolds numbers between 2000 and 10000 [30].

$$\alpha = 1.926 Re_{eq} Pr_L^{0.3} Bo_{eq}^{0.3} Re_L^{-0.5} \left(\frac{\lambda_f}{d_e} \right) \quad (7.13)$$

With Bo_{eq} being the equivalent boiling number, indicating the non-dimensional heat flux stated in equation 7.14, with Δh being the latent heat.

$$Bo_{eq} = \frac{\dot{q}}{G_{eq} \Delta h} \quad (7.14)$$

The corresponding friction factor to determine the pressure drop is the one developed by Yan & Lin where the equivalent Reynolds number exceeds 6000 stated in equation 7.15[36].

$$f_{TP} = 31.21 Re_{eq}^{0.04557} Re^{-0.5} \quad (7.15)$$

After which the water/steam pressure drop can be determined via equation 7.10.

Shell & tube evaporator design

The operating conditions of the high pressure regime in the improved cycle HRSG require a shell & tube evaporator design due to the elevated operating pressure of approximately 45 bar. The design of the S&T evaporator is achieved according to the vaporiser design method presented in Sinnott & Towler [83]. The complex heat transfer phenomena of boiling a liquid is not discussed in this design process, only a brief explanation of the design method is given for a basic sufficient understanding of the workings of vaporisers. The forced convective boiling α_{cb} is determined via Chen's method and can be considered of the summation of a forced convective component α'_{fc} and a nucleate boiling component α'_{nb} stated in equation 7.16.

$$\alpha_{cb} = \alpha'_{fc} + \alpha'_{nb} \quad (7.16)$$

The convective boiling part α'_{fc} is estimated with the use of single phase forced convection heat transfer and multiplied with a correction factor f_c to account for the two-phase flow. The nucleate boiling coefficient α'_{nb} is calculated with the nucleate pool boiling correlation and a correction factor f_s to account for the boiling suppression factor. Equation 7.17 shows the two correlations with the corresponding correction factors for the convective and nucleate boiling coefficients.

$$\alpha'_{fc} = f_c \alpha_{fc} \quad , \quad \alpha'_{nb} = f_s \alpha_{nb} \quad (7.17)$$

The correction factors are found in found in tables in the literature and correspond to convective boiling enhancement factors ($1/X_{tt}$) and nucleate boiling suppression factors ($Re_L f_c^{1.25}$). The term $1/X_{tt}$ is the Lockhart-Martinelli two-phase turbulence flow parameter which is a function of density, vapour fraction and viscosity stated in equation 7.18.

$$\frac{1}{X_{tt}} = \left(\frac{x}{1-x} \right)^{0.9} \left(\frac{\rho_L}{\rho_v} \right)^{0.5} \left(\frac{\mu_v}{\mu_L} \right)^{0.1} \quad (7.18)$$

The nucleate boiling coefficient α_{nb} was determined via the correlation developed by Forster and Zuber which is a useful correlation that can be used to estimate pool boiling coefficients in the absence of experimental data [37][83].

$$\alpha_{nb} = 0.00122 \left[\frac{\lambda_L^{0.79} C p_L^{0.45} \rho_L^{0.49}}{\sigma^{0.5} \mu_L^{0.29} \Delta h^{0.24} \rho_G^{0.24}} \right] (T_w - T_s)^{0.24} (P_w - P_s)^{0.75} \quad (7.19)$$

The results of the evaporator sizing calculations are presented in table 7.12 for the basic and improved cycle.

Table 7.12: Evaporator design specifications for both cycles

Parameter	Basic cycle	Improved cycle		Unit
	WPHE	LP WPHE	HP S&T	
Q	648	137	393	kW
U_0	215	197	123	$W(m^2C)^{-1}$
A	41.9	26.2	59.3	m^2
ΔT_{lm}	77.4	26.2	50.9	$^{\circ}C$
ΔP_s	15	1	21.7	Pa
ΔP_{fg}	0.019	0.024	0.024	bar
V	0.1	0.07	1	m^3
β	422.2	361.1	57.5	m^2/m^3

7.5. Comparison with commercial equipment

This section compares, if possible, the designed components to commercially available equipment. Several of the components are not yet available and multiple years of research and development is required in order to actually built these components. For not yet available equipment, usually due to the use of 100% hydrogen as fuel, a comparison is made with commercially available equipment fuelled with natural gas.

Compressor

The compression of steam comes with several challenges, for the compressor to operate as efficient as possible, the inlet temperature needs to be as low as possible. This however results in temperatures close to saturation, which could result in condensation problems in the compressor and therefore, the temperature needs to be selected with caution. Steam compressors are frequently part of a mechanical vapour recompression (MVR) system and are built by manufacturers such as Howden and Piller [35][63]. Special care regarding material selection needs to be taken into account for the high operating temperatures of the compressor in the proposed cycles.

High Temperature Turbine

Pure hydrogen and oxygen fuelled gas turbines are not yet a possible solution. More and more research is conducted about increasing the hydrogen content in the fuel, with the goal of reaching a fully functional 100% hydrogen fired gas turbine. According to McCoy Power Report [64], the Original Equipment Manufacturer (OEM) most advanced in this field is General Electric with 75 gas turbines worldwide operating on fuels with higher hydrogen concentrations [64].

Opra turbines [85] is specialised in radial gas turbines operating in a wide range of power outputs. A collaboration between the OEM and Ansaldo Thomassen, Delft University of Technology, Vattenfall, Nouryon and EMMTEC is currently in progress to develop a hydrogen gas turbine retrofit with subsidy of the Dutch Government [10]. The similarities of this cooperation and the proposed cycles makes this a promising project to closely monitor.

Mitsubishi Power has successfully developed gas turbines capable of operating with hydrogen fuel concentrations of 30%, which is an important step in achieving the goal of a 100% H_2 fired GT [53]. Siemens Energy is somewhat further in its development and has reached hydrogen fuel concentrations of 40 to 60%. The company has set its targets on a project showcasing a future energy system with hydrogen turbines called "Zero Emission Hydrogen Turbine Center" [26]. With this program, Siemens aims to reach successful operation on 100% hydrogen fuel compositions in 2030.

When comparing commercially available turbine packages, operating within a comparable power range but fuelled with natural gas, the C600S (fig 7.15) developed by Capstone Green Energy [21] is a good alternative. The gas turbine system provides a power output of maximum 600 kW, which is comparable with the net power output from the HTT-Compressor shaft power output of the proposed cycles. The Capstone C600S has a total size of 3.0x5.8x3.0 m.

Low Pressure Turbine

Several condensing turbines are commercially available for the power range and operating pressure range of the LPT. An example is the MDT-300 developed by Turbonik [86] depicted in figure 7.16. With a maximum power output of 300 kW, low weight and small size, makes it a good fit for



Figure 7.15: The C600S Power Package developed by Capstone [21]

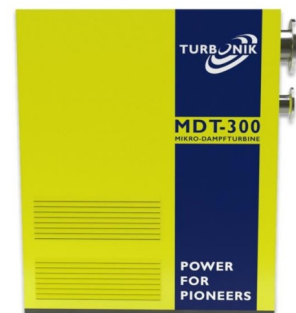


Figure 7.16: MDT-300 developed by Turbonik as suggested LPT [86]

the proposed power cycles. The dimensions of the LPT with casing are 1.80x2.20x0.80 m, accounting to a total volume of approximately 3.2 m^3 . A fine, but larger alternative for the Turbonik low pressure turbine is the Mitsubishi AT34C [52], the preferred option is, due to its size, the steam turbine developed by Turbonik [86].

Solid Oxide Fuel Cell

A cooperation between Cummings Inc. and Ceres Power Ltd. evaluated Microsoft's vision regarding fuel cell powered small scale data centers and developed a fuel cell demonstrator unit of the size 1.25x0.6x1.9 [93]. This demonstrator unit delivers 5 kW of power so when scaled to size, the total volume of the stack is significant. More research about implementing Ceres fuel cells on the 2 MWe power output size is required to get a better idea of the size of such a fuel cell system.

The world's first fuel cell system of approximately equal power outputs compared to that of the proposed SOFC is the 2 MWe fuel cell power plant project called DEMCOPEM [82]. It was constructed at the end of 2017 in Yingkou China consisting of low temperature PEM fuel cells developed by Nedstack, fuelled with high concentrations of hydrogen. The project was a cooperation between Nouryon, Nedstack, MTSA Technopower, JM and Politecnico milano. The total size of the 2 MWe fuel cell system is approximately 2.5 times the size of regular 20 ft shipping containers as can be seen in figure 7.17 developed by DEMCOPEM [82]. The companies involved claim that due to its modular design, the system could be scaled up to power outputs of 20 MWe.

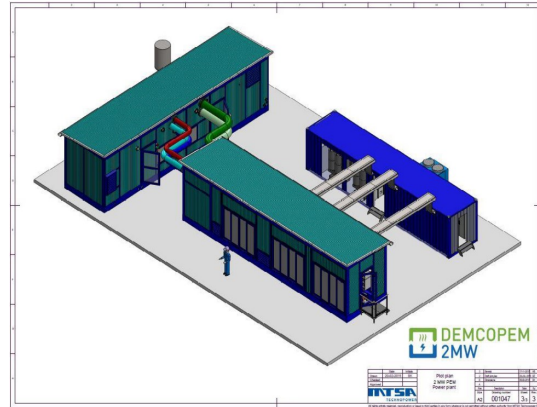


Figure 7.17: Lay-out of the DEMCOPEM 2 MWe PEM fuel cell system with human for scale [82]

7.5.1. Inland shipping application

The company Nedstack, that supplied the large fuel cell system for the DEMCOPEM project in China is also currently invested in the FELMAR [61] and WEVA [66] projects in the Netherlands. These projects focus on developing zero emission inland shipping vessels with the goal of reaching zero carbon emissions for all inland shipping vessels before 2050. The Dutch government invested 4 million euros in the projects, one of which is a vessel named "Antonie", depicted in figure 7.18 and is expected to be ready in 2023 [66]. The vessel with a length of 135m will transport cargo between the harbours of Rotterdam and Delfzijl, powered with a PEM fuel cell stack fuelled with 100% hydrogen [66].



Figure 7.18: The inland shipping vessel "Antonie", currently developed to be powered by a 100% hydrogen fuelled PEM fuel cell [66]

A downside of hydrogen powered vessels is the on board storage of the fuel. Hydrogen is less energy dense compared to the fuels used today. Furthermore, the storage tanks are expensive since they have to be able to withstand extremely low temperatures and high pressures. To get an idea about the fuel storage space, the required tank capacity was determined for a trip from Rotterdam to Basel, a trip of approximately 850 km for a 110 meter long inland shipping vessel with comparable power range of the proposed cycles. With the hydrogen being fully liquid, a storage tank with the capacity of approximately 57 m^3 is required for a one way trip. With a tank this size, a diesel powered inland shipping vessel could make almost three return trips. This is a direct result of the low liquid hydrogen

density of approximately 70 kg/m^3 , when compressed hydrogen in gaseous form is used, even larger tank sizes are required [92]. For a hydrogen tank with the capacity of 57 m^3 , an oxygen tank capacity of approximately 28 m^3 is needed, with the requirement that the oxygen is also cooled to its liquid form.

7.5.2. Preliminary size estimation of the basic cycle

With the preliminary component designs and comparison with commercial available equipment, a provisional estimation about the total volume of the cycle can be made. It is, at this stage, impossible to give an exact number of the final volume, only provisional estimations can therefore be made.

The largest part of the cycle is the fuel cell system, since only the approximate size of the stack was determined, the proven system built for the DEMCOPEM project is considered as more representative for a size estimation. This amounts to approximately 2.5 containers.

Since gas turbines operating on 100% hydrogen fuels are not yet developed, the size of the Capstone system is taken as alternative. The Capstone system consists of a high temperature turbine, compressor, generator, bearings, recuperator, combustion chamber and housing. The system comes in a package with a total volume of approximately 52 m^3 . For an indication of the LPT size, the dimensions of the MDT-300 developed by Turbonik [86] were used.

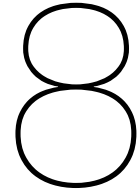
The volumes of the heat exchange equipment, determined in the design process only consists of the active heat transfer area of the components. Since only welded plate heat exchangers are equipped in the basic cycle, the total volume of the exchanger is expected not to differ much compared to the actual size of the exchanger. Nevertheless, a factor of 4 was used to account for additional piping and possible skids. The total heat exchange volume amounts to approximately 5 m^3 .

To get an idea about the size of the hydrogen storage tank, the design made by Kawasaki [41] is used. Kawasaki claims to have developed the largest spherical liquefied hydrogen storage tank in the world with a storage capacity of $10,000 \text{ m}^3$ with an outer diameter of 30m. These ratios were used to design a storage tank with the capacity of 57 m^3 , earlier discussed for a trip of 850 km. This comes down to a spherical tank with the total volume of approximately 80 m^3 , resulting in an outer tank diameter of 5.4m. For the oxygen storage tank, the same ratio was used, which results in a spherical tank with an outer diameter of 4.2m.

An overview of the estimated volumes of the cycle components are depicted in table 7.13. The SOFC integrated combined cycle, without the tank storage, has an estimated size of approximately 4.5 regular 20 ft shipping containers.

Table 7.13: Provisional size estimation of the components and cycle

Component	Value	Unit
SOFC system (DEMCOMPEM [82])	83.0	m^3
Gas turbine system (Capstone [21])	52.2	m^3
LPT [86]	3.2	m^3
Heat exchange equipment	5.0	m^3
Tank sizes	120	m^3
Total volume without tank storage	143	m^3
Total volume with tank storage	263	m^3



Conclusion & recommendations

8.1. Conclusion

The purpose of this research was to develop a small scale, zero carbon emission power cycle which could be used in the transport sector as power supply for the newly designed electrical inland shipping vessels. The important design criteria were simplicity and efficiency so that the cycle could be developed within a research and development time of approximately 10 to 20 years. Two hydrogen-oxygen power cycles were designed with the inclusion of a solid oxide fuel cell for direct electricity generation. The cycles were evaluated with an exergy analysis, from which became clear where the major losses in the cycle take place and showed where the potential for improvement lies.

The basic cycle can be summarised as a SOFC integrated combined Brayton-Rankine cycle where the SOFC is placed upstream of the combustion chamber and the two cycles are connected via a single pressure heat recovery steam generator. Power is extracted from the medium in three stages, the fuel cell converts the energy in the fuel directly into electricity and heat, where two turbines in the power cycle are coupled to generators to convert the mechanical energy into electrical energy. The fuel cell takes care of the largest part of the generated power, 80% of the hydrogen is converted in the SOFC stack, 20% of the supplied fuel is reacted in the combined cycle. The total generated power by the SOFC-combined cycle is 3016 kWe, where the fuel cell power amounts to 2184 kWe and the net power generated by the combined cycle is thus 832 kWe. The exergy analysis resulted in a total exergetic efficiency of 73.09% and showed that the major losses in the system were in the fuel cell, combustor and HRSG.

The second proposed cycle is an improvement on the basic cycle. From the basic cycle exergy analysis became clear that improvements for the HRSG could potentially result in a large efficiency increase. The improved cycle HRSG is therefore designed with an extra pressure regime, making it a dual pressure HRSG. With the high pressure regime, a high pressure turbine is added, creating an extra point in the cycle where useful power is extracted from the steam. The addition of the HP regime results in an efficiency increase of 0.74% for the HRSG alone, the extra work required by the pumps and compressor however have a negative effect on the performance, resulting in a total loss increase of 0.38% to 73.47% exergetic efficiency of the improved cycle. Such an improvement is a fine result for a large scale power plants, but of questionable advantage for a small scale power system of approximately 3 MWe. When considering both design criteria, simplicity and efficiency, the basic cycle is the preferred option for this power range since the extra complexity of the dual pressure HRSG of the improved cycle does not weigh up to the efficiency increase it provides.

The compressor, HTT and HPT are determined to be radial equipment, where the compressor is of the dual stage configuration and the turbines both single stage. This results in a compressor stage PR lower than 3, which implies that a shrouded and thus more efficient compressor can be used. The shaft speed of the compressor stages and HTT are matched so that the two components can be arranged on the same shaft with as result that the HTT drives the compressor and no external motor is required.

This resulted in a minimal decrease in maximum efficiency of the components but a more ideal design. The high pressure turbine is a typical radial micro steam turbine with a lower efficiency of approximately 70% compared to the other turbomachinery equipment. The preliminary design of the SOFC based on the design of Ceres Ltd. [45] resulted in eleven stacks of 200 kW with the size of 0.3 m^3 per stack, implying that the total combined volume of the stacks is 3.3 m^3 . What must be emphasised is that this is not the total size of the complete fuel cell system but only an indication about the stack size. The designed heat exchangers in the basic cycle are all of the welded plate and frame configuration due to their favourable high heat transfer coefficients and high area densities. Shell & Tube designs are only proposed for the operating conditions beyond the possible operating window of the welded plate and frame exchangers. This is only the case for the high pressure equipment of the improved cycle HRSG.

From the provisional size estimation of the components, the total system size was estimated to be approximately the size of 4.5 shipping containers. If the cycle would be installed in one of the newest inland shipping vessels, two spherical tanks with the capacity of 57 and 28 m^3 are required for the hydrogen and oxygen storage to make a single trip of 850 km.

8.2. Recommendations for future research

For future research, the following recommendations can and/or need to be investigated for further improvements of the cycle.

To reduce the compressor work, an intercooler should be implemented between compression stages. The use of the LPT inlet stream as cooling medium between compression stages will result in an efficiency increase on two levels. It has a positive effect since the inlet temperature of the LPT is raised, but more predominantly, the cooling between compression stages results in a significant decrease in the amount of required compression work. From an efficiency standpoint, this would be an improvement to the cycle, the cycle does however get more complicated due to the extra equipment.

For the turbomachinery design, the N_s-D_s relation and dependence on the optimum efficiency used were developed by Baljé. Although the diagrams developed by Baljé are relevant and consist of correct data, studies have shown that for low-Reynolds numbers, optimum efficiency ranges for radial turbomachinery deviate somewhat from the correlations developed by Baljé. For a more exact design of the low-Reynolds number radial turbomachinery, the data developed by Capata et al. [20] should be taken into account in future research.

In this research, several operating conditions of the solid oxide fuel cell such as the efficiency and fuel utilisation were fixed on beforehand with values taken from literature. For a better design of the SOFC, a parameter analysis should be conducted to determine the optimum operating conditions for increased power densities resulting in smaller stack sizes. The true size of the fuel cell system should be investigated as well to get a better idea of the feasibility of implementing the cycle in an inland shipping vessel.

The proposed cycles are designed for their maximum power output and operate thus at full load. The performances of the cycles should be investigated thoroughly for off design or part load operation to investigate if part load operation is still an attractive option or even a possibility.

When the time comes that all equipment in the cycle is commercially available, a new size estimation should be made in order to get a better idea about the options of implementing the system in an inland shipping vessel.

Finally, all decisions made in the process of this research were based on optimum designs regarding simplicity and efficiency, but a cost-benefit analysis has not been performed. Future research needs to take costs into account as well to determine if a power system is financially conceivable.

Bibliography

- [1] The National Oceanic Administration, Atmospheric, and U.S. Department of Commerce. CO2 levels during the last three glacial cycles, as reconstructed from ice cores. URL <https://climate.nasa.gov/vital-signs/carbon-dioxide/>.
- [2] Roberto Agromayor and Lars O Nord. Preliminary Design and Optimization of Axial Turbines Accounting for Diffuser Performance. *International Journal of Turbomachinery, Propulsion and Power*, 2019. doi: 10.3390/ijtpp4030032.
- [3] P. Aguiar, C. S. Adjiman, and N. P. Brandon. Anode-supported intermediate temperature direct internal reforming solid oxide fuel cell. I: Model-based steady-state performance. *Journal of Power Sources*, 138(1-2):120–136, 2004. ISSN 03787753. doi: 10.1016/j.jpowsour.2004.06.040.
- [4] A Ahmed, K Khodary Esmaeil, M. A. Irfan, and F. A. Al-mufadi. Design methodology of heat recovery steam generator in electric utility for waste heat recovery. (September):369–379, 2018. doi: 10.1093/ijlct/cty045.
- [5] Muhammad Akram, Jean-michel Bellas, and Karen N Finney. Making gas-CCS a commercial reality : The challenges of scaling up. *Greenhouse gas science and technology*, 24:1–24, 2017. doi: 10.1002/ghg.
- [6] C Al. Appendix 1: Standard Chemical Exergy. *Thermodynamics and the Destruction of Resources*, pages 489–494, 2011. doi: 10.1017/cbo9780511976049.024.
- [7] Abid Al-Rahman.H.AL-Hobo and Maher Saab.Salamah. Design Of Dual Pressure Heat Recovery Steam Generator For Combined Power Plants.
- [8] T. C. Allison, J. Moore, R. Pelton, J. Wilkes, and B. Ertas. *Fundamentals and Applications of Supercritical Carbon Dioxide (sCO₂) Based Power Cycles*. 2017. ISBN 9780081008058. doi: 10.1016/B978-0-08-100804-1.00007-4.
- [9] M Andersson and J Froitzheim. Technology review – Solid Oxide Cells 2019. *Swedish Electromobility Centre - Energiforsk*, 601, 2019.
- [10] Thomassen Ansaldo. Important subsidy paves way towards emission-free gas turbines, 2019.
- [11] P. V. Aravind. SOFCs- From cells to systems. *ME45100 Fuel Cell Systems (2018/19 Q4)*, pages 1–52, 2019.
- [12] A. Averberg, K. R. Meyer, C. Q. Nguyen, and A. Mertens. A survey of converter topologies for fuel cells in the kW range. *IEEE Energy 2030 Conference, ENERGY 2008*, (June), 2008. doi: 10.1109/ENERGY.2008.4781012.
- [13] Ballard. Fuel Cell applications for marine vessels. 2019.
- [14] S. Bastianoni, A. Facchini, L. Susani, and E. Tiezzi. Emergy as a function of exergy. *Energy*, 32(7):1158–1162, 2007. ISSN 03605442. doi: 10.1016/j.energy.2006.08.009.
- [15] N P Brandon, A Blake, D Corcoran, D Cumming, A Duckett, D Haigh, C Kidd, R Leah, G Lewis, C Matthews, N Maynard, N Oishi, T Mccolm, R Trezona, A Selcuk, M Schmidt, and L Verdugo. Development of Metal Supported Solid Oxide Fuel Cells for Operation at 500 – 600 C. *Journal of Fuel Cell Science and Technology*, 1(November 2004):61–65, 2019. doi: 10.1115/1.1794709.
- [16] Paul Breeze. Natural Gas-Fired Gas Turbine and Combined Cycle Power Plants. In *Power Generation Technologies*, pages 71–97. 2019. ISBN 9780081026311. doi: 10.1016/b978-0-08-102631-1.00004-3.

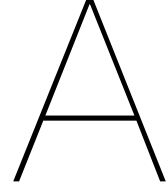
- [17] Cleverson. Bringhenti, Jesuino Takachi. Tomita, and Joao Roberto. Barbosa. Performance Study of a 1 MW Gas Turbine Using Variable Geometry Compressor and Turbine Blade Cooling. 2010.
- [18] F. Calise, M. Dentice d'Accadia, A. Palombo, and L. Vanoli. Simulation and exergy analysis of a hybrid Solid Oxide Fuel Cell (SOFC)-Gas Turbine System. *Energy*, 31(15):3278–3299, 2006. ISSN 03605442. doi: 10.1016/j.energy.2006.03.006.
- [19] Stefano Campanari, Luca Mastropasqua, Matteo Gazzani, Paolo Chiesa, and Matteo C. Romano. Predicting the ultimate potential of natural gas SOFC power cycles with CO₂ capture – Part A: Methodology and reference cases. *Journal of Power Sources*, 324:598–614, 2016. ISSN 03787753. doi: 10.1016/j.jpowsour.2016.05.104. URL <http://dx.doi.org/10.1016/j.jpowsour.2016.05.104>.
- [20] Roberto Capata and Enrico Sciubba. Experimental Fitting of the Re-Scaled Balje Maps for Low-Reynolds Radial Turbomachinery. *Energies*, (July), 2015. doi: 10.3390/en8087986.
- [21] Capstone. C600S Power Package, High-pressure Natural Gas - Technical datasheet.
- [22] Macinac center for public Policy. Electricity in Michigan: A Primer.
- [23] H Cohen, GFC Rogers, and HIH Saravanamuttoo. *Gas Turbine Theory*. 1996.
- [24] Ibrahim Dincer and Marc A. Rosen. Exergy - Energy, Environment and Sustainable Development - Chapter 3: Chemical exergy. In *Exergy*, pages 37–60. 2021. ISBN 9780128243725. doi: 10.1016/b978-0-12-824372-5.00003-8.
- [25] H Ekker. 2020 warmste jaar ooit gemeten in Europa, grootste afwijking bij Siberië en Noordpool, 2021.
- [26] Siemens Energy. Zero Emission Hydrogen Turbine Center, 2021. URL <https://www.siemens-energy.com/global/en/priorities/future-technologies/hydrogen/zehtc.html>.
- [27] U.S. Department of Energy Energy efficiency Energy and Renewable. Comparison of Fuel Cell Technologies. Technical report, 2016.
- [28] European Union. Hydrogen roadmap Europe - A sustainable pathway for the European energy transition. Technical report, 2019.
- [29] M. Gandiglio, A. Lanzini, P. Leone, M. Santarelli, and R. Borchiellini. Thermo-economic analysis of large solid oxide fuel cell plants: Atmospheric vs. pressurized performance. *Energy*, 55:142–155, 2013. ISSN 03605442. doi: 10.1016/j.energy.2013.03.059. URL <http://dx.doi.org/10.1016/j.energy.2013.03.059>.
- [30] J. R. García-Cascales, F. Vera-García, J. M. Corberán-Salvador, and J. González-Maciá. Assessment of boiling and condensation heat transfer correlations in the modelling of plate heat exchangers. *International Journal of Refrigeration*, 30(6):1029–1041, 2007. ISSN 01407007. doi: 10.1016/j.ijrefrig.2007.01.004.
- [31] Andrzej Gardzilewicz. Wet steam flow in the turbines - The Baumann rule of losses still in force. *Institute of Fluid-Flow Machinery, PAS, Gdansk*, (December), 2017.
- [32] General Electric and Electricite de France. GE and EDF unveil a game-changer at Bouchain: a 62.22 percent efficiency rating for a combined-cycle power plant has never been achieved before, 2016.
- [33] K. Hassmann. SOFC Power Plants, the Siemens-Westinghouse Approach. *Fuel Cells*, 1(1):78–84, 2001. ISSN 1615-6846. doi: 10.1002/1615-6854(200105)1:1<78::aid-fuce78>3.0.co;2-q.
- [34] R Holyst and A Poniewierski. *Thermodynamics for Chemists, Physicists and Engineers*. 2012. ISBN 9789400729988.

- [35] Howden. Howden compressor technologies - brochure, 2021.
- [36] Carlos A Infante Ferreira. ME45165 - Equipment for heat transfer - Plate heat exchangers. *Equipment for Heat and Mass transfer*, pages 1–58, 2020.
- [37] Carlos A Infante Ferreira. ME45165 - Equipment for heat transfer - Condensation and evaporation in tubes. *Equipment for Heat and Mass transfer*, pages 1–33, 2020.
- [38] Carlos A Infante Ferreira and Xuan Tao. Heat transfer and frictional pressure drop during condensation in plate heat exchangers : Assessment of correlations and a new method. *International Journal of Heat and Mass Transfer*, 135:996–1012, 2019. ISSN 0017-9310. doi: 10.1016/j.ijheatmasstransfer.2019.01.132. URL <https://doi.org/10.1016/j.ijheatmasstransfer.2019.01.132>.
- [39] Herbert Jericha and Morteza Fesharaki. The Graz cycle - 1500 C Max Temperature potential H₂-O₂ fired CO₂ capture with CH₄-O₂ firing. *ASME Cogen-Turbo Power Conference*, (August), 1995.
- [40] Herbert Jericha, Wolfgang Sanz, Jakob Woisetschläger, and Morteza Fesharaki. CO₂ - Retention Capapility of CH₄/O₂ - Fired Graz Cycle. *Cimac*, pages 1–13, 1995.
- [41] Kawasaki. Kawasaki completes basic design for worlds largest class (11,200-cubic meter) sperical liquefied hydrogen storage tank, 2020. URL https://global.kawasaki.com/en/corp/newsroom/news/detail/?f=20201224_8018.
- [42] Kelvion. HIGH PERFORMANCE MODEST SPACE REQUIREMENTS.
- [43] James Larminie and Andrew Dicks. *Fuel Cell Systems Explained*. 2003. ISBN 047084857X.
- [44] F. Laurencelle, R. Chahine, J. Hamelin, K. Agbossou, M. Fournier, T.K. Bose, and A. Laperriere. Characterization of a Ballard MK5-E Proton Exchange Membrane fuel cell stack. *Fuel Cells: From Fundamentals to Systems*, pages 66–71, 2001. ISSN 00207462. doi: 10.1016/S0360-3199(01)00020-9.
- [45] R T Leah, N P Brandon, and P Aguiar. Modelling of cells, stacks and systems based around metal-supported planar IT-SOFC cells with CGO electrolytes operating at 500 – 600 C. *Journal of Power Sources*, 145:336–352, 2005. doi: 10.1016/j.jpowsour.2004.12.067.
- [46] Jekyoung Lee, Jeong Ik, Yoonhan Ahn, and Seong Gu. Conceptual Design of Supercritical CO₂ Brayton Cycle Radial Turbomachinery for SMART Application. *Korean Nuclear Society*, 1(1):25–26, 2012.
- [47] R.I. Lewis. *Turbomachinery performance analysis*. Elsevier Science and Technology Books, 1996. ISBN 0340631910.
- [48] Bruce E. Logan. Fuel Cells, electrochemical conversion. *Fuel Cells: Technologies for Fuel Processing*, pages 1–32, 2009.
- [49] W.L. Lundberg, R.A. Holmes, J.E. King, G.A. Israelson, P.R. Zafred, R.E. Kothmann, R.R. Moritz, and S.E. Veyo. Pressurized Solid Oxide Fuel Cell/ Gas Turbine Power System. Technical report, 2000. URL <http://www.osti.gov/scitech/servlets/purl/772401/>.
- [50] Jaroslaw Milewski. Hydrogen utilization by steam turbine cycles. *Journal of Power Technologies*, 95(4):258–264, 2015. ISSN 2083-4195.
- [51] Jaroslaw Milewski, Krzysztof Badyda, and Andrzej Miller. Chapter 5: Gas Turbines in Unconventional Applications. Number April, pages 121–164. 2012. doi: 10.5772/37321.
- [52] Mitsubishi Heavy Industries Marine Machinery and Equipment. Mitshubishi Product information - Steam Turbine Generators (AT-Type AT34C).
- [53] Ltd. Mitsubishi Power and Mitsubishi Heavy Industries Group. Hydrogen power generation handbook, 2021.

- [54] C. Mitsugi, A. Harumi, and F. Kenzo. WE-NET: Japanese hydrogen program. *International Journal of Hydrogen Energy*, 23(3):159–165, 1998. ISSN 03603199. doi: 10.1016/S0360-3199(97)00042-6.
- [55] M. J. Moran, H. N. Shapiro, D. D. Boettner, and M. B. Bailey. *Fundamentals of Engineering Thermodynamics*. Number 8. 2014. ISBN 9781118412930.
- [56] Toshihiko Nakata, Diego Silva Herran, and Mikhail Rodionov. Application of energy system models for designing a low-carbon society. *Progress in Energy and Combustion Science*, (August):463 – 498, 2011. doi: 10.1016/j.pecs.2010.08.001.
- [57] Hossein Nami, Faramarz Ranjbar, and Mohsen Yari. Thermodynamic analysis of a modified oxy-fuel cycle , high steam content Graz cycle with a dual-pressure heat recovery steam generator. *Int. J. Exergy*, 21(3), 2016.
- [58] R. G. Narula, D. Koza, and H. Wen. *Impacts of steam conditions on plant materials and operation in ultra-supercritical coal power plants*. Woodhead Publishing Limited, 2013. ISBN 9780857091161. doi: 10.1533/9780857097514.1.23. URL <http://dx.doi.org/10.1533/9780857097514.1.23>.
- [59] Peter O’Kelly. *Computer simulation of thermal plant operations*. Springer, 2013. ISBN 9781461442554. doi: 10.1007/978-1-4614-4256-1.
- [60] H. Ouwerkerk. *Development of a 1MWe RCG-unit*. PhD thesis, 2009. URL <https://research.tue.nl/en/publications/development-of-a-1mwe-rcg-unit>.
- [61] Alles over Waterstof. Project FELMAR boekt vorderingen met ontwikkeling brandstofcel voor schepen, 2021. URL <https://allesoverwaterstof.nl/project-felmar-boekt-vordering-met-ontwikkeling-brandstofcel-voor-schepen/>.
- [62] Sung Ho Park, Young Duk Lee, and Kook Young Ahn. Performance analysis of an SOFC/HCCI engine hybrid system: System simulation and thermo-economic comparison. *International Journal of Hydrogen Energy*, 39(4):1799–1810, 2014. ISSN 03603199. doi: 10.1016/j.ijhydene.2013.10.171. URL <http://dx.doi.org/10.1016/j.ijhydene.2013.10.171>.
- [63] Piller. Blowers and compressors - brochure, 2021.
- [64] General Electric Gas Power. Hydrogen fueled gas turbines, 2021. URL <https://www.ge.com/gas-power/future-of-energy/hydrogen-fueled-gas-turbines>.
- [65] B. V. Reddy and Khaled Mohamed. Exergy analysis of a natural gas fired combined cycle power generation unit. *International Journal of Exergy*, 4(2):180–196, 2007. ISSN 17428300. doi: 10.1504/IJEX.2007.012065.
- [66] Nederlandse Particuliere Rijnvaart and K De Vries. Waterstof-Elektrisch Vrachtschip Antonie.
- [67] Rory Roberts, Jack Brouwer, Faryar Jabbari, Tobias Junker, and Hossein Ghezal-Ayagh. Control design of an atmospheric solid oxide fuel cell/gas turbine hybrid system: Variable versus fixed speed gas turbine operation. *Journal of Power Sources*, 161(1):484–491, 2006. ISSN 03787753. doi: 10.1016/j.jpowsour.2006.03.059.
- [68] Masoud Rokni. Thermodynamic analysis of an integrated solid oxide fuel cell cycle with a rankine cycle. *Energy Conversion and Management*, 51(12):2724–2732, 2010. ISSN 01968904. doi: 10.1016/j.enconman.2010.06.008. URL <http://dx.doi.org/10.1016/j.enconman.2010.06.008>.
- [69] M. R. Sandberg. Centrifugal Compressor Configuration, Selection and Arrangement: A Users Perspective. *Proceedings of the Forty-Fifth Turbomachinery Symposium*, pages 1–44, 2016.

- [70] Benjamin D. Santer, Céline J.W. Bonfils, Qiang Fu, John C. Fyfe, Gabriele C. Hegerl, Carl Mears, Jeffrey F. Painter, Stephen Po-Chedley, Frank J. Wentz, Mark D. Zelinka, and Cheng Zhi Zou. Celebrating the anniversary of three key events in climate change science. *Nature Climate Change*, 9(3):180–182, 2019. ISSN 17586798. doi: 10.1038/s41558-019-0424-x. URL <http://dx.doi.org/10.1038/s41558-019-0424-x>.
- [71] Wolfgang Sanz, M. Braun, Herbert Jericha, and M. F. Platzer. Adapting the zero-emission Graz Cycle for hydrogen combustion and investigation of its part load behavior. *International Journal of Hydrogen Energy*, 43(11):5737–5746, 2018. ISSN 0360-3199. doi: 10.1016/j.ijhydene.2018.01.162. URL <https://doi.org/10.1016/j.ijhydene.2018.01.162>.
- [72] Bram Schouten. Thermal efficiency improvement of closed hydrogen and oxygen fuelled combined cycle power plants with the application of solid oxide fuel cells using an exergy analysis method. Technical report, 2020.
- [73] Bram Schouten and Sikke Klein. Hydrogen and oxygen fired turbine cycle optimization. *ASME Turbo Expo 2020*, (June), 2020.
- [74] Eds. Shen, V.K., Siderius, D.W., Krekelberg, W.P., and Hatch, H.W. NIST Standard Reference Simulation Website.
- [75] J. M. Smith, H. C. Van Ness, M. M. Abbott, and M. T. Swihart. *Introduction to chemical engineering thermodynamics*. Number 8. 2018. ISBN 9781259696527.
- [76] Robin Smith. *Chemical Process Design and Integration*. John Wiley and Sons, Ltd, 2005. ISBN 0471486809.
- [77] Sondex. Plate and Shell Wärmtewisselaars (SPS) - Technische specificaties, 2021.
- [78] James M. Sorokes. Selecting a centrifugal compressor. *Chemical Engineering Progress*, 109(6): 44–51, 2013. ISSN 03607275.
- [79] Stella Spazzoli. Supercritical CO₂ Power Cycle for Solar Applications - Thermodynamic analysis and 1D turbomachinery design. Technical report, 2016.
- [80] A Boudghene Stambouli and E Traversa. Solid oxide fuel cells (SOFCs): a review of an environmentally clean and efficient source of energy. *Renewable and Sustainable energy reviews*, 6: 433–455, 2002.
- [81] NVRSS Subrahmanyam, S. Rajaram, and N. Kamalanathan. HRSGs for combined cycle power plants. *Heat Recovery Systems and CHP*, 15(2):155–161, 1995. ISSN 08904332. doi: 10.1016/0890-4332(95)90022-5.
- [82] MTSA Technopower and Nedstack Fuel Cell Technology. Industrial demonstration project 2 MW PEM fuel cell generator - Description and results of the DEMCOPEM project. *International Hydrogen Energy and Fuel Cell technology and product Expo in Foshan, China*, 2018.
- [83] G Towler and R Sinnott. *Chemical Engineering Design - Principles, practice and economics of plant and process design*. 2008. ISBN 9780750684231.
- [84] V Tsourapas, J Sun, and A Stefanopoulou. Incremental Step Reference Governor for Load Conditioning of Hybrid Fuel Cell and Gas Turbine Power Plants. *American Control Conference*, (June 2014):2184 – 2189, 2008. doi: 10.1109/TCST.2008.2010554.
- [85] Opra Turbines. Future Energy Landscape - Hydrogen combustion technology - OP16 gas turbine, 2021. URL <https://www.opraturbines.com/hydrogen-a-key-element-for-the-energy-transition/>.
- [86] Turbonik and Fraunhofer Institute UMSICHT. MDT-300 Technische daten, 2021.
- [87] UNFCCC. Kyoto Protocol to the United Nations Framework Convention On Climate Change. pages 1–24, 1997.

- [88] United Nations. Paris agreement, 2015.
- [89] Vahterus. Plate and Shell Heat Exchanger Technology - Design and Technical Sheet, 2021.
- [90] L. van Biert, T. Woudstra, M. Godjevac, K. Visser, and P. V. Aravind. A thermodynamic comparison of solid oxide fuel cell-combined cycles. *Journal of Power Sources*, 397(June):382–396, 2018. ISSN 03787753. doi: 10.1016/j.jpowsour.2018.07.035.
- [91] J. P. Van Buijtenen, W. Visser, T. Tinga, S. Shakariyants, and F. Montella. *Gas Turbines*. 2007.
- [92] Wouter van der Geest and Menno Menist. Op weg naar een klimaatneutrale binnenvaart per 2050, Transitie- en rekenmodel binnenvaart. *Panteia - Research to Progress*, (Juli):1–66, 2019.
- [93] Charles Cummins Inc Veseley and Bal Ceres Power Ltd Dosanjh. Metal-supported ceria electrolyte-based SOFC stack for scalable, low cost, high efficiency and robust stationary power systems. (June):1–23, 2018.
- [94] Michael M. Whiston, William O. Collinge, Melissa M. Bilec, and Laura A. Schaefer. Exergy and economic comparison between kW-scale hybrid and stand-alone solid oxide fuel cell systems. *Journal of Power Sources*, 353:152–166, 2017. ISSN 03787753. doi: 10.1016/j.jpowsour.2017.03.113. URL <http://dx.doi.org/10.1016/j.jpowsour.2017.03.113>.
- [95] N. Woudstra. *Sustainable energy systems. Limitations and challenges based on exergy analysis*. 2012. ISBN 9789461914415.
- [96] N. Woudstra, T. Woudstra, A. Pirone, and T. van der Stelt. Thermodynamic evaluation of combined cycle plants. *Energy Conversion and Management*, 51(5):1099–1110, 2010. ISSN 01968904.



Mathematical derivations

A.1. Enthalpy & entropy change of the reaction

The Gibbs Free Energy of the overall reaction (ΔG_r) at given temperature and pressure is calculated via Eq. A.1, earlier briefly discussed for the maximum efficiency of the fuel cell (Eq. 3.4).

$$\Delta G_r = \Delta H_r - T\Delta S_r \quad (\text{A.1})$$

The standard heat of a chemical reaction can be determined via the heats of formation from the products and reactants and vice versa. The standard enthalpy or heat of formation ΔH_f^o of a substance is specified as the enthalpy change when a single mole of the substance is formed from its constituent elements in the standard state, where the enthalpy of formation is zero for elements. The relation between the standard heats of reaction and formation are stated in equation A.2 [83]. The standard entropy of the reaction ΔS_r^o is found via an equal approach and stated in equation A.3.

$$\Delta H_r^o = \sum \Delta H_{f,products}^o - \sum \Delta H_{f,reactants}^o \quad (\text{A.2})$$

$$\Delta S_r^o = \sum \Delta S_{f,products}^o - \sum \Delta S_{f,reactants}^o \quad (\text{A.3})$$

The specific overall chemical reaction taking place in the Solid Oxide Fuel Cell and taking into account the stoichiometrics of the reaction results in equation A.4 for the standard enthalpy of reaction and equation A.5 for the standard entropy of reaction.

$$\Delta H_r^o = \Delta H_{f,H_2O}^o - \Delta H_{f,H_2}^o - \frac{1}{2}\Delta H_{f,O_2}^o \quad (\text{A.4})$$

$$\Delta S_r^o = \Delta S_{f,H_2O}^o - \Delta S_{f,H_2}^o - \frac{1}{2}\Delta S_{f,O_2}^o \quad (\text{A.5})$$

Values for the standard enthalpy and entropy of formation are found in thermodynamic databases from the National Institute of Standards and Technology (NIST) [74]. Table A.1 shows the corresponding constants together with the standard enthalpies and Gibbs energies of formation in kJ/mol , according to Smith, Van Ness & Abbott [75]. When a chemical reaction occurs in any other environment other than the standard conditions, extra steps need to be made to calculate the specified entropy and enthalpy of formation. Equation A.6 shows how the specified enthalpy is defined, equation A.7 shows how the specified entropy is calculated where the subscript i implies H_2 , O_2 or H_2O .

$$\Delta H_{f,i} = \Delta H_{f,i}^o + \int_{298}^T C_{p,i} dT \quad (\text{A.6})$$

$$\Delta S_{f,i} = \Delta S_{f,i}^o + \int_{298}^T \frac{C_{p,i}}{T} dT \quad (\text{A.7})$$

The heat capacity at constant pressure is determined via empirical expressions of ideal gasses according to Smith, Van Ness & Abbott [75]. Under certain circumstances, steam can be considered an ideal gas, this is further elaborated in appendix A.2.

Table A.1: Heat capacity constants, standard enthalpies & Gibbs energies of formation of the gasses in the ideal-gas state

Substance	A	10 ³ B	C	10 ⁻⁵ D	ΔH_f^o , kJ/mol	ΔG_f^o , kJ/mol
H ₂	3.249	0.422	0	0.083	0	0
O ₂	3.639	0.506	0	-0.227	0	0
H ₂ O	3.470	1.450	0	0.121	-241.818	-228.572

A.2. Ideal gas use verification

The temperature dependence of the heat capacity is a combination of the two simple expressions of practical values.

$$\frac{C_p^{ig}}{R} = \alpha + \beta T + \gamma T^2 \quad \text{and} \quad \frac{C_p^{ig}}{R} = a + bT + \frac{c}{T^2}$$

Where α , β , γ , a , b and c are constants depending on the substance. The combined expression of these empirical heat capacity definitions is used in this research and shown in equation A.8 [75].

$$C_p^{ig} = R \left(A + BT + CT^2 + \frac{D}{T^2} \right) \quad (\text{A.8})$$

The analytically expressed temperature dependence of the heat capacity at constant pressure (Eq A.8) does not take the pressure elevation into account on which the fuel cell will be operating and thus regards the steam as an ideal gas. Although ideal-gas-state heat capacities are strictly only correct for real gasses at zero pressure, it is rarely significant at pressures below several bars. The question is whether or not the operating conditions deviate too much so that the steam cannot be treated as an ideal gas, for this dilemma, figure A.1 comes into play. According to Smith, Van Ness & Abbott, it is a reasonable approximation to consider a real gas as an ideal gas when the first coefficient of the compressibility factor Z^0 lies between 0.98 and 1.02. Calculating the reduced pressure p_{red} and reduced temperature T_{red} of the steam at operating conditions of the Fuel cell with equations A.9 and A.10 respectively.

$$p_{red} = \frac{p}{p_c} \quad (\text{A.9})$$

$$T_{red} = \frac{T}{T_c} \quad (\text{A.10})$$

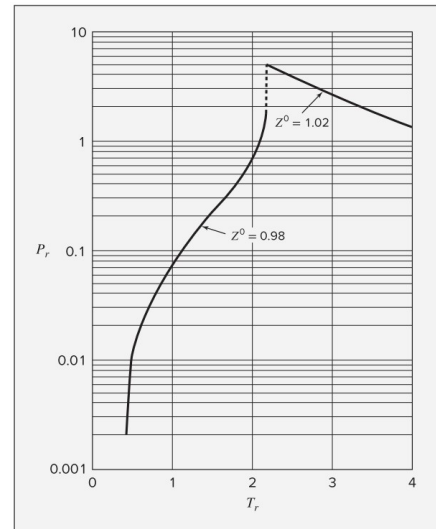


Figure A.1: The graphical relation between Z^0 , p_r and T_r [75]

Results in Z^0 of 0.99 using appendix D from Smith, Van Ness & Abbott [75]. The use of C_p^{ig} is therefore a validated choice to use instead of the real gas heat capacity.

A.3. Shell & Tube heat exchanger design steps continued

Step 6: Decide type, tube size, material layout and fluid sides

The following step in the design procedure is to determine the layout of the exchanger. Tube sizes, material layout and the division for the shell and tube side fluids. Normally, the most fouling fluid is sent through the tubes due to easier cleaning options but since all the fluids in the cycle are either pure gasses, clean steam or water, fouling does not play a large role in this cycle. The decision was therefore taken regarding the maximum allowable pressure drops from chapters 5 and 6 of the fluids on the tube and shell side, elaborated further in step 12. The tube configuration is chosen to be triangular for a more space efficient design regarding its alternatives square and rotated square. The triangular configuration is more difficult to clean, but since fouling does not play an important role, triangular is the best tube layout. The tube material is a carbon steel that can withstand the maximum temperature of 560 °C. The tube dimensions and number of passes are selected such that the pressure drop on the tube and shell side of the exchanger are within the limits of the designed cycle in Thermoflex.

Step 7: Calculate number of tubes

The number of tubes N_t is determined by dividing the total area of the exchanger by the area of a single tube A_t with the dimensions specified in step 6 (Eq. A.11).

$$N_t = \frac{A}{A_t} \quad \text{with} \quad A_t = d_o \pi L \quad (\text{A.11})$$

With D_o being the outside diameter and L the length of the tubes. The cross sectional area of the tubes is defined as the cross sectional area of a single tube times the number of tubes per pass. The number of tube passes depends on the type of exchanger, a single tube pass is the preferred design to minimise the tube fluid pressure drop. The tube side velocity u_t is defined as the volumetric flow rate \dot{V} through the tubes over the area per pass A_{pp} , resulting in equation A.12.

$$u_t = \frac{\dot{V}_t}{A_{pp}} \quad \text{with} \quad \dot{V}_t = \frac{\dot{m}_t}{\rho_{t,m}} \quad \text{and} \quad A_{pp} = N_p A_c \quad (\text{A.12})$$

Step 8: Calculate bundle and shell diameter

The bundle diameter depends on the number of tubes, tube passes and configuration of the tubes. In order to estimate the bundle diameter D_b , constants K_1 and n_1 are used that are derived from standard tube layouts. Equation A.13 states the empirical relation between the outer diameter, number of tubes and constants.

$$d_b = d_o \left(\frac{N_t}{K_1} \right)^{\frac{1}{n_1}} \quad (\text{A.13})$$

The inside shell diameter d_s will be a bit larger than the bundle diameter, the space between the tube bundle and inside shell is referred to as the clearance, the clearance depends on the type of exchanger and bundle diameter and is selected via typical values stated in Sinnott & Towler [83].

Step 9: Calculate tube side heat transfer coefficient

To determine the inside (tube side) heat transfer coefficient h_t , the Reynolds number must be calculated to determine if the flow is laminar or turbulent via Eq. A.14. The Prandtl number defines the ratio of momentum diffusivity to thermal diffusivity with Eq. A.15.

$$Re_t = \frac{\rho_{t,m} u_t d_i}{\mu_{t,m}} \quad (\text{A.14})$$

$$Pr_t = \frac{C_p \rho_{t,m} \mu_{t,m}}{\lambda_{f,t,m}} \quad (\text{A.15})$$

Where the subscript m states the mean value between inlet and outlet of the corresponding stream, subscript t refers to the tube side and $\lambda_{f,m}$ the mean thermal conductivity of the medium. A heat transfer factor j_h is used to determine the Nusselt number. Kern's method states that for turbulent ($Re_t > 2000$),

the ratio of convective to conductive heat transfer can be stated as equation A.16 and for laminar flow ($Re_t < 2000$) statement A.17 must be used.

$$Nu_{t,t} = j_{h,t} Re_t Pr_t^{\frac{1}{3}} \left(\frac{\mu_{t,m}}{\mu_{t,w}} \right)^{0.14} \quad (\text{A.16})$$

$$Nu_{t,l} = 1.86 (Re_t Pr_t)^{\frac{1}{3}} \left(\frac{d_i}{L} \right)^{\frac{1}{3}} \left(\frac{\mu_{t,m}}{\mu_{t,w}} \right)^{0.14} \quad (\text{A.17})$$

Where the mean medium viscosity μ_m is considered equal to the medium viscosity at the tube wall μ_w , implying that the viscosity term is eliminated from both the turbulent and laminar Nusselt equations. With the dimensionless numbers determined, the inside tube fluid film coefficient α_t can be calculated via equation A.18 in $W/(m^2 \cdot C)$.

$$\alpha_t = Nu_t \frac{\lambda_{f,t,m}}{d_i} \quad (\text{A.18})$$

Step 10: Calculate shell side heat transfer coefficient

The shell side heat transfer coefficient α_s is again calculated using the Kern's method based on experimental work on commercial heat exchangers and standard designs. The shell side parameters are correlated in a similar manner to those of the tube side but now using a hypothetical shell diameter and velocity. Since the cross-sectional area of the shell side flow varies across the shell diameter, the velocity is taken to be at the shell equator, indicating maximum area for cross flow. The shell equivalent diameter d_e is calculated for the area parallel to the tubes (axial direction) and the wetted perimeter of the tubes and is thus dependent on the tube arrangement. The cross flow area A_s for the hypothetical row of tubes at the shell equator is given by Eq. A.19.

$$A_s = \frac{(p_t - d_o) d_s l_b}{p_t} \quad \text{with} \quad p_t = 1.25 d_o \quad (\text{A.19})$$

With p_t being the tube pitch distance and l_b the baffle spacing both in meters. The shell side mass velocity G_s and the linear velocity u_s are determined via equation A.20 and A.21 respectively.

$$G_s = \frac{\dot{m}_s}{A_s} \quad (\text{A.20})$$

$$u_s = \frac{G_s}{\rho_{s,m}} \quad (\text{A.21})$$

With \dot{m}_s being the shell side mass flow rate in kilograms per second. The shell side hydraulic (equivalent) diameter depends on the tube arrangement of the bundle, since an equilateral triangular pitch is used for maximum heat transfer, d_e is expressed as equation A.22

$$d_e = \frac{4 \left(0.87 \frac{p_t^2}{2} - \frac{1}{2} \pi \frac{d_o^2}{4} \right)}{\frac{\pi d_o}{2}} = \frac{1.10}{d_o} (p_t^2 - 0.917 d_o^2) \quad (\text{A.22})$$

Now that the linear shell velocity and the equivalent diameter are determined, the shell side Reynolds and Prandtl number can be calculated via equation A.23 and A.24 respectively.

$$Re_s = \frac{\rho_{s,m} u_s d_e}{\mu_{s,m}} \quad (\text{A.23})$$

$$Pr_s = \frac{C p_{s,m} \mu_{s,m}}{\lambda_{f,s,m}} \quad (\text{A.24})$$

The shell side heat transfer coefficient can now be determined with equation A.25 in $W/(m^2 \cdot C)$.

$$\alpha_s = \left(\frac{\lambda_{f,s,m}}{d_e} \right) j_{h,s} Re_s Pr_s^{\frac{1}{3}} \quad (\text{A.25})$$

Where the shell side heat transfer factor $j_{h,s}$ can be found in figures depending on the shell side Reynolds number and the baffle cut percentage from Sinnott & Towler [83].

Step 11: Calculate overall coefficient U_0

The overall coefficient U_0 can be determined after the correct inside α_{id} and outside α_{od} dirt coefficients are selected from tables from Sinnott & Towler. The overall coefficient is the summation of the individual resistances to heat transfer, which is the reciprocal of the overall resistance. For shell and tube heat exchangers, the overall coefficient is determined via equation A.26.

$$U_0 = \left[\frac{1}{\alpha_s} + \frac{1}{\alpha_{od}} + \frac{d_o \ln\left(\frac{d_o}{d_i}\right)}{2\lambda_w} + \frac{d_o}{d_i} \frac{1}{\alpha_{id}} + \frac{d_o}{d_i} \frac{1}{\alpha_t} \right]^{-1} \quad (\text{A.26})$$

With k_w being the thermal conductivity of the tube wall material in $W/(m^2\text{ }^\circ\text{C})$. Now that the overall coefficient is known, the assumed overall coefficient from the literature in step 3 must be validated. When the assumed and the calculated value differ are not within the proximity stated in equation A.27, changes in the design procedures must be made from step 5 and further.

$$0 < \frac{U_0 - U_{0,ass}}{U_{0,ass}} < 10\% \quad (\text{A.27})$$

The closer the validation approaches zero, the better the design of the heat exchanger.

Step 12: Calculate shell & tube side pressure drops

The pressure drops on the shell and tube side are determined with friction factors $j_{f,s}$ and $j_{f,t}$ from the literature together with the calculated exchanger geometries, velocities and medium densities. The pressure drop across the inlet and outlet nozzles are assumed to be 15% of the total pressure losses and are included in the total shell and tube side pressure drops. The major sources of the tube side pressure drop are friction losses and sudden contraction and extractions the medium experiences by flowing through the pipes. The friction loss can be calculated using well known equations, but a combined equation developed for both loss contributions is not yet fully satisfactory. Frank (1978) developed the most realistic value for commercially used heat exchangers and is stated in equation A.28.

$$\Delta P_t = N_p \left[8j_{f,t} \left(\frac{L}{d_i} \right) \left(\frac{\mu_{t,m}}{\mu_{t,w}} \right)^{-m} + 2.5 \right] \frac{\rho_{t,m} u_t^2}{2} \quad (\text{A.28})$$

The shell side pressure drop is given by equation A.29.

$$\Delta P_s = 8j_{f,s} \left(\frac{d_s}{d_e} \right) \left(\frac{L}{l_b} \right) \left(\frac{\rho_{s,m} u_s^2}{2} \right) \left(\frac{\mu_{s,m}}{\mu_{s,w}} \right)^{-0.14} \quad (\text{A.29})$$

Where the mean medium viscosity values are again considered to be proportionate to the wall viscosity values, implying that the viscosity terms drops out of the equations.

A.4. Plate heat exchanger design steps continued

Step 8 & 9: Geometric design specifications

The required number of plates needs to be calculated for the required duty, to do so, the area per plate first needs to be calculated via Eq. A.30.

$$A_p = \phi L_p B_p \quad (\text{A.30})$$

Where ϕ is the coefficient for corrugated plates of 1.22 with an angle of 45 degrees, which are standard values for technical surfaces. The number of plates is the total heat transfer area divided by the effective area of a single plate stated in equation A.31

$$N_{plates} = \frac{\frac{A_0}{A_p}}{2} - 2 \quad (\text{A.31})$$

Where the two end plates are subtracted from the effective number of plates.

Step 10: Heat transfer coefficients per stream

To determine the heat transfer coefficients of the sensible plate heat exchangers, the Prandtl, Reynolds and Nusselt numbers are calculated with the physical properties of the steam, hydrogen and oxygen. The Reynolds and Prandtl number are already defined in the previous chapter in equations A.23 and A.24. The equation for forced-convective heat transfer in conduits can be used for PHE's, where turbulent flow is safe to assume. The plate Nusselt number is calculated via equation A.32, which is a typical value for turbulent flow.

$$Nu_p = 0.26 Re^{0.65} Pr^{0.4} \left(\frac{\mu}{\mu_w} \right) \quad (\text{A.32})$$

Where the wall viscosity is assumed to be equivalent to the bulk viscosity. Now, with the Nusselt number calculated, the plate film coefficient α can be calculated via equation A.33.

$$\alpha_p = Nu \left(\frac{\lambda_f}{d_e} \right) \quad (\text{A.33})$$

Step 11: Overall heat transfer coefficient & fouling coefficients

The overall fouling coefficients are taken from literature [83], the overall heat transfer coefficient can then be calculated via equation A.34 in $W/m^2 \cdot C$.

$$U_0 = \left[\frac{1}{\alpha_h} + \frac{1}{\alpha_{hd}} + \frac{P_t}{\lambda_w} + \frac{1}{\alpha_c} + \frac{1}{\alpha_{cd}} \right]^{-1} \quad (\text{A.34})$$

After which the assumed overall coefficient is validated with the calculated overall coefficient with the same statement presented in the previous chapter in equation A.35

$$0 < \frac{U_0 - U_{0,ass}}{U_{0,ass}} < 10\% \quad (\text{A.35})$$

Step 12: Pressure drop

There are several methods to determine the pressure drop in plate heat exchangers, in this report, the single phase pressure drops are calculated via the VDI method. The final pressure drop in a conduit is the statement presented in equation A.36.

$$\Delta P = \frac{\xi}{2} \rho u^2 \frac{L_p}{d_e} \quad (\text{A.36})$$

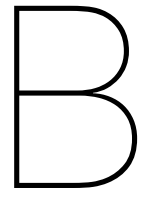
The factor ξ is calculated via equation A.37

$$\xi = \left[\frac{\cos(\phi)}{\sqrt{0.18 \tan(\phi) + 0.36 \sin(\phi) + \frac{\xi_0}{\cos(\phi)}}} + \frac{1 - \cos(\phi)}{\sqrt{3.8 \xi_1}} \right]^{-2} \quad (\text{A.37})$$

Where the factors ξ_0 and ξ_1 are dependent on the Reynolds numbers of the corresponding streams and ϕ . The two options for the calculation of ξ_0 are depicted in Eq. A.38, the two options for ξ_1 are stated in Eq. A.39.

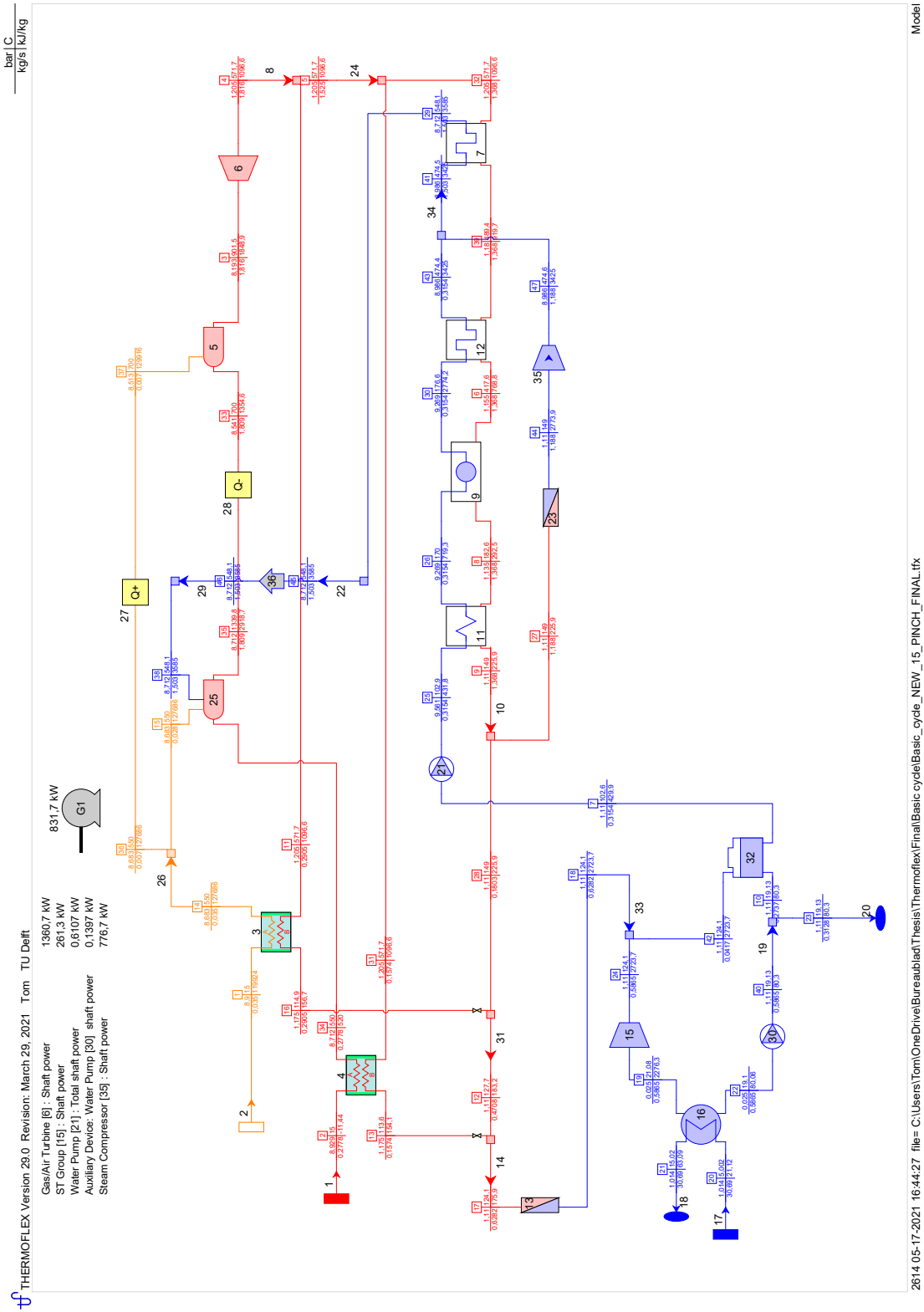
$$\xi_0 = \frac{64}{Re_p} \quad \text{For } Re_p < 2000 \quad \text{and} \quad \xi_0 = \frac{1}{(1.8 \ln Re_p - 1.5)^2} \quad \text{For } Re_p \geq 2000 \quad (\text{A.38})$$

$$\xi_1 = \frac{597}{Re_p} + 3.85 \quad \text{For } Re_p < 2000 \quad \text{and} \quad \xi_1 = \frac{39}{Re_p^{0.289}} \quad \text{For } Re_p \geq 2000 \quad (\text{A.39})$$



Thermoflex simulation models

B.1. Basic cycle Thermoflex model



B.2. Improved cycle Thermoflex model

